Molecular Beam Experiments
and Scattering Studies
with State-selected Metastable CO

Molecular Beam Experiments and Scattering Studies with State-selected
Metastable CO / Rienk Jongma.
Thesis Katholieke Universiteit Nijmegen. - Illustrated.
With references. - With summary in Dutch.
ISBN 90-9010384-8
NUGI 812
Subject headings: gas-surface interaction / electronic excitation
and ionization of molecules / laser-spectroscopic techniques.
Cover: J.J.A. Slippens and R.T. Jongma

Molecular Beam Experiments and Scattering Studies with State-Selected Metastable CO

een wetenschappelijke proeve op het gebied van
de Natuurwetenschappen

PROEFSCHRIFT

ter verkrijging van de graad van doctor
aan de Katholieke Universiteit Nijmegen,
volgens besluit van het College van Decanen
in het openbaar te verdedigen
op maandag 26 mei 1997,
des namiddags om 1.30 uur precies

door

Rienk Taco Jongma

geboren op 8 juni 1970
te Deventer

Promotores : Prof. Dr. G.J.M. Meijer
Prof. Dr. H. Zacharias

Co-Promotor : Dr. Th.H.M. Rasing

Manuscriptcommissie : Prof. Dr. J. Reuss

Prof. Dr. A.W. Kleyn
AMOLF, Amsterdam

Prof. Dr. H.-J. Freund
Fritz-Haber-Institut, Berlijn

Dit werk maakt deel uit van het onderzoeksprogramma van het 'Research Institute for Materials (RIM)'.

‘Ik geloof dat fysici in zeker opzicht religieuze mensen zijn. Want zij geloven dat er wetten zijn in de natuur, die men door hard werken kan vinden. Nou, er is geen mens die bewijzen kan dat de natuur aan wetten voldoet. Dat is een geloof.’

Abraham Pais, Natuurkundige

Voorwoord

Het boekje dat nu voor u ligt is het resultaat van vier jaar onderzoek en is uiteraard niet uitsluitend het werk van mij alleen geweest. Daarom wil ik op deze plaats al diegenen bedanken die mij de afgelopen vier jaar in meer of mindere mate hebben geholpen.

Tijdens een promotie-onderzoek is een goede begeleiding van essentieel belang. Ik had mij in Gerard nauwelijks een betere begeleider kunnen wensen. Mede door zijn creativiteit en zijn altijd aanwezige enthousiasme ligt dit boekwerk nu onder uw neus. Naast de wetenschappelijke bijdrage, zijn ook de goede samenwerking en sfeer van grote invloed geweest, met de Margarita-party's als jaarlijkse hoogtepunt ... en nu maar afwachten of ze in Californië net zo lekker smaken (en minder hoofdpijn tot gevolg hebben). Ook de bijdrage van de, immer drukke, RIM-baas Theo Rasing mag niet onvermeld blijven.

Furthermore, I wish to thank Helmut Zacharias for a very fruitful cooperation and for the valuable suggestions and new ideas appearing in the discussions (during visits to Nijmegen or via e-mail). I would like to thank Carsten Menzel for his trips to Nijmegen to prepare new LiF samples and for his helpful suggestions.

Alle leden van de manuscriptcommissie, Prof. J. Reuss, Prof. A.W. Kleyn en Prof. H.-J. Freund, ben ik erkentelijk voor het grondig lezen van het manuscript en de daaruit voortkomende verbeteringen.

De opbouw van een nieuwe opstelling is niet mogelijk zonder een goede technische ondersteuning. Daarom wil ik de immer creatieve Kapitein-Cor bedanken voor het uitzetten van de goede koers voor mijn CO-moleculen. Ik wil ook Chris, Frans, Jan Hermsen, Eugene, John en Jan Gerritsen hartelijk danken voor hun onmisbare hulp.

De ex-AIO's Bart Nelissen en Harald Wierenga waren in de aanloopfase verantwoordelijk voor de hulp bij het produceren van de lage drukgebieden.

De uitstekende samenwerking met de werkplaats heeft er voor gezorgd dat onze 'papieren' ideeën werden omgezet in mooie opstellingen, flenzen, enzovoort. Speciaal de bijdrage van Leander, Lambert en Jos wil ik daarbij noemen, als ook de talrijke (spoed) klusjes die door Wim Schut (SIM) zijn uitgevoerd en de perfecte medewerking van de glasblazerij: Jos en 2×Peter. Ferry Derksen (zelf-service) natuurlijk bedankt voor de echte hoge-nood gevallen.

Alle AIO's, post-docs en vaste medewerkers van de afdeling bedank ik voor de uitstekende samenwerking en voor de natuurkundige en materiële ondersteuning. Met name wil ik noemen: Maarten (is het nu Boog-seconde of Boog-minuut?), Nudel-Gert, snelle-Richard, Mike, Tony, Hans N., Tim, Jules, Koen en de cameraploeg gevormd door André en Robert K.; daarnaast natuurlijk de altijd vrolijke software koning William Boerstal, en Dorien voor het vervaardigen van de kleinste massa-spectrometer van de hele afdeling. Mijn altijd treinende, maar toch bijna nooit vertraagde privé post-doc Giel verdient een aparte

vermelding: vele van de hier beschreven experimenten zijn mede door deze laser- en fitkunstenaar zo goed gelukt.
Mijn twee paranimfen Iwan en Paul: bedankt voor de hulp, maar met name voor de gezelligheid in de vorm van etentjes, mailtjes en onnavolgbare 'drìnk'-avonden en 'driemusketier' weekenden in Nijmegen, Amsterdam, Asten, Antwerpen en Groningen (volgend jaar maar Californië?). Bijna aan het einde van het voorwoord wil ik mijn apetrotse ouders en alle verdere familieleden bedanken voor de voortdurende belangstelling voor mijn werk en de onmisbare ondersteuning.
En Babs: ook al mocht ik dit boekje niet aan je opdragen, je aandacht voor en, misschien nog wel belangrijker, de afleiding van mijn werk is een grote steun in de rug geweest.

Rienk Jongma april 1997

Contents

Chapter 1

General Introduction

When an atom or molecule approaches a surface, a variety of processes can occur, like diffractive scattering, direct-(in)elastic scattering or trapping. The internal energy of the incoming particles can significantly influence these processes. With the combination of molecular beam technology [1] and surface science techniques [2] all these processes can be studied under well-defined conditions to obtain detailed information about the gas-surface interaction [3]. Although the effect of kinetic, rotational, and vibrational energy on these processes has been investigated for several systems, the effect of the electronic degree of freedom has not been explored thus far. The experiments reported in this thesis focus on the production of a pure beam of electronically excited carbon monoxide molecules and on the application of such a molecular beam in surface scattering experiments.

1.1 Molecular beams

A supersonic molecular beam is obtained when a high pressure gas (mixture) is expanded through a small orifice into a vacuum chamber. Under normal operating conditions, molecular beams are collision-free and can be employed for storage and transport of fragile species like radicals, clusters, and excited atoms or molecules. With the introduction of pulsed molecular beams, the peak intensity in the beam of both 'normal' and fragile species could be increased by orders of magnitude. Combination with pulsed lasers and time-resolved detection schemes thus opened the possibility to study many systems that are otherwise impossible to access. Details about the possibilities and difficulties of molecular beam techniques are extensively described in ref. [1].

The molecular beam machine built in our laboratory is designed to produce a pure beam of CO molecules in a single rotational level of the metastable (i.e. long lived) $a^3\Pi$ state. Each of these molecules contains 6 eV of electronic energy. In the experiments, CO is seeded in a rare gas and is expanded from a valve that delivers short gas pulses. The average velocity of the CO molecules in the beam can be varied by changing the mass of the carrier gas. To obtain a clean vacuum system, the entire vacuum system is pumped by oil-free turbo molecular pumps. The relatively low capacity of these pumps makes very short gas pulses indispensable when a intense gas pulse must be combined with a small gas-load. The molecular beam machine is connected to an Ultra High Vacuum (UHV) chamber in which surface scattering experiments are performed. The gas-load to the UHV chamber is reduced by allowing exclusively the metastable CO molecules to enter the UHV system.

1.2 State-selection

The first step in the production of a beam of state-selected metastable CO is laser excitation of the ground state molecules to the metastable $a^3\Pi$ state. The availability of a pulsed laser system with a high spectral brightness allows production of an intense beam of metastable CO molecules in a single Λ-doublet component. The radiative lifetime of the laser-prepared molecules is on the order of 3 ms [4]. Because the average velocity of molecules in the beam is typically around 10^3 m/s, the metastable CO molecules can travel a few meters before they decay to the electronic ground state.

Discrimination between the laser-prepared metastable CO molecules and other gas particles present in the beam is achieved by an electrostatic hexapole state-selector. Inhomogeneous electric fields can generally be used to deflect molecules with a sufficiently large dipole moment and a significant Stark effect, and many different deflection schemes have been experimented with [5]. Electrostatic multipole configurations can not only deflect but also focus polar molecules. In this work we employ a hexapole [6] to state-select the electronically excited CO molecules. In the ideal situation a hexapole works as a lens for polar molecules, with a state-specific focal length. Molecules starting from a single point can thus be focused again in a single point. Hexapoles can be applied to enhance the number density of molecules in a specific quantum state by orders of magnitude. Since the deflection force, and thereby the selection, vanishes on the axis of the hexapole, a beamstop must be inserted to get rid of the undesired species.

In addition to focusing, the hexapole can be applied to prepare molecules for orientation in an electric field. The difference in magnitude and direction of the focusing force for the different M-components of a certain rotational level will lead to selection of specific M-components. When electric fields are properly applied, an oriented molecular beam is produced. This technique is employed to study orientational effects (head versus tail collisions) in gas-surface interactions [7] and in crossed molecular beam experiments [8].

In our experiments the hexapole is utilized to focus the electronically excited CO molecules through a small aperture, while a beamstop, mounted in the center of the molecular beam, prohibits transmission of the (unfocused) ground state CO molecules and carrier gas atoms. In this setup it is possible to generate a pure beam of electronically excited CO molecules in a single quantum-state and with well-defined velocity, ideally suited for scattering experiments.

1.3 Surface scattering

A variety of processes can occur when a molecule collides with a surface, leading to energy and momentum transfer between the molecules and the surface. In general, direct-(in)elastic scattering and trapping is observed. When light particles are impinging on the surface, diffractive scattering can be observed in addition. For reactive systems, chemisorption followed by other processes like dissociative adsorption, diffusion, formation of ordered surfaces etc. may occur. The gas-surface interaction can be studied in detail when molecular beam techniques are combined with surface science technology.

From direct-elastic scattering processes, information about the surface morphology can be extracted. When the kinetic energy of the incoming beam is low, the atomic or molecular particles form a very soft probe of the surface because they are physically unable to damage, or penetrate into, the surface. Under these conditions only the outermost layers of the sample are probed; in this respect the scattering technique compares favourably to a surface spectroscopic technique like Low Energy Electron Diffraction (LEED) [2]. Especially when an atomic beam is employed, i.e. when the degrees of freedom of the scattered particle are largely reduced, information about the static characteristics of the surface and the presence of possible contaminants can be obtained. The advantage of surface spectroscopic techniques like LEED and Auger Electron Spectroscopy (AES), however, is that they are more readily applicable since the generation and manipulation of charged particles allows preparation of a 'monochromatic' (i.e. mono-energetic), well-collimated beam in a straightforward manner. Additionally, they directly provide information about structure and chemical composition of the surface.

Apart from applying surface scattering as a tool for probing purely the surface structure, it can be used to study more relevant gas-surface processes as well. The understanding of complex systems, e.g. reactive systems, on a state-to-state basis is not yet possible with the currently available techniques. The study of less complicated systems (in which processes like trapping-desorption and direct-(in)elastic scattering occur) is a prerequisite for further understanding and for knowledge about energy transfer of the translational, rotational, vibrational, as well as the electronic degrees of freedom of the scattering partner and the surface.

In scattering studies both the angular and the velocity distribution of the scattered particles contain information about energy transfer. Additionally, the development of laser-based detection techniques allows sensitive and state-specific probing of the species of interest. When these techniques are applied, a state-to-state analysis of the scattered particles can be performed.

If heavy species are scattered, there is normally a small probability for direct-elastic scattering. For non-reactive systems direct-inelastic scattering or trapping-desorption will occur. For the extensively studied NO/Ag(111) systems it is shown that with increased kinetic energy of the incoming beam the direct-inelastic scattering channel is favoured relative to the trapping-desorption channel [9]. Ultimately, the orientation of the incoming molecule can influence the relative probability of both processes. This effect is observed for the NO/Ag(111) system [10] and is much more dramatic for the strongly attractive NO/Pt(111) system [11].

Studies with excited or polarized molecular beams are still rare in the field of gas-surface interactions although it is obvious that the internal energy of the incoming molecule can have large effects on the processes that occur. The H_2/Cu(111) system, for example, is believed to have an activation barrier for dissociative adsorption. Additional to kinetic energy, vibrational energy can efficiently be used to overcome this barrier [12, 13]; several studies have been performed to test this mechanism (see references in ref. [14]).

Apart from the influence of the translational, rotational, and vibrational degree of freedom on molecular surface scattering, the influence of the electronic degree of freedom is of importance. The energy involved in gas-surface interactions is generally too low to expect electronical excitation of molecules to occur. Surface scattering experiments with an incoming beam of electronically excited molecules, however, are free of this energetic restriction but stil form an unexplored field of investigation. The properties of electronically excited molecules, like bond-length, vibrational energy, and electronic structure, can change drastically as compared to ground state molecules, thereby completely changing the scattering behaviour. A big difficulty with experiments of this type is formed by the preparation of the electronically excited species. The molecule has to be excited close enough to the surface so that it can reach the surface within the lifetime of the excited state. In practice, this implies that exclusively molecules with a metastable electronic state, i.e. with a long lived electronically excited state, are suited for these experiments.

The large amount of energy stored in electronically excited species gives rise to an additional category of processes. If the workfunction of the surface is low enough, the electronic energy of the incoming particle can be used for emission of electrons in so called Auger-processes. In particular, the large amount of energy stored in metastable atoms gives rise to a variety of emission schemes [15]. For metastable atoms these processes have been extensively studied and are a tool for surface characterization [16, 17], even applicable to semiconductor surfaces [18]. Similar studies with metastable molecules have not been performed yet. The lack of information about the scattering behaviour of electronically excited molecules is an important motivation for the molecular beam surface scattering experiments reported here.

1.4 Outline

Most of the experiments reported in this thesis are performed with the molecular beam machine described above. In chapter 2, the details of the molecular beam machine are given. In the reported experiments time- and spatially-resolved techniques for detection of metastable CO molecules are employed to characterize the molecular beam in terms of parallel and perpendicular velocity distributions and to determine the rotational temperature achieved due to cooling in the expansion. A two-dimensional detection technique for metastable CO molecules is applied to study the details of the focusing performance of an electrostatic hexapole and to demonstrate the mass-focusing effect. In addition, the possibility to produce a pure beam of metastable CO utilizing the hexapole-beamstop-diaphragm combination has been explored.

Chapter 3 describes the techniques that are used throughout this thesis for detection of the metastable CO molecules. One scheme is based on detection of Auger electrons, produced by the metastable CO molecules upon impact on the surface of a Micro-Channel Plate (MCP) detector; calibration of the efficiency of the MCP detector is accomplished by simultaneous detection of metastable CO molecules and laser-produced ions. It is shown that, under the appropriate experimental conditions, monitoring the spin-forbidden a→X fluorescence is a straightforward way to detect metastable CO. A large part of this chapter deals with the determination of the fluorescence properties of the metastable CO molecules, including the branching ratios and the radiative lifetime. Different ionization schemes to allow efficient and state-selective detection of the metastable CO molecules are also discussed.

As a spin-off, in chapter 4 a novel experimental scheme is described, capable of confining metastable CO molecules in quasi-stable 'orbits'. This scheme is substantiated by trajectory calculations based on measurements of the Stark effect in electric fields up to 150 kV/cm.

The last two chapters of this thesis deal with the scattering of metastable CO molecules from a LiF(100) surface. In chapter 5 the first scattering experiments with electronically excited molecules are reported. Metastable CO molecules are state-selected, and a pure beam of metastable CO molecules is scattered from the LiF(100) surface. The velocity distribution, angular distribution, and internal-state distribution of the scattered molecules are measured and unambiguously indicate a direct-inelastic scattering process.

In the last chapter, scattering of vibrationally and electronically excited CO molecules in the $a^3\Pi(v{=}1)$ state from a LiF(100) surface is described. Because in the incoming beam the vibrational ground state of the $a^3\Pi$ state is not populated, the vibrational deactivation probability can be determined very accurately. In addition, it allowed a comparison between the electronic and vibrational relaxation rate.

1.5 Future

The scattering experiments reported here are performed exclusively with a LiF(100) surface. The characteristics of the CO($a^3\Pi$)/LiF system have not been fully explored yet and many complementary studies can still be pursued. Detailed information about the influence of the angle of incidence and the surface temperature on the velocity distribution, the internal state distribution, and the angular distribution will yield more insight into the nature of the scattering process and the importance of phonons for the scattering process. Although some studies have been performed already, state-distributions of the deexcited CO molecules could not be obtained because ro-vibrational levels in the electronic ground state of CO cannot be probed very efficiently. Since it concerns the major fraction of the incoming molecules ($\geq$95%), however, this still is an important task and will provide knowledge about the deexcitation mechanism.

Also experiments with other surfaces should be performed. It would be interesting to compare the scattering behaviour of the CO($a^3\Pi$)/LiF system with the results of CO($a^3\Pi$) scattered from surfaces like diamond and graphite. At these surfaces part of the CO molecules will retain their electronic energy for similar reasons as for the LiF surface. The absence of the dipole-dipole interaction for these surfaces can confirm or invalidate the given explanation for the broad angular distribution observed in the CO($a^3\Pi$)/LiF scattering experiments.

Other interesting systems can also be found in scattering metastable CO from oxidized metal surfaces. It is known that the lifetime of CO($a^3\Pi$) adsorbed on Al_2O_3(111) is relatively long due to the absence of fast relaxation channels via Auger deexcitation or via the formation of electron-hole pairs [19]. Scattering of metastable CO molecules from oxidized metal surfaces can thus improve the understanding of desorption processes involving electronic transitions at these surfaces.

If metastable atoms are impinging on a surface, a precisely known amount of energy is consumed for emission of Auger electrons. The kinetic energy distribution of the emitted Auger electrons thus directly reflects the density of states of the surface. This Metastable Deexcitation Spectroscopy (MDS/MIES) technique is usually applied to metal surfaces. When metastable molecules are utilized the density of states is probed repeatedly: once for each vibrational level to which the molecules are deexcited. Each vibrational level that is populated in the deexcitation process shows a similar kinetic energy distribution of the electrons, but shifted to lower energies over the total amount of vibrational energy. For metastable molecules, information about the density of states is thus hidden in a complicated distribution. The Auger process itself, however, is very interesting. For metastable CO, probing the population of the different vibrational levels of the deexcited molecules yields the 'Franck-Condon' factors for the deexcitation process. A promising approach would be to determine the kinetic energy of the released electrons. If the density of states is known for the specific metal surface, for example from metastable atom scattering, the contribution of the different vibrational levels can be extracted to determine the 'Franck-Condon' factors for this process. Due to the relatively low (6.0 eV) electronic energy of metastable CO, efficient Auger deexcitation occurs particularly at metal surfaces.

An extra degree of sophistication can be added to these scattering experiments when the metastable CO molecules are oriented before colliding with the surface, a possibility that has not been exploited in the studies reported here.

To summarize, surface scattering experiments with electronically excited molecules will allow a large number of challenging experiments to be performed in the near future.

References

[1] *Atomic and Molecular Beam Methods*, Vol. I and II, ed. G. Scoles, (Oxford University Press, New York, 1988/1992).

[2] D.P. Woodruff and T.A. Delchar, *Modern Techniques of Surface Science*, (Cambridge University Press, Cambridge, England, 1986).

[3] J.A. Barker and D.J. Auerbach, Surf. Sci. Reports **4**, 1 (1984).

[4] T.C. James, J. Chem. Phys. **55**, 4118 (1971).

[5] J. Reuss, (1988), See [1], 276-292.

[6] K.H. Kramer and R.B. Bernstein, J. Chem. Phys. **42**, 767 (1965).

[7] E.W. Kuipers, M.G. Tenner, A.W. Kleyn, and S. Stolte, Nature **334**, 420 (1988).

[8] J.J. van Leuken, J. Bulthuis, S. Stolte, and J.G. Snijders, Chem. Phys. Lett. **260**, 595 (1996).

[9] E.W. Kuipers, M.G. Tenner, M.E.M. Spruit, and A.W. Kleyn, Surf. Sci. **205**, 241 (1988).

[10] E.W. Kuipers, M.G. Tenner, A.W. Kleyn, and S. Stolte, Chem. Phys. **138**, 241 (1989).

[11] E.W. Kuipers, M.G. Tenner, A.W. Kleyn, and S. Stolte, Phys. Rev. Lett. **62**, 2152 (1989).

[12] J. Harris, Surf. Sci. **221**, 335 (1989).

[13] M. Hand and S. Holloway, Surf. Sci. **211/212**, 940 (1989).

[14] C.T. Rettner, D.J. Auerbach, J.C. Tully, and A.W. Kleyn, J. Phys. Chem. **100**, 13021 (1996).

[15] H.D. Hagstrum, Phys. Rev. **96**, 336 (1954).

[16] W. Sesselmann, H. Conrad, G. Ertl, J. Küppers, B. Woratschek, and H. Haberland, Phys. Rev. Lett. **50**, 446 (1983).

[17] W. Maus-Friedrichs, S. Dieckhoff, and V. Kempter, Surf. Sci. **249**, 149 (1991).

[18] S. Masuda and Y. Harada, Surf. Sci. **283**, 78 (1993).

[19] R.M. Jaeger, K. Homann, H. Kuhlenbeck, and H.-J. Freund, Chem. Phys. Lett. **203**, 41 (1993).

Chapter 2

Two-Dimensional Imaging of Metastable CO Molecules: Characterization of the Molecular Beam [1]

Abstract

Direct time- and spatially-resolved detection of metastable CO molecules, prepared in selected quantum states via pulsed laser excitation, is experimentally demonstrated in a molecular beam machine. The molecular beam is characterized in terms of parallel and perpendicular velocity distributions and rotational temperatures. A direct two-dimensional (2D) demonstration of the mass-focusing effect in binary gas mixtures is presented.

Two-dimensional imaging of the spatial distribution of the metastable CO ($a^3\Pi$) molecules in the beam after passage through a hexapole field is used to study hexapole focusing performance. Structured 2D-images demonstrate the dependence of the focusing characteristics on the magnitude of the Λ-doubling and on the angular dependence of the focusing force in a hexapole consisting of cylindrical rods.

It is shown that the combination of hexapole, beamstop and diaphragm can provide a pure beam of metastable CO molecules in a single quantum state.

---

[1] Adapted from: R.T. Jongma, Th. Rasing, and G. Meijer, J. Chem. Phys. **102** 1925 (1995).

2.1 Introduction

Over the last few years a variety of two-dimensional (2D) imaging techniques has been experimentally demonstrated and applied in different fields. Spatially resolved detection of planar laser induced fluorescence has turned out to be a powerful tool in combustion diagnostics and has been used for *in situ* 2D visualization of combustion species not only in stationary flames but also in combustion chambers of running engines [1, 2]. Fluorescence imaging as well as ion-imaging techniques have added an extra dimension to photo-dissociation studies and to studies of (in)elastic and reactive scattering processes [3, 4]. In the field of quantum electronics, spatially resolved detection of metastable atoms is used to visualize minute photo-deflection and atomic interference effects.

In this chapter we report on 2D-imaging of metastable molecules. First, direct time-resolved (and spatially-integrated) detection of laser prepared metastable CO molecules in a molecular beam is described. This detection technique is used to characterize the molecular beam in terms of parallel velocity distribution and rotational temperature. In contrast to similar time-resolved measurements by Wodtke and co-workers [5], we use a Micro-Channel Plate (MCP) to directly detect the metastable molecules, allowing for a straightforward extension of this technique to two dimensions. Direct 2D-imaging of metastable CO molecules in the molecular beam is then used to measure the perpendicular velocity distribution of CO in the beam, and thereby completes the characterization of the molecular beam. A clear 2D visualization of the mass-focusing effect in binary CO/rare gas mixtures is given.

Direct 2D-imaging of metastable CO molecules is also used to study the focusing performance of an electrostatic hexapole. Hexapoles are used throughout for state-selection of polar symmetric top molecules using the first order Stark effect [6–8]. With the combination of guiding fields and orientation fields the selected molecules can be oriented as well. Application of hexapoles in reaction dynamics and in molecular beam scattering experiments [9], in surface scattering experiments [10] as well as in photodissociation studies [11, 12] has yielded a wealth of information on the steric effects in these processes. The operation characteristics of a hexapole are commonly determined via measurement of the focusing curve, i.e. via measurement of the (state-selective) molecular beam intensity integrated over a certain area as a function of the voltage applied to the hexapole-rods [13, 14]. We here present measurements of the full 2D distributions of the metastable CO molecules in the beam after passage through a hexapole field as a function of the voltage applied to the hexapole rods. Structured 2D-images demonstrate the dependence of the focusing characteristics on the magnitude of the Λ-doubling and show the effect of the deviations of the hexapole field in a hexapole consisting of cylindrical rods from the ideal hexapole field.

After having obtained a complete characterization of the molecular beam, the molecular beam machine is connected to an Ultra High Vacuum (UHV) scattering chamber and the possibility to produce a pure beam of metastable CO molecules is demonstrated.

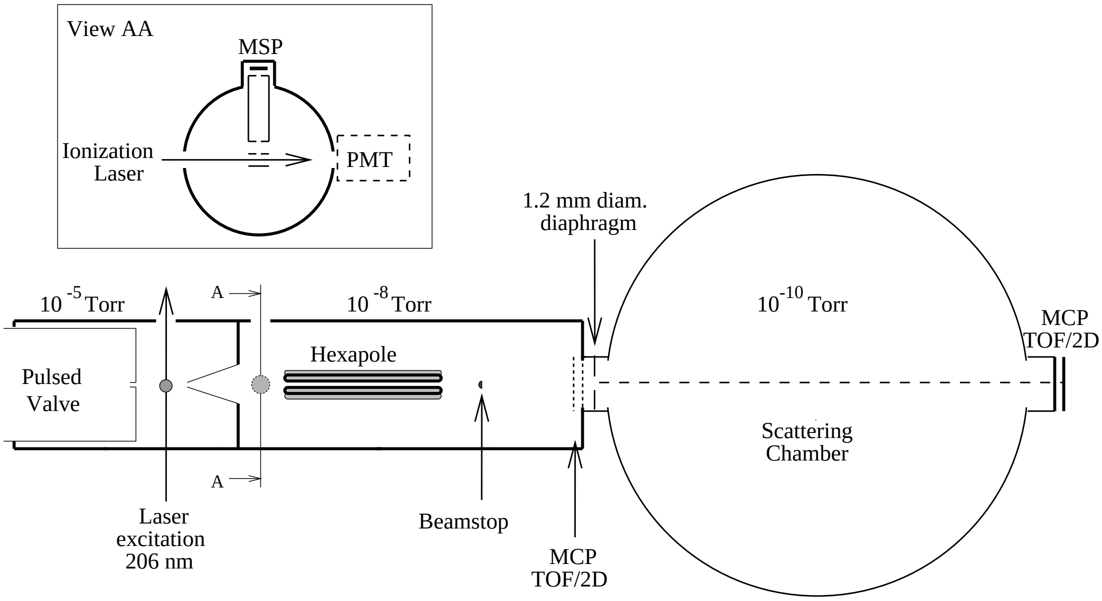

Figure 2.1: *Schematic overview of the vacuum machine, composed of three differentially pumped chambers. The pulsed valve releases short gas pulses of CO diluted in a rare gas. Metastable* $a^3\Pi(v'=0)$ *CO molecules are prepared via pulsed laser excitation around 206 nm of jet-cooled ground state CO molecules and enter the differentially pumped hexapole chamber through the skimmer. Directly after the skimmer a small Wiley-McLaren type time-of-flight mass spectrometer is mounted to perform REMPI spectroscopy in the molecular beam. A cross-section at this position is displayed at the top of the figure, showing the electrode assembly and the MSP detector used for ion detection. If the mass spectrometer is not in use, excitation to the metastable state can be monitored with the optional PMT (dashed) looking at the spin-forbidden fluorescence signal of the metastable CO molecules. Downstream from the mass spectrometer the metastable CO molecules pass through an electrostatic hexapole state-selector and impinge on a MCP detector (dashed) where they are time- and spatially-resolved detected. Part of the beam can optionally be blocked by a beamstop. After removal of the MCP detector at the end of the hexapole chamber, the molecular beam machine is connected to the UHV chamber via a small diaphragm. A pure beam of metastable CO molecules can thus be produced as is verified with the same MCP based detection techniques, but now applied at the end of the UHV chamber.*

2.2 Experimental

A schematic overview of the vacuum system is shown in Fig. 2.1. The machine is composed of three differentially pumped stainless steel vacuum chambers. The first two chambers, the source chamber and the hexapole chamber, form the molecular beam machine, configured to provide a pure beam of metastable CO molecules. The pure beam of metastable CO molecules can be used in the UHV chamber for surface scattering or surface spectroscopic experiments.

In the source chamber a pulsed valve (R.M. Jordan Co.) operating on the magnetic repulsion principle is mounted. The valve has a 0.35 mm diameter orifice and delivers gas pulses of typically 30 μs duration at a repetition frequency of 10 Hz. A mixture of either 5% or 10% CO in a rare gas at a total backing gas pressure of 2 atm. is used for the supersonic expansion. About 2 cm downstream from the nozzle the jet-cooled ground state CO molecules are excited to the metastable $a^3\Pi(v'{=}0)$ state by pulsed 206 nm laser radiation.

The laser system used for quantum-state selective preparation of metastable CO molecules consists of a Nd:YAG laser pumped pulsed dye laser system (Spectra Physics, GCR 150/PDL-3 combination) operating on a DCM/Sulforhodamine 640 dye mixture that is optimized for producing 618 nm radiation. The output of the dye laser (95 mJ/pulse, 0.07 cm^{-1} bandwidth) is frequency tripled in a combination of a KDP and a BBO crystal, thus producing linearly polarized tunable 206 nm radiation with an energy of 1.5 mJ/pulse in a 0.2 cm^{-1} bandwidth. The laser light is focused by a 21 cm focal length lens into the molecular beam machine, intersecting the molecular beam perpendicularly. The light transmitted through the machine is focused back onto the same spot in the molecular beam by a plano-concave mirror with a radius of curvature of –25 cm, thus approximately doubling the number of metastable CO molecules produced.

After passing the excitation region, the molecular beam is collimated by a 0.8 mm diameter skimmer located 4 cm away from the nozzle, and enters the differentially pumped hexapole chamber. In the hexapole chamber a small Wiley-McLaren type Time-Of-Flight (TOF) mass spectrometer [15], as schematically indicated in the cross-section in Fig. 2.1 (view AA), is mounted 7.5 cm downstream from the excitation region. This mass spectrometer can be used to test several ionization schemes for CO, or to perform Resonance Enhanced Multi-Photon Ionization (REMPI) spectroscopy of CO. The (gridless) extraction electrodes have a diameter of 17.5 mm and are equally spaced at a distance of 6 mm. The grounded field free flight tube has a length of 10 cm. At the end of the flight tube the ions are detected on a Micro-Sphere Plate (MSP) detector (El-Mul). Only the upper electrode of the flight tube is equipped with a grid, to shield for electric stray fields caused by the voltages applied to the MSP detector. Ionization can be performed from the metastable state in CO between the lower two extraction plates, for example via (1+1)-REMPI with a second laser that is resonant with ro-vibrational transitions in the $b^3\Sigma^+ \leftarrow a^3\Pi$ band of CO. An example of a mass spectrum recorded in this set-up is given in Fig. 2.2. The only feature that is present in the mass spectrum at 28 Dalton is caused by CO$^+$ ions. The mass resolution, determined by the ratio $m/\Delta m$ in which Δm is the full width at half maximum, is calculated from this spectrum to be 33. Further results using this mass spectrometer will not be discussed in this thesis. If the mass spectrometer is not in use, a photomultiplier (PMT, indicated with dashed line in the cross-section in Fig. 2.1) can be used to monitor the production of metastable CO molecules by recording the spin-forbidden $a^3\Pi \rightarrow X^1\Sigma^+$ fluorescence signal.

After passage through the mass spectrometer, the CO molecules encounter a 15 cm long electrostatic hexapole state-selector, the entrance of which is 13 cm downstream from the laser excitation region. The 4 mm diameter cylindrical hexapole rods, located at the outside of an 8 mm diameter circle, provide an electric field that approximates the ideal

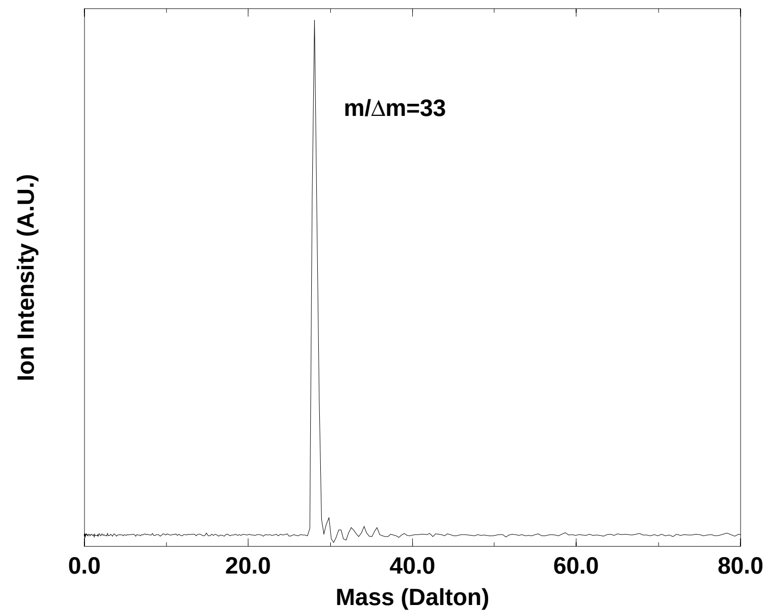

Figure 2.2: *Mass spectrum recorded with the small Wiley-McLaren type TOF mass spectrometer. The only feature observed is caused by CO^+. The mass resolution ($m/\Delta m$) deduced from this spectrum is around 33.*

hexapole field [14, 16]. A 1.2 mm diameter beamstop can optionally be inserted 2 cm behind the end of the hexapole and can be adjusted via an UHV manipulator. At the end of this chamber the molecular beam impinges upon a 25 mm diameter MCP detector (R.M. Jordan Co.) that is used for selective detection of the metastable CO molecules. For the time-resolved (and spatially-integrated) measurements in the hexapole chamber the MCP detection stage is a double MCP with ns time resolution located 38 cm downstream from the excitation region. For the spatially resolved 2D-imaging measurements a single MCP/phosphor screen (P20) detector (LaVision GmbH), located 49 cm downstream from the excitation region, is used in combination with a CCD camera system.
After finishing the experiments in the hexapole chamber and removal of the MCP detection stage at the end of the hexapole chamber, the molecular beam machine is connected to the UHV chamber via a 1.2 mm diameter diaphragm. The molecular beam of metastable CO molecules is detected again in the UHV chamber. The MCP detectors for time- and spatially resolved detection of the metastable CO molecules inside the UHV chamber are located 98 cm and 93 cm downstream from the excitation region, respectively.

The source chamber and the hexapole chamber are pumped by a 300 l/s and a 240 l/s turbo molecular pumping system, respectively, yielding background pressures of $1.5{\cdot}10^{-5}$ Torr in the source chamber and around $2.0{\cdot}10^{-8}$ Torr in the hexapole chamber under operating conditions. The UHV chamber is pumped by the combination of a 240 l/s turbo molecular pump and a titanium sublimation pump. The base pressure of the system, after bake-out, is around $2.0{\cdot}10^{-10}$ Torr and does not increase significantly during operation.

For the time-resolved detection of the metastable CO molecules in both the hexapole chamber and the UHV chamber the double MCP detection stage is terminated with a 1 kΩ resistor to increase the detection sensitivity. The concomitant loss in time resolution (determined by the RC-time of the detection system) is unimportant on the time-scale of the actual TOF measurements. The TOF distributions are digitized and displayed on an oscilloscope with a 100 MHz sampling rate and a 10 bit vertical resolution (Lecroy 9430). From single shot TOF distributions it is deduced that the number of metastable molecules measured on the detector is typically on the order of 10^3–10^4 per pulse. To improve the measurement statistics the TOF transients are averaged over 3000 shots. The averaged TOF transients are read into a 486-PC via a GPIB interface. Laser excitation spectra are recorded by measuring the time-integrated TOF signal as a function of the excitation laser frequency.

For the spatially-resolved detection of the metastable CO molecules the combined MCP/phosphor screen detector is used. To suppress the background noise (e.g. from ion gauges) and to retain part of the time-resolution the MCP is gated using a high voltage pulser. The phosphor screen is coupled to the outside of the vacuum machine by a fiber optical taper and imaged on a CCD chip with a 12 bit resolution and 384x288 pixels. The CCD chip is cooled to –15 °C with a Peltier element to reduce the dark current. The CCD camera is interfaced to and controlled by a 486-PC. With this detection system (LaVision GmbH) the 2D spatial distribution of the CO molecules under various molecular beam conditions with and without applied hexapole fields has been visualized, both in the hexapole chamber and in the UHV chamber.

Triggering of valve, laser and detection system is regulated by a digital delay generator (DG535, Stanford Research Systems Inc).

2.3 Metastable CO production and detection

Metastable CO molecules are produced by pulsed laser excitation of ground state CO molecules on the spin-forbidden $a^3\Pi(v'=0) \leftarrow X^1\Sigma^+(v''=0)$ transition (Cameron band) around 206 nm. Single rotational levels in the metastable state can be prepared. A detailed presentation of the excitation scheme is shown in Fig. 2.3. In the $^1\Sigma^+$ electronic ground state of CO, which is best described in the Hund's case (b) approximation [17], the rotational structure is fully characterized by the quantum number $N(=J)$ corresponding to the end-over-end rotation vector $\vec{N}$. The parity of the rotational levels in the electronic ground state is given by $(-1)^N$. The rotational structure in the $a^3\Pi$ state is characterized by the quantum number J, corresponding to the total angular momentum vector $\vec{J}$. For low J-values, the $a^3\Pi$ state is best described in the Hund's case (a) approximation. In this approximation, three different rotational ladders belonging to the possible values of the quantum number Ω, in which $\vec{\Omega}$ is the projection of the total angular momentum $\vec{J}$ on the internuclear axis, are distinguished. Each J-level is split by the Λ-doubling in two components with opposite parity, as shown enlarged in the figure.

The spin-forbidden $a^3\Pi(v'=0)\leftarrow X^1\Sigma^+(v''=0)$ transition becomes weakly allowed due to spin-orbit interaction of the $A^1\Pi$ state with the $a^3\Pi$ state, i.e. due to the amount of $^1\Pi$ character in the $^3\Pi$ state. The selection rules are therefore identical to those of a $^1\Pi \leftarrow ^1\Sigma^+$

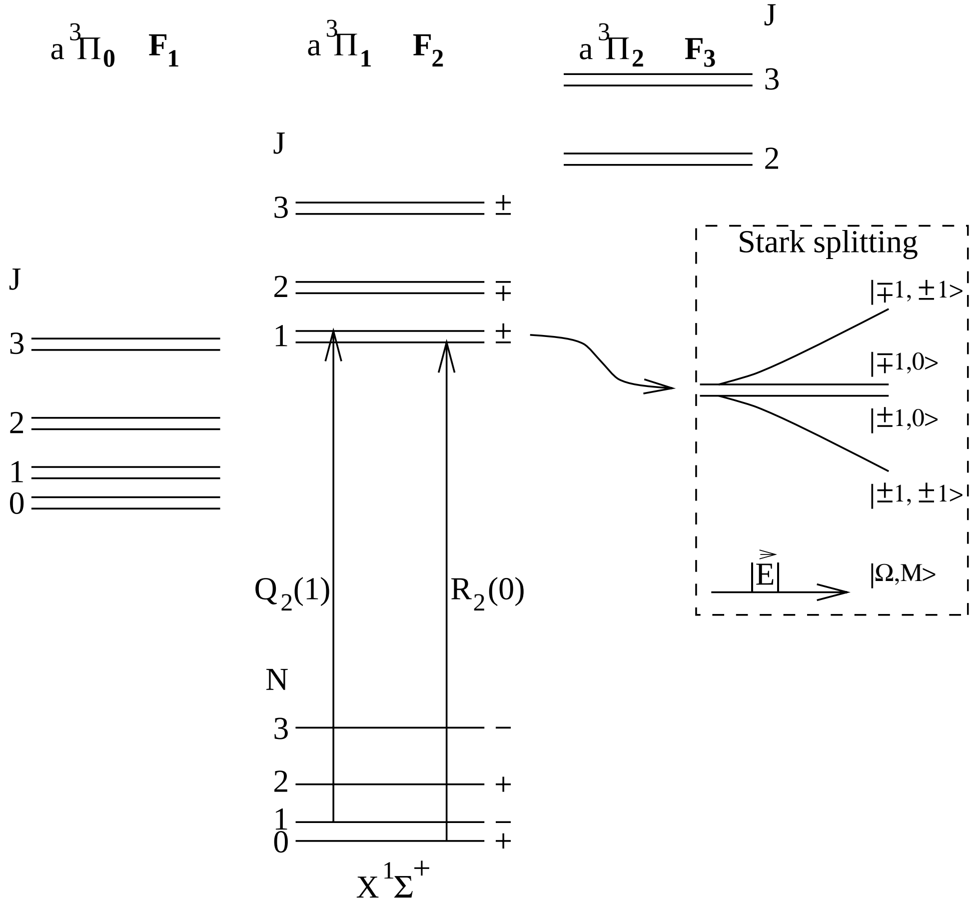

Figure 2.3: *Excitation scheme for the* $a^3\Pi \leftarrow X^1\Sigma^+$ *transition in CO. Quantum numbers and parity of the rotational levels are indicated. For low* J*-values the dominant transitions are to the* Ω*=1 component of the* $a^3\Pi$ *state, as indicated. The behavior of the* Λ*-doublet components of the* $a^3\Pi_1$*,* J*=1 level in an electric field is schematically indicated in the dashed box.*

transition. In the pure Hund's case (a) description this implies that only transitions to the Ω=1 multiplet component of the $a^3\Pi$ state are allowed. For higher J-values there is a considerable amount of mixing of the various multiplet components in the triplet state [18], and excitation is no longer restricted to the Ω=1 component. The validity of this model [19] has been experimentally verified in previous studies [5, 20, 21]. The radiative lifetime of the metastable CO molecules is several ms and is strongly J-dependent. The prominent transitions used in our experiments are indicated in Fig. 2.3 using the conventional notation $\Delta J_{F_{final}}(N'')$ [17], where F_{final} is 1, 2 and 3 for Ω is 0, 1, and 2, respectively.

In the presence of an external electric field, like the electrostatic hexapole field, the $(2J{+}1)$ fold M-degeneracy of each J-level, where M is the projection of $\vec{J}$ in the direction of the electric field, is lifted. In the $X^1\Sigma^+$ state only a second order Stark effect exists, yielding negligible (MHz) splittings in the electric fields present in the hexapole. In the metastable $a^3\Pi_1$ state there is a first order Stark effect and with a dipole moment of 1.37 D [22] Stark splittings on the order of a GHz occur in the hexapole field under our operating conditions. The behavior of the Λ-doublet components for the J=1 level in the $a^3\Pi_1$ state in an electric field is schematically indicated in the dashed box in Fig. 2.3. In zero electric field the splitting of these Λ-doublet components is 394 MHz [22]. With the hexapole state selector molecules in (Ω,J,M) levels with a positive Stark effect, i.e. levels that increase in energy with increasing electric field strength, can be focused and a (Ω,J,M) state-selected and oriented molecular beam can be produced. The M=0 levels can not be deflected by a hexapole field at all whereas states with a negative Stark effect are defocused. A more detailed description of the Stark effect for the J=1 level of the $a^3\Pi$ state, especially in the limit of high electric fields, is given in chapter 4.

In the experiments reported here the laser preparation of the metastable CO molecules takes place in zero electric field so there is no M-selection in the excitation process, and M-state selection only takes place afterward in the hexapole field. An alternative approach for the production of a beam of state-selected and oriented metastable CO molecules is to induce the $a^3\Pi(v'=0) \leftarrow X^1\Sigma^+(v''=0)$ transition in a static electric field with a laser that has a bandwidth that is narrow enough that individual $M' \leftarrow M''$ transitions can be resolved [23]. As will be shown explicitly below, however, hexapole state-selection and focusing has the advantage that it permits a complete discrimination against non-selected (ground state) CO molecules and against the rare gas carrier atoms. A truly pure beam of state-selected and oriented metastable CO molecules can thus be produced.

The electronically excited metastable CO molecules can be detected via the ejection of electrons when the metastable molecules impinge on a metal surface. Various studies have been performed on the ejection of electrons from metals by impact of atomic (metastable) ions [24, 25]. An early theoretical description of these processes has been given by Hagstrum in 1954 [26]. Auger deexcitation processes of metastable neutral atoms have also been studied and these studies have led to the development of metastable atom deexcitation spectroscopy as a surface spectroscopic technique [27].

Generally, when a metastable molecule collides with a metal surface the molecule can become deexcited via two mechanisms. The first mechanism is resonant ionization of the excited molecule followed by Auger neutralization. The second mechanism is direct Auger deexcitation of the metastable molecule. Both processes eject Auger electrons but can be distinguished by the different kinetic energy distributions of the ejected electrons. The resonant ionization process is an one-electron process that takes place when the metastable molecule is still relatively far away from the surface and is a much faster process than the two-electron Auger deexcitation process. The resonant ionization process can only occur, however, when the effective ionization potential of the metastable molecule is smaller than the workfunction of the metal, i.e. only if the energy of the metastable level is above the Fermi level of the metal. The 6 eV internal energy of the metastable CO $a^3\Pi$ molecules is sufficient to eject Auger electrons from nearly any metal. As there is still 8 eV needed to ionize the metastable molecules, however, all the electrons are produced in a direct Auger deexcitation process only. This latter process is schematically indicated in Fig. 2.4, for a metastable CO molecule at a distance S from a metal surface with a work function Φ

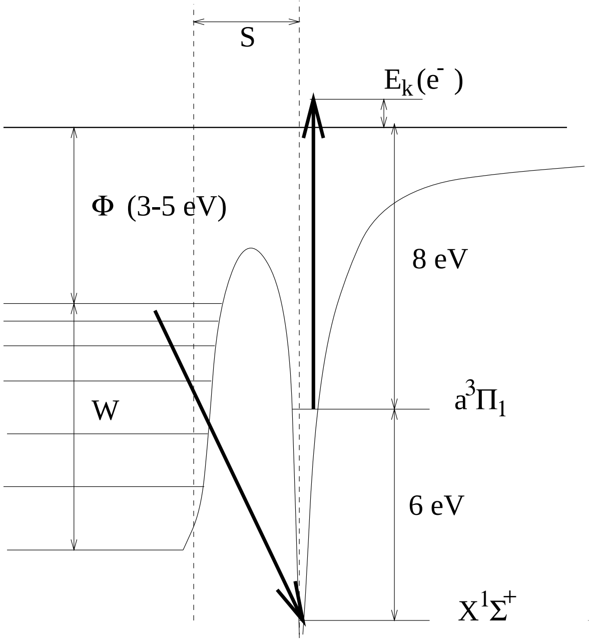

Figure 2.4: *Energy level structure of a metastable CO molecule at a distance S from a metal surface (work function Φ, Fermi energy W). Metastable CO molecules are detected via the electrons that are ejected according to the indicated Auger deexcitation process.*

and a Fermi energy W. An electron from the conduction band of the metal deexcites the metastable molecule and the energy gained in this process is used to let an electron escape from the metal/molecule system with a kinetic energy $E_k(e^-)$.

When a metastable CO molecule strikes the surface of a MCP detector the direct Auger deexcitation process takes place as well. The produced Auger electrons are multiplied by the MCP and single emitted, amplified Auger electrons can thus be detected. The workfunction of the MCP detectors we used is approximately 5 eV and metastable CO $a^3\Pi(v'=0)$ molecules can be time- and spatially-resolved detected with an efficiency of around 10^{-3}.

2.4 Results and discussion

2.4.1 Molecular beam characterization

Velocity distributions and internal-state distribution

Time-resolved measurements are performed to determine the velocity distribution of ground state CO molecules in a well-defined quantum state as well as to determine the rotational temperature of the supersonically expanded molecular beam. The parallel velocity distribution $f(v_{||})$ for a specific rotational level in the $X^1\Sigma^+$ $(v''=0)$ state is directly deduced from the measured TOF distribution of metastable CO molecules that are prepared out of this specific rotational level. In Fig. 2.5 the measured TOF distributions for 5% CO

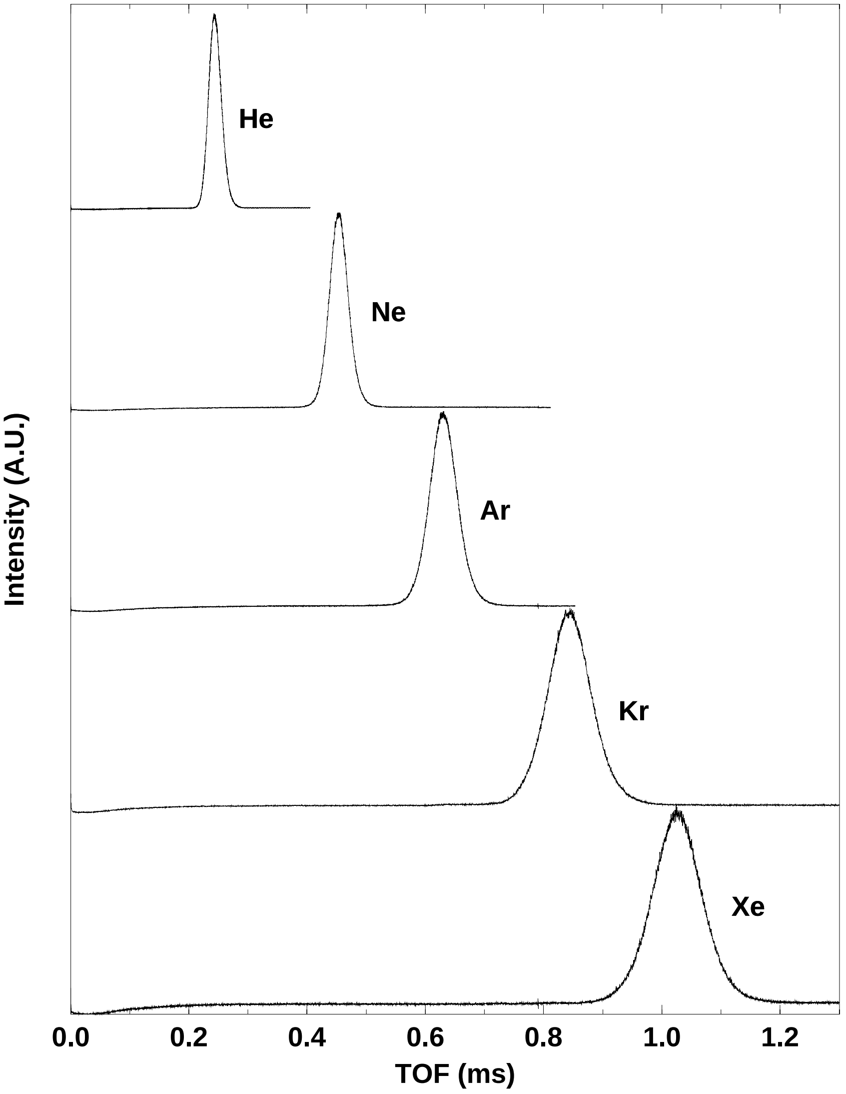

Figure 2.5: *Measured TOF distributions for 5% CO expanding in He, Ne, Ar, Kr, and Xe. The TOF distributions are measured after excitation on the $R_2(0)$ transition, thus monitoring CO molecules in the $X^1\Sigma^+$ (v''=0, N''=0) ground state. On the horizontal axis the time-of-flight for the 38 cm path from the laser excitation region to the detector is indicated.*

expanding in He, Ne, Ar, Kr, and Xe are shown. These TOF distributions are measured after excitation on the $R_2(0)$ transition, thus monitoring the TOF of CO molecules in the $X^1\Sigma^+$ (v''=0, N''=0) state. On the horizontal axis the time-of-flight for the 38 cm path from the laser excitation region to the detector is indicated. Vertically the signal intensity is shown.

The observed TOF distributions are fit to the Gaussian velocity distribution [28]

$$f(v_{||}) = \left(\frac{m}{2\pi k T_{||}}\right)^{1/2} e^{-S_{||}^2(1-\frac{v_{||}}{\overline{v}_{||}})^2} \tag{2.1}$$

in which $\overline{v}_{||}$ is the average parallel velocity, m is the mass of the carrier gas, k is Boltzmann's constant and $T_{||}$ is the parallel translational temperature, a parameter determined by the width of the velocity distribution. The parallel speed ratio $S_{||}$ is related to $T_{||}$ via

$$S_{||} = \frac{\overline{v}_{||}}{\left(\frac{2kT_{||}}{m}\right)^{1/2}} \tag{2.2}$$

The resulting parameters of the fit ($\overline{v}_{||}$, $T_{||}$ and $S_{||}$) are found in Table 2.1 for the various TOF distributions displayed in Fig. 2.5. The observed TOF distributions are accurately described by this velocity distribution function, and a more sophisticated description [29] is therefore not attempted. The experimentally observed average parallel velocities, $\overline{v}_{||}$, correspond to effective temperatures of the source (not to be confused with the parallel translational temperature) that are (except for He) clearly above room temperature, probably due to heating of the gas mixture by the intense current pulses used for operating the valve. A similar observation is reported by others for these pulsed valves [30].

Table 2.1: *Parameters characterizing the molecular beam for various binary 5% CO/rare gas mixtures. The average parallel velocity ($\overline{v}_{||}$), the parallel translational temperature ($T_{||}$) and the associated parallel speed ratio ($S_{||}$), the FWHM of the perpendicular velocity distribution ($\Delta v_\perp$) and the rotational temperature (T_{rot}) are given.*

Carrier gas	$\overline{v}_{\|\|}$ (m/s)	$T_{\|\|}$(K)	$S_{\|\|}$	$\Delta v_\perp$ (m/s)	T_{rot} (K)
He	1560 ± 10	2.2 ± 0.2	16.0 ± 1.2		15.0 ± 2.0
Ne	840 ± 5	2.1 ± 0.2	20.3 ± 1.5	16.3 ± 0.9	4.7 ± 0.3
Ar	600 ± 4	2.4 ± 0.2	19.1 ± 1.4	16.4 ± 1.2	5.2 ± 0.3
Kr	450 ± 3	3.9 ± 0.3	16.1 ± 1.2		3.7 ± 0.3
Xe	370 ± 2	3.5 ± 0.3	17.4 ± 1.3	17.6 ± 1.6	3.3 ± 0.3

The rotational temperature, T_{rot}, of the CO molecules in the molecular beam is determined from excitation spectra measured for all the gas mixtures. An example of an excitation spectrum is given in Fig. 2.6 for a mixture of 10% CO in Ar, as it has a slightly better signal to noise ratio than the 5% CO/rare gas mixtures. On the horizontal axis the absolute laser frequency (in cm^{-1}) is indicated while vertically the time-integrated TOF-signal intensity is shown. The upper trace shows the measured excitation spectrum in the region of the most intense Q_2 and R_2 lines of ^{12}CO. Several lines of the ^{13}CO isotope, present in the gas mixture at a natural abundance of 1.1%, are indicated in the

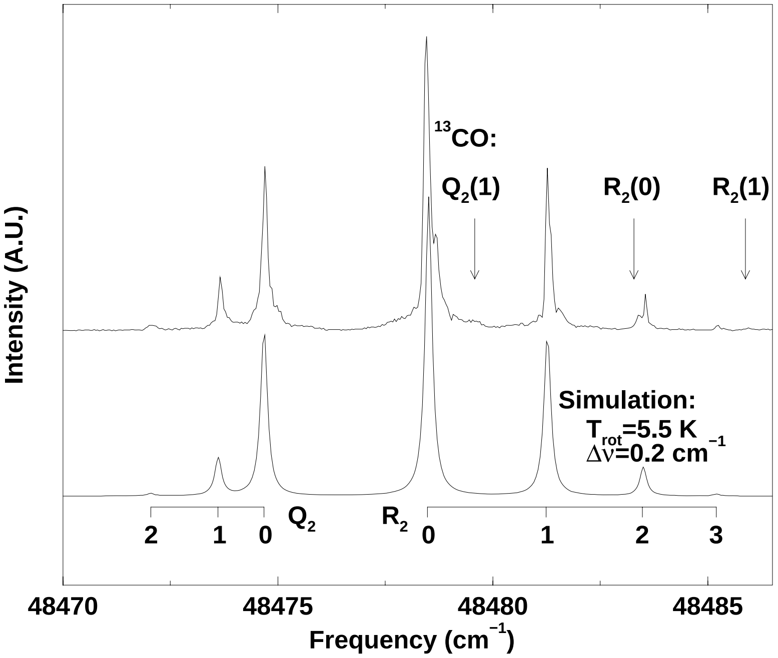

Figure 2.6: *Upper trace: Excitation spectrum of a mixture of 10% CO in Ar in the region of the most intense Q_2 and R_2 lines of ^{12}CO. The time-integrated TOF-signal intensity is plotted against the absolute laser frequency. The strongest lines of the ^{13}CO isotope, present at a natural abundance of 1.1%, are indicated in the spectrum by vertical arrows. Lower trace: Best fitting simulated spectrum assuming a Lorentzian laser profile with a FWHM of $\Delta\nu$ = 0.2 cm^{-1}. A rotational temperature T_{rot} = 5.5 K is found.*

experimental spectrum by vertical arrows. The lower trace shows the corresponding simulated spectrum of ^{12}CO, using the known transition frequencies [18] and relative transition strengths [19] and assuming a Boltzmann distribution for the population of the rotational levels in the electronic and vibrational ground state. The spectrum is best simulated with a rotational temperature T_{rot}=5.5 K and a Lorentzian laser profile with a Full Width at Half Maximum (FWHM) of 0.2 cm^{-1}. Since the residual Doppler width in the molecular beam is about two orders of magnitude smaller than the laser bandwidth, the lineshape in the excitation spectra is solely determined by the laser. The rotational temperatures as found via this procedure are given in the last column of Table 2.1 for all the gas mixtures used in the TOF experiments.

To determine the velocity distribution of the CO molecules perpendicular to the molecular beam axis, the laser-prepared metastable CO molecules are detected spatially resolved. Two-dimensional images showing the spatial distribution of CO in the molecular beam in a grey scale representation are displayed in Fig. 2.7 for mixtures of 5% CO in He, Ne, Ar and Xe. To record these 2D-images the MCP detector is gated to integrate over only the most intense part of the TOF-signal intensity; typically a gate with a width of 10% of the mean arrival time is used. The images are averaged over 10^4 laser shots with the laser resonant on the $R_2(0)$ transition while a background image, recorded without laser

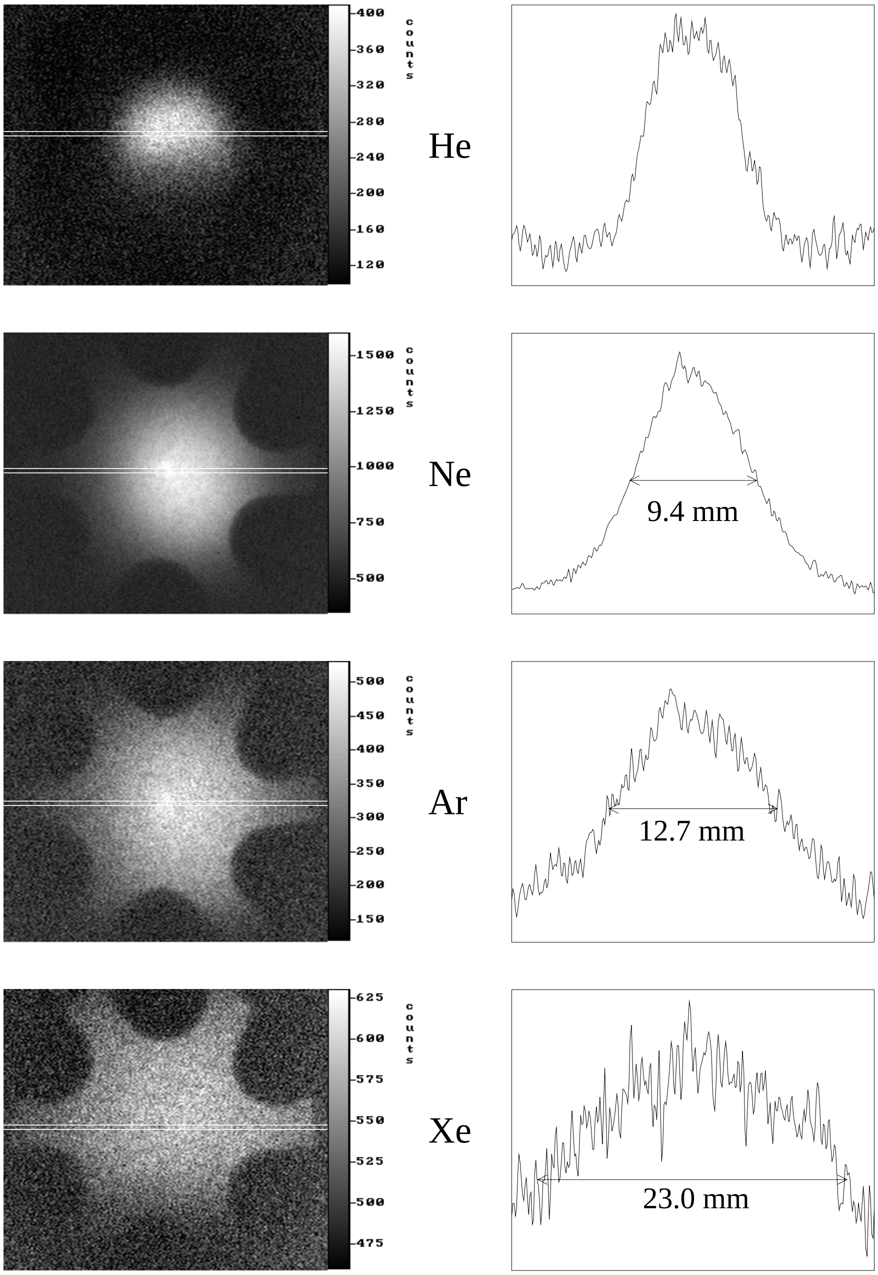

Figure 2.7: *Two-dimensional images (26.9 mm x 23.3 mm) showing the spatial distribution of CO in the molecular beam for mixtures of 5% CO in He, Ne, Ar and Xe. The grey scale associated with the pixel intensity on the detector is indicated next to the images. In most of the 2D-images the 'shadow' of the hexapole-rods is clearly visible.*
The series of images demonstrates the mass-focusing effect by which in a molecular beam of a binary mixture the heavier species is concentrated on the molecular beam axis. On the right-hand side the horizontal intensity profiles of the corresponding 2D-images are shown, averaged over the 6 horizontal lines near to the center of the image, indicated between the white lines in the images. The FWHM of the spot on the detector (in mm) is indicated for those profiles that can be accurately fit using a simple Gaussian perpendicular velocity distribution.

excitation, is subtracted. The size of the images corresponds to a detector area of 26.9 mm x 23.3 mm (300 x 260 pixels on the CCD chip). The grey scale associated with a certain pixel intensity on the detector is indicated next to the images. The images are smoothed by Fourier filtering techniques to eliminate the high frequency noise and are corrected for a somewhat higher sensitivity in a small central spot, caused by local cleaning of the MCP detector in the hexapole focus.

In most of the 2D-images of Fig. 2.7 the 'shadow' of the hexapole-rods is clearly visible. The actual distance between two opposite hexapole rods is 8.0 mm, which appears as an enlarged 14.4 ± 0.3 mm distance on the detector due to the experimental geometry. It is evident from these images that the molecular beam is slightly misaligned from the center of the hexapole. The series of images displayed in this figure demonstrates the mass-focusing effect, i.e. the effect that in a molecular beam of a binary mixture the heavier species is concentrated on the molecular beam axis [28]. In this series of images it is seen that the width of the CO distribution in the beam increases with increasing mass of the carrier gas; for the lightest carrier gas, He, the 'shadow' of the hexapole-rods is not even visible. On the right-hand side of the figure the horizontal intensity profiles of the corresponding 2D-images are shown. These profiles are averaged over the 6 horizontal lines near to the center of the image. This area is indicated between the white lines in the images. Except for the He image, the shape of the profiles is accurately described by a Gaussian curve, and the resulting FWHM of the best-fit is indicated (in mm) in the figure. The corresponding FWHM of the perpendicular Gaussian velocity distribution, $\Delta v_\perp$, is given in Table 2.1.

The observed mass-focusing effect can be explained in a rather simple model [28]. As the collisions between CO molecules and carrier gas atoms in the expansion exchange essentially velocity along the molecular beam axis the velocity of the CO molecules in this direction adapts to the velocity of the carrier gas, as is demonstrated in the TOF distributions shown in Fig. 2.5. The velocity distribution perpendicular to the molecular beam axis is mainly determined by the initial velocity of the CO molecule, however, implying a perpendicular velocity distribution that is independent of the carrier gas, in agreement with the values of $\Delta v_\perp$ in Table 2.1. This results in a spatial width of the CO distribution in the molecular beam that scales linearly with $1/\overline{v}_{||}$, as observed for CO seeded in Ne, Ar and Xe.

In the interpretation of the experimental observations it is assumed that no disturbing collisions take place between the laser excitation region and the detector. For the heavy carrier gasses, possible disturbing effects related to shock waves in the source chamber can be circumvented by exciting CO molecules in the front part of the short gas pulse. For Ne, for instance, the gas pulse has a length of about 2.5 cm, which is shorter than the skimmer length, so shock waves can have formed only after passage of the excited molecules through the skimmer. In the faster He beam, however, shock waves can not be completely avoided, which probably is the explanation for the relatively high rotational temperature, for the unexpectedly low parallel velocity and for the non-Gaussian perpendicular velocity distribution.

Hexapole focusing

Prior to discussing the experimental observations, a description of the trajectories of metastable CO molecules through a hexapole field is given. The electrostatic potential in an *ideal* hexapole is given by [6]

$$V = \frac{V_0}{2}\left(\frac{r}{r_0}\right)^3 \cos 3\phi \tag{2.3}$$

where r and ϕ are the cylindrical coordinates (the z-axis coincides with the axis of the hexapole, z=0 at the beginning of the hexapole), V_0 is the voltage difference between neighbouring rods and r_0 is the inner radius of the hexapole. The azimuthal angle ϕ is zero in the direction of the center of one of the hexapole-rods. The electric field $\vec{E}$ derived from this potential is

$$\vec{E} = (-3\frac{V_0}{2}\left(\frac{r^2}{r_0^3}\right)\cos 3\phi,\ 3\frac{V_0}{2}\left(\frac{r^2}{r_0^3}\right)\sin 3\phi,\ 0) \tag{2.4}$$

in the (r, ϕ, z) cylindrical coordinates. The Stark splitting of the energy levels in the $a^3\Pi_\Omega$ state only depends on the absolute value of the electric field $|\vec{E}|$ which, in the ideal hexapole, is independent of ϕ. The magnitude of the Stark shift of a Λ-doublet level ΔW_{Stark} relative to the zero-field energetic center of the Λ-doublet components is given by [22]

$$\Delta W_{Stark} = \left(\left(\frac{\Lambda}{2}\right)^2 + (E_{Stark})^2\right)^{1/2} \tag{2.5}$$

In this expression Λ is the magnitude of the Λ-doubling and E_{Stark} is the first order Stark effect in an electric field $\left|\vec{E}\right|$, given by

$$E_{Stark} = -\mu_{el}\left|\vec{E}\right|\frac{M\Omega}{J(J+1)} = -\mu_{el}3\frac{V_0}{2}\left(\frac{r^2}{r_0^3}\right)\frac{M\Omega}{J(J+1)} \tag{2.6}$$

containing the electric dipole moment μ_{el}, the absolute value of the electric field and the quantum numbers Ω, J and M. The force exerted by a hexapole field on the CO molecules is determined by the gradient of ΔW_{Stark}, resulting in the equation of motion

$$m_{CO}v_{\|}^2\frac{d^2r}{dz^2} = -\frac{|E_{Stark}|}{\Delta W_{Stark}}\frac{dE_{Stark}}{dr} \tag{2.7}$$

in which m_{CO} is the mass of the CO molecule. It should be noted that there is only a radial force present in the ideal hexapole.

In the high electric field limit, ΔW_{Stark} can be approximated by $|E_{Stark}|$, resulting in an equation of motion according to which the CO molecules describe a sinusoidal path in the hexapole field. Although this high electric field approximation is commonly made, it is not valid for the present experimental situation. The electric field near the center of the hexapole is rather low resulting in a value for E_{Stark} comparable to Λ, causing a deviation from a sinusoidal path of the CO molecules [8, 16].

It has already been mentioned, and it is also clear from the above equations, that only metastable CO molecules with a positive Stark effect (the upper Λ-doublet component with $M\Omega<0$) can be focused, while a negative Stark effect (the lower Λ-doublet component, with $\mathrm{M}\Omega>0$) leads to defocusing of the molecules. From the excitation scheme in Fig. 2.3 it follows that Q_2 lines have to be used to produce $a^3\Pi_1$ metastable CO molecules that can be focused by the hexapole. The $M=0$ levels of the $a^3\Pi_1$ state and the ground state CO molecules (where $\Lambda=\Omega=0$) can barely be deflected, if at all. This implies that by using the hexapole the number of metastable CO molecules can be enhanced with about a factor of 100 relative to the number of ground state CO molecules and that single $a^3\Pi$ (Ω,J,M) quantum states can be selected.

In Fig. 2.8, two-dimensional images of the distribution of the laser prepared metastable CO molecules in the molecular beam are shown as a function of the voltage on the hexapole-rods. Laser excitation is performed on the $Q_2(1)$ transition in a mixture of 5% CO seeded in Kr. The size of the displayed images corresponds to a 12.6 mm x 12.6 mm area on the detector (140 x 140 pixels on the CCD chip; smaller than in the mass-focusing images). The images are averaged over 10^4 laser shots with a background subtracted. To prevent saturation effects on the CCD chip, the 6 kV focusing image has been averaged over 5000 shots only. The images are smoothed by Fourier filtering techniques and corrected for the increased sensitivity of the MCP detector at the spot of the hexapole focus. Separate grey scales, associated with the pixel intensity on the detector, are given for each image. The series of images shows a clear ring-pattern in the under-focused situation (4 kV; 5 kV), a sharp spatial focus at a hexapole voltage of 6 kV and again a broader distribution in the over-focused situation (8 kV). Attention is drawn to the apparent rotation of the six-fold symmetry in the 2D-images over 30° in going from the under-focused to the over-focused situation (dashed hexagons are indicated to guide the eye). This effect will be explained below. Vertical profiles taken along the white line in the 2D-images are shown as the upper trace in the plots next to the images. The lower trace in each of these plots shows the profiles as calculated using the aforementioned hexapole focusing theory. To obtain the calculated profiles, the equation of motion (2.7) is solved numerically. All input parameters for this calculation are known experimentally so there are no adjustable parameters. The geometry of the molecular beam machine, the voltage applied to the hexapole rods, the gating on the MCP detector, the parallel velocity distribution as derived from the TOF measurements, the perpendicular velocity distribution as derived from the (unfocused) 2D-images, the quantum numbers of the laser prepared metastable levels as well as the magnitude of the Λ-doubling are used as input in the calculation of the profiles. The hexapole field is assumed to switch on and off abruptly at the beginning and end of the hexapole, respectively. For the under-focused situation the calculated profiles match the experimental ones rather well. The width of the calculated focus at 6 kV is smaller than the experimentally observed width (0.8 mm FWHM) and the calculated profile in the over-focused situation does not agree that well with the observed profile, an effect we attribute to deviations of our field from an ideal hexapole field, as will be discussed below. The slight misalignment of the molecular beam with the axis of the hexapole will also give a minor deviation (image distortion due to 'spherical' aberration).

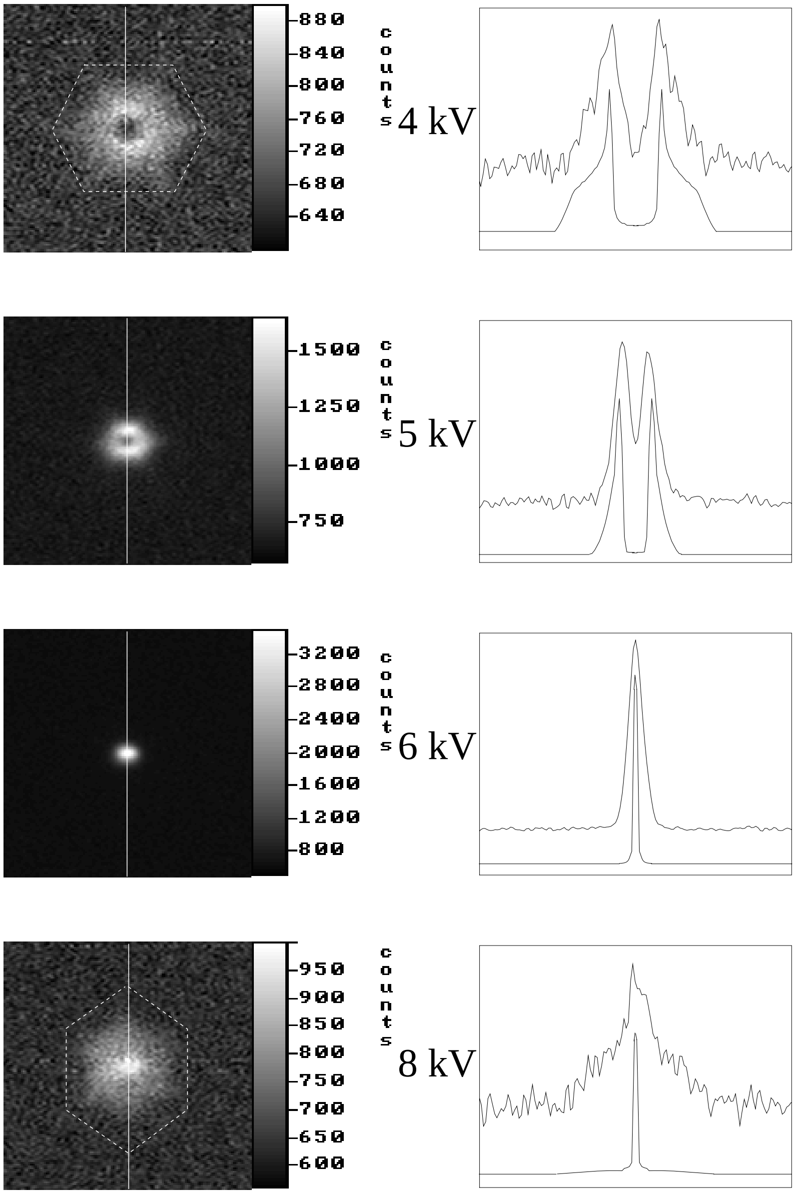

Figure 2.8: *Two-dimensional images (12.6 mm x 12.6 mm) of the distribution of metastable CO molecules (5% CO in Kr; $Q_2(1)$ excitation) in the molecular beam as a function of the voltage on the hexapole-rods. The series of images shows a clear ring-pattern due to the Λ-doubling in the under-focused situation (4 kV; 5 kV), a sharp spatial focus at a hexapole voltage of 6 kV and again a broader distribution in the over-focused situation (8 kV). Attention is drawn to the apparent rotation of the six-fold symmetry in the 2D-images over 30° in going from the under-focused to the over-focused situation, due to the ϕ-dependence of the radial force acting on the metastable CO molecules (dashed hexagons are indicated in the figure to guide the eye). Vertical profiles taken along the white line in the 2D-images are shown as the upper trace in the plots next to the images. The lower trace in each of these plots shows the profiles as calculated using the (ideal) hexapole focusing theory.*

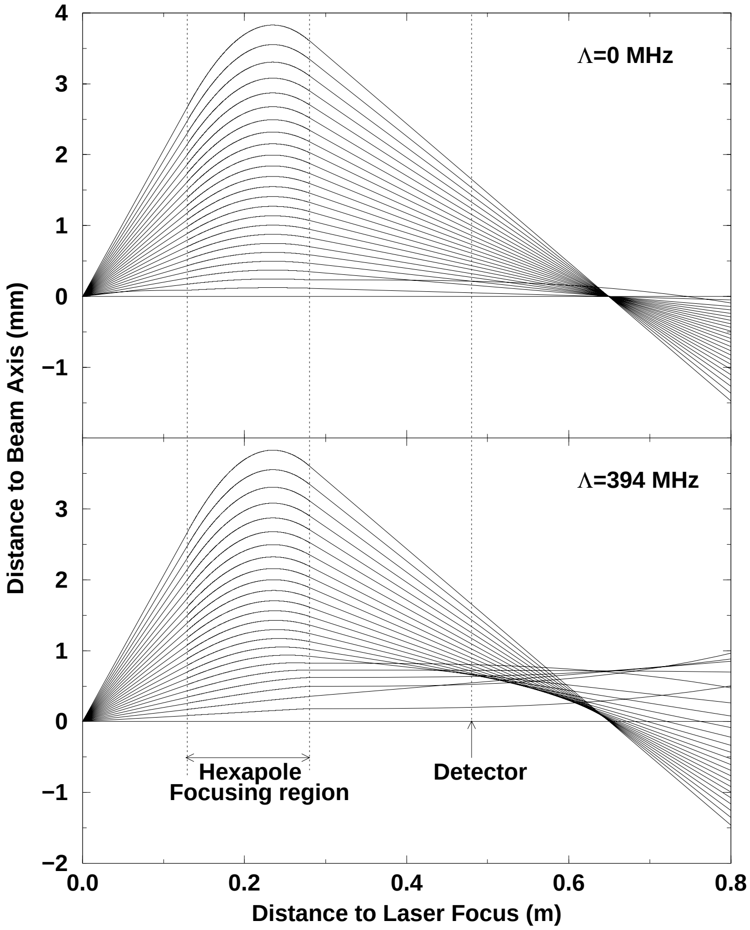

Figure 2.9: *These figures show the trajectories of metastable CO molecules, starting from the laser focus (distance in m), passing through the hexapole state-selector where the molecules are bend, and then again continuing in straight trajectories in the direction of the detector (distance to beam axis in mm). It is assumed in the calculations that the molecules all have the same absolute velocity. It is shown (upper figure) that molecules starting from one point, all flying with the same velocity, can be focused back in a single point for a purely linear Stark effect. If the Λ-doubling is taken into account (lower figure), one observes that in low electric fields the force on the molecules is reduced, leading to a ring-like pattern on the detector (since this is a 1-dimensional calculation, the calculated trajectory distribution has to be rotated around the beam axis to obtain the ring-like pattern).*

The observed ring-pattern in the under-focused situation, which is quantitatively reproduced in the calculations, is caused by the Λ-doubling. In the absence of Λ-doubling (or generally, in the high field approximation) all molecules coming from a point and entering the hexapole with the same velocity under various angles with respect to the hexapole axis can be focused in a point. This is explicitly shown in the upper part of Fig. 2.9, where trajectories have been calculated for metastable CO molecules in the $M\Omega$=–1 level. The high field limit for this situation is simulated by putting Λ=0. The molecules start from the laser focus, enter the hexapole focusing region, and continue in straight trajectories again after they have left the hexapole (distance to laser focus (beam axis) indicated in m (mm)). To obtain a 2D-distribution, this pattern has to be rotated around the beam axis because of the cylindrical symmetry. In the underfocused situation this leads to a homogeneous distribution on the detector for a pure linear Stark effect.

The lower part of Fig. 2.9 shows the result of trajectory calculations where the Λ-doubling is taken into account under otherwise identical circumstances as in the upper part of the figure. The presence of the Λ-doubling decreases the force exerted on the metastable molecules that are near the hexapole-axis relative to the force that would be present in the high electric field approximation (as can be directly seen from the Eqs. (2.5) and (2.7)). The result is that molecules close to the hexapole axis are obviously deflected less efficiently than is expected in the high field limit. By comparing both figures one can observe that for metastable molecules that are further away from the hexapole axis, where the high electric field approximation *is* valid, the trajectories are almost identical. If $\Lambda \neq 0$, evidently the 2D distribution shows a ring-like structure for the underfocused situation; the diameter of the ring at a certain hexapole voltage is a direct measure for the magnitude of the Λ-doubling.

A more accurate description of the electric field as well as of the equations of motion of dipolar molecules in a hexapole consisting of cylindrical rods has been given by Vonbun [16]. He showed that the gradient of the electric field in the radial direction inside such a hexapole has a ϕ-dependence, that becomes increasingly important for distances further away from the hexapole axis. This ϕ-dependence results in a radial force that is maximum for molecules that travel toward the center of a hexapole rod and minimum for molecules that travel in the direction in between hexapole rods. For the hexapole used in the present study the ratio of the maximum to the minimum value of $\frac{d|\vec{E}|}{dr}$ is calculated to be around 1.04 at a distance of 0.5 r_0, increasing to almost a factor 2 at a distance of 0.8 r_0 from the hexapole axis. This ϕ-dependence of the radial force is responsible for the already mentioned rotation of the 6-fold symmetry in the series of 2D-images.

In the 2D-images of Fig. 2.8 taken in the under-focused situation at 4 kV and 5kV it is seen that the six-fold symmetry is such that the image is somewhat less extended in the direction of the hexapole rods. This effect can be explained by the previously shown 'shadowing' effect of the hexapole rods (Fig. 2.7), i.e. by viewing the under-focused 2D-images as (ϕ-independently) compressed reproductions of the unfocused 2D-images shown in Fig. 2.7. Alternatively, this effect can be explained by (or at least will be enhanced by) the ϕ-dependence of the radial force acting on the metastable CO molecules. The ϕ-dependence of the radial force is held responsible for the apparent rotation of the image in the over-focused (8 kV) situation, however; molecules travelling in the direction of one of the hexapole rods will feel the strongest radial force and will therefore be deflected most efficiently and be bent away most strongly from the molecular beam axis in the over-focusing situation. An alternative explanation would invoke the presence of a velocity component in the ϕ-direction induced either by a force component in this direction which is present in our non-ideal hexapole field [16] or by misalignment of the molecular beam with respect to the hexapole axis. Such an explanation can be discarded, however, as the magnitude of the resulting rotation should change with the hexapole voltage and the parallel velocity of the CO molecules, something that has not been observed.

2.4.2 Beam characterization in the scattering chamber

Next, the UHV chamber is connected to the molecular beam machine via a 1.2 mm diameter diaphragm. The UHV chamber serves to study the scattering behaviour of metastable CO molecules. To avoid interfering effects due to either ground state CO molecules or due to carrier gas atoms a truly pure beam of state-selected metastable CO molecules is required. To obtain such a pure beam, a beamstop is centered on the molecular beam axis.

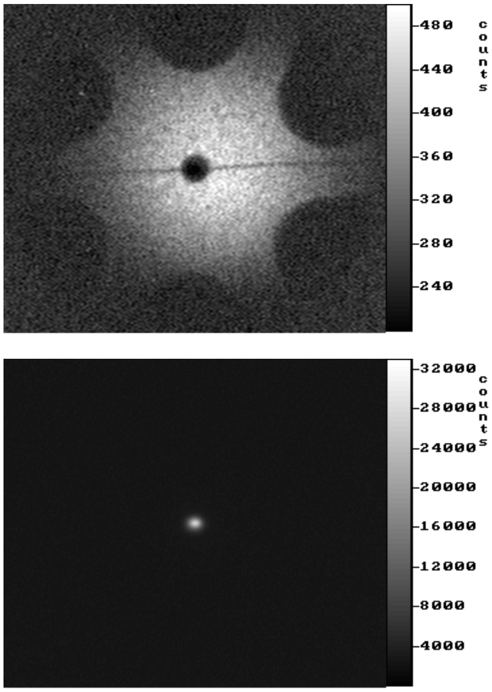

Figure 2.10: *Upper image: Distribution of metastable CO molecules in the beam (5% CO in Ar), with no voltage applied to the hexapole rods. Apart from the 'shadow' of the hexapole rods, the 'shadow' of the beamstop-assembly can be recognized. Lower image: The metastable CO molecules are bent around the beamstop and focused (12 kV) in a spot centered in its 'shadow'.*

In the upper image of Fig. 2.10, still recorded in the old configuration of the molecular beam machine without scattering chamber connected, the distribution of metastable CO molecules in the molecular beam (5% CO in Ar), with no voltage applied to the hexapole rods, is shown. Apart from the 'shadow' of the hexapole rods, the 'shadow' of the 1.2 mm diameter beamstop can be recognized, as well as of the 0.1 mm diameter wire to which this beamstop is attached. As is explicitly shown in the lower image of Fig. 2.10, the metastable CO molecules can be bent around this beamstop and focused in a spot centered behind the beamstop. A diaphragm with the appropriate dimensions (1.2 mm diameter) placed in the focal plane of the hexapole will therefore transmit only the pure state-selected metastable CO beam.

The distance of the diaphragm to the laser focus is chosen to be the same as the distance between the laser focus and the 2D-MCP detector in the above-mentioned experiments. Therefore, the spatial profile at the position of the diaphragm is accurately known. In the UHV chamber both time-resolved and spatially-resolved detection of metastable CO molecules can be performed. The MCP detector registers the intensity of the molecular beam of metastable CO molecules and can be used to optimize the transmission through the diaphragm by adjustment of the voltage applied to the hexapole rods and variation of the position of the diaphragm under operating conditions. The MCP based detection techniques can also be used to study the time- and spatial-profile of the molecular beam in the scattering chamber.

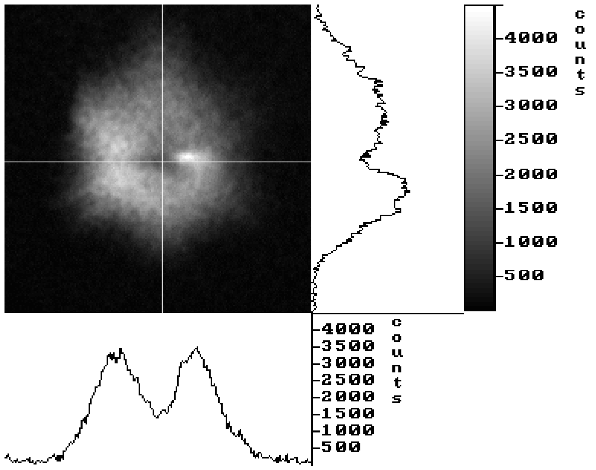

Figure 2.11: *Distribution of metastable CO molecules, detected at the end of the UHV chamber (image size: 18.8 mm x 18.8 mm). The 2D-image is recorded for 5% CO seeded in Ar, and a voltage of 12.75 kV applied to the hexapole rods. Both a horizontal and a vertical profile (indicated below and right of the image, respectively) taken along the white lines indicated in the figure, are displayed as well.*

A 2D-image of the shape of the molecular beam under optimized conditions is shown in Fig. 2.11. The image (time-integrated over the entire TOF profile) is obtained for a mixture of 5% CO in Ar. The horizontal and vertical profile (indicated below and left of the 2D-image) are taken along the white lines indicated in the 2D-image, and show a minimum in the middle. This minimum is not so much caused by the Λ-doubling but rather by the presence of the beamstop. The image shows the same structure as the overfocused image in Fig. 2.8. This is because the focus of the hexapole is located at the position of the diaphragm, and the molecular beam is increasing in size again in the scattering chamber. The diameter of the beam of metastable CO molecules in the center of the UHV chamber, where the scattering experiments are performed, is less than 3 mm. Figure 2.11 shows

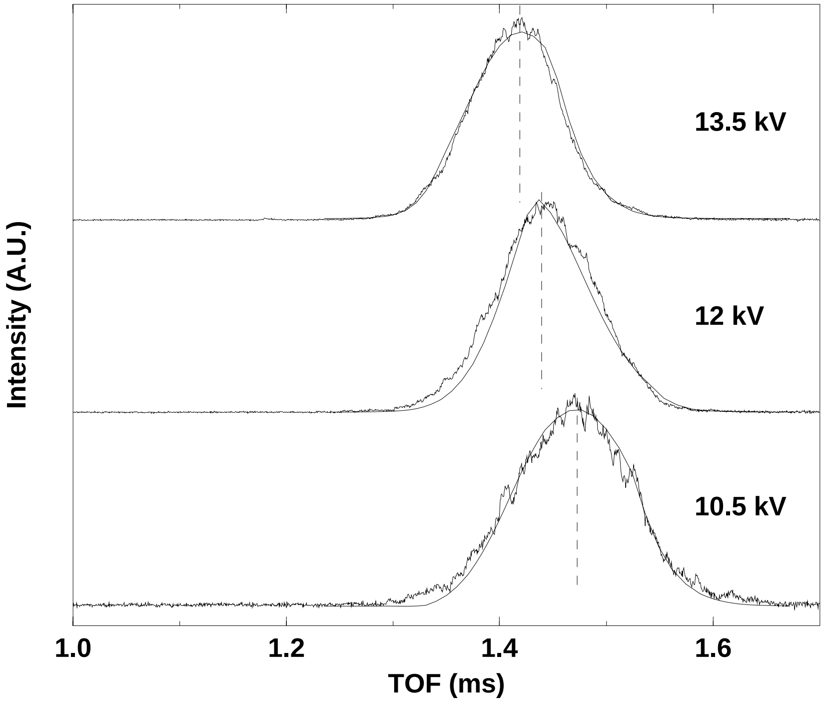

Figure 2.12: *TOF profiles as detected at the end of the UHV chamber for a mixture of 5% CO in Ar. The shift of the peak velocity with a change of the voltage applied to the hexapole rods demonstrates the velocity selection that is performed when the combination of a hexapole and a diaphragm is used. The smooth curves indicated in the figure are simulations obtained from trajectory calculations for an ideal hexapole field and taking the geometry of the machine into account.*

again the apparent rotation over 30° as the overfocused image of Fig. 2.8, but much more pronounced.

TOF profiles have been recorded in the UHV chamber as well. Figure 2.12 shows three of these profiles, recorded for 5% CO seeded in Ar and for different voltages applied to the hexapole rods. Calculated TOF profiles, again obtained by solving the equation of motion (2.7) for a number of trajectories and taking the geometry of the machine into account, are superimposed on the experimental profiles. It is clear that the peak velocity is slightly changed by changing the voltage that is applied to the hexapole rods. It follows from Eqs. (2.6) and (2.7) that in the high field limit the velocity for optimum focusation scales with $\sqrt{V_0}$. The velocity of the metastable CO beam in the UHV chamber can therefore be scanned over the velocity range present in the hexapole chamber by changing the focusing voltage. As a result, the velocity distribution of the pure beam of metastable CO molecules in the UHV chamber is slightly narrower than the velocity distribution in the molecular beam machine.

2.5 Conclusions

Metastable $a^3\Pi$ CO molecules can be state-selectively prepared and sensitively detected on a MCP detector via Auger deexcitation allowing both time- and spatially-resolved measurements. The combination of these techniques is used for a straightforward characterization of a molecular beam and parallel and perpendicular velocity distributions as well as rotational temperatures are determined. A direct 2D demonstration of the mass-focusing effect in a binary gas mixture is given.

After passage through a hexapole field, two-dimensional imaging of the spatial distribution of the metastable $a^3\Pi$ CO molecules in the beam is used to study hexapole focusing performance. Structured 2D-images demonstrate the dependence of the focusing characteristics on the magnitude of the Λ-doubling and on the angular dependence of the focusing force in a realistic hexapole consisting of cylindrical rods. It is demonstrated that the combination of a hexapole, a beamstop and a diaphragm allows preparation of a pure beam of metastable CO molecules, ideally suited for scattering experiments.

Laser preparation of quantum-state selected metastable molecules in combination with time- and spatially-resolved detection of the metastable species holds great promise in fields like photo-dissociation dynamics and reactive and (in)elastic scattering. Compared to ion-imaging techniques, metastable imaging has the advantage that problems related to space-charge effects and to the presence of spurious electric and/or magnetic fields are avoided.

Acknowledgements

We thank Prof. Dr. D.H. Parker and Dr. J.J. ter Meulen for useful discussions and helpful suggestions and C.A. Sikkens, J.G.H. Hermsen and C.A. Timmer for technical support. We acknowledge LaVision GmbH (Göttingen, Germany) for lending us the 2D-imaging detector as well as for software support.

References

[1] R.K. Hanson, J.M. Seitzman, and P.H. Paul, Appl. Phys. B. **50**, 441 (1990).

[2] P. Andresen, G. Meijer, H. Schlüter, H. Voges, A. Koch, W. Hentschel, W. Oppermann, and E. Rothe, Appl. Opt. **29**, 2392 (1990).

[3] D.W. Chandler and P.L. Houston, J. Chem. Phys. **87**, 1445 (1987).

[4] T.N. Kitsopoulos, M.A. Buntine, D.P. Baldwin, R.N. Zare, and D.W. Chandler, Science **260**, 1605 (1993).

[5] J.M. Price, A. Ludviksson, M. Nooney, M. Xu, R.M. Martin, and A.M. Wodtke, J. Chem. Phys. **96**, 1854 (1992).

[6] K.H. Kramer and R.B. Bernstein, J. Chem. Phys. **42**, 767 (1965).

[7] *Atomic and Molecular Beam Methods*, Vol. I, ed. G. Scoles, (Oxford University Press, New York, 1988).

[8] J. Reuss, (1988), See [7], 276-292.

[9] S. Stolte, (1988), See [7], 631-652.

[10] E.W. Kuipers, M.G. Tenner, A.W. Kleyn, and S. Stolte, Phys. Rev. Lett. **62**, 2152 (1989).

[11] S.R. Gandhi and R.B. Bernstein, J. Chem. Phys. **88**, 1472 (1988).

[12] J.W.G. Mastenbroek, C.A. Taatjes, and S. Stolte, J. Phys. Chem. **99**,4360 (1995).

[13] S.R. Gandhi, T.J. Curtiss, Q. Xu, S.E. Choi, and R.B. Bernstein, Chem. Phys. Lett. **132**, 6 (1986).

[14] F. Harren, D.H. Parker, and S. Stolte, Comments At. Mol. Phys. **26**, 109 (1991).

[15] W.C. Wiley and I.H. McLaren. Rev. Sci. Instrum. **26**, 1150 (1955).

[16] F.O. Vonbun, J. Appl. Phys. **29**, 632 (1958).

[17] G. Herzberg, *Spectra of Diatomic Molecules*, Second edition, (Van Nostrand Reinhold Co., New York, 1950).

[18] R.W. Field, S.G. Tilford, R.A. Howard, and J.D. Simmons, J. Mol. Spectrosc. **44**, 347 (1972).

[19] T.C. James, J. Chem. Phys. **55**, 4118 (1971).

[20] G. Meijer, A.M. Wodtke, H. Voges, H. Schlüter, and P. Andresen, J. Chem. Phys. **89**, 2588 (1988).

[21] R.T. Jongma, M.G.H. Boogaarts, and G. Meijer, J. Mol. Spectrosc. **165**, 303 (1994).

[22] R.C. Stern, R.H. Gammon, M.E. Lesk, R.S. Freund, and W.A. Klemperer, J. Chem. Phys. **52**, 3467 (1970).

[23] M. Drabbels, S. Stolte, and G. Meijer, Chem. Phys. Lett. **200**, 108 (1992).

[24] H.D. Hagstrum, Phys. Rev. **96**, 325 (1954).

[25] H. Brenten, H. Müller, K.H. Knorr, D. Kruse, H. Schall, and V. Kempter, Surf. Sci. **243**, 309 (1991).

[26] H.D. Hagstrum, Phys. Rev. **96**, 336 (1954).

[27] B. Woratschek, W. Sesselmann, J. Küppers, G. Ertl, and H. Haberland, Phys. Rev. Lett. **55**, 1231 (1985).

[28] D.R. Miller, (1988), See [7], 14-53.

[29] H.C.W. Beijerinck, G.H. Kaashoek, J.P.M. Beijers, and M.J. Verheijen, Physica 121, 425 (1983).

[30] M.G.H. Boogaarts, Ph.D. thesis, University of Nijmegen (1996).

Chapter 3

Detection Schemes for Metastable CO Molecules and Determination of the Radiative Lifetime

Abstract

Several detection schemes for metastable CO molecules are investigated. Auger deexcitation followed by detection of the electrons and detection of the a→X fluorescence are shown to be straightforward, generally applicable techniques for detection of metastable CO molecules. A (1+1)-REMPI scheme via the $b^3\Sigma^+$ state is demonstrated to be a very sensitive, state-selective technique for detection of metastable CO molecules. The radiative lifetime of the $a^3\Pi_1(J{=}1)$ level is determined via two different techniques: direct absorption and dispersion measurements yield a lifetime of $3.6_7 \pm 0.4$ ms, while recording the fluorescence signal at two positions in a molecular beam leads to a lifetime of 1.08 ± 0.15 ms for this same level. The difference might be explained by collisional quenching in the beam.

3.1 Introduction

In this chapter several detection schemes for metastable (i.e. long lived, electronically-excited) CO molecules are described. Simple and more complicated schemes for detection of these molecules in the excited state are discussed, together with the advantages and disadvantages of the different techniques. An overview of possible detection schemes for metastable species is given by Hotop [1]. Detection schemes for metastable atoms or molecules often exploit the long lifetime or the relatively high internal energy of the particle. The techniques as discussed can be distinguished in two categories. Techniques in the first category are based on deexcitation of the metastable species. Examples are electron emission detectors, penning ionization of gas targets, radiative decay, and collision induced photon emission. Laser-induced excitation and ionization schemes belong to the second category and are used for more sensitive and also state selective detection of metastable species. For CO, ionization schemes are relatively difficult because the Ionization Potential (I.P.) is rather high, and even for the metastable state 8 eV is required to reach the I.P. Examples of detection techniques from both categories, applied to metastable CO molecules, are presented in this chapter.

We also report on experiments to determine the radiative lifetime of the metastable state in CO. The determination of the radiative lifetime of metastable states in molecules is in general not easy. Conventional gas phase techniques measure the decay time of the fluorescence signal in a molecular beam or in a cell, but these techniques are only applicable for radiative lifetimes up to several microseconds. For the determination of the radiative lifetime of metastable states there are some extra difficulties. First, the preparation of single quantum levels in the excited state using direct laser excitation is difficult because the transition to the excited state is very weak, inherent to being a metastable state. Second, molecules with long lived excited states may escape from the detection region. And third, the population can be redistributed over other levels due to quenching during their lifetime.

Direct absorption measurements provide a general applicable technique to measure lifetimes and are also applicable to measure the lifetime of long lived excited states. For this it is needed that all decay and relaxation channels from the excited state are known. In practice, this means that all possible relaxation channels to dark and dissociative states and radiative relaxation channels must be known.

In the early 1970's calculations and many experiments have been performed to determine the lifetime of the $a^3\Pi$ state of CO. The interest in metastable CO molecules was triggered by the presence of strong features of the Cameron bands of CO in the emission spectrum of Mars. James calculated the oscillator strength to, and the corresponding lifetime of, the $a^3\Pi(v{=}0)$ state assuming spin-orbit coupling to the $A^1\Pi$ [2] state. He found a value of $f_{0,0}{=}1.63{\cdot}10^{-7}$ and an averaged electronic lifetime (assuming an equal distribution of intensity over each Λ-doublet component in each Ω-ladder) of $\tau_{av}{=}8.75$ ms. In this model the radiative lifetime of the metastable CO molecules depends strongly on the rotational quantum number.

Various experiments in that same period claim a high degree of accuracy [3–8] and give oscillator strengths that correspond to averaged lifetimes between 1 ms and 9.4 ms.

This averaged lifetime is normally obtained from cell experiments, where generally a large number of rotational levels is populated in the upper state, and pressures are such that collisional redistribution occurs within the lifetime of the excited state.

For the interpretation of the results of the scattering experiments as reported in chapter 5 and 6 of this thesis, not knowledge of the averaged lifetime, but knowledge of the lifetime for single ro-vibrational levels in the $a^3\Pi(v{=}0)$ state is required.

3.2 Detection of CO($a^3\Pi$) with a MCP detector

Figure 3.1 shows all of the electronic states that are relevant for the preparation and detection of metastable CO as presented here. The metastable CO molecules are prepared from the electronic ground state. The spin-forbidden transition for preparation of the metastable CO molecules is to the $a^3\Pi$ state. The $a^3\Pi$ state is weakly perturbed by the $A^1\Pi$ state via spin-orbit coupling. The spin-forbidden $a^3\Pi \leftarrow X^1\Sigma^+$ transition therefore borrows intensity from the $A^1\Pi \leftarrow X^1\Sigma^+$ transition due to the amount of $^1\Pi$ character in the wavefunction of the $^3\Pi$ state. The selection rules for the a←X Cameron band are therefore identical to those of a $^1\Pi \leftarrow ^1\Sigma^+$ transition. In the pure Hund's case (a) description this implies that only transitions to the $\Omega{=}1$ manifold of the $a^3\Pi$ state are allowed.

A straight forward detection scheme is based on detection of electrons that are produced upon impact of a metastable CO molecule on surfaces that have a workfunction that is lower than the electronic energy of CO in its $a^3\Pi$ state, e.g. at the surface of a Micro-Channel Plate (MCP) detector. In this detection scheme the electronic energy of the metastable CO molecules (6.0 eV) causes the release of electrons from the surface via an Auger deexcitation process [9]. The method allows time- and spatially-resolved detection of metastable CO molecules, as described in detail previously [10].

The efficiency of the MCP detector for measuring the metastable CO molecules is calibrated using a scheme as described by Hotop [1]. For calibration, metastable CO molecules are measured by the MCP detector simultaneously with ions produced by a second laser. The depletion of the metastable state in CO due to the ionization laser (measured on the MCP detector) can be directly related to the number of ions that is produced.

3.2.1 Experimental

The experiment is performed in a molecular beam machine [11] equipped with a high resolution Wiley-McLaren type Time-Of-Flight (TOF) mass spectrometer, as indicated in Fig. 3.2. A valve (R.M. Jordan Co.) releases gas pulses with a duration of 30 μs. For this experiment a gas mixture of 5% CO in Ar is used. After the expansion the pulsed molecular beam is collimated by a 1 mm ×4 mm slit-skimmer. The slit is placed vertically, i.e. perpendicular to the plane formed by the molecular beam axis and the direction of laser propagation, to reduce the size of the molecular beam in the excitation region along the direction of laser propagation. The molecular beam enters the TOF mass spectrometer between the two lowest extraction grids. Its field free flight tube has a length of 60 cm. The mass resolution under space-focusing conditions is $m/\Delta m{=}400$.

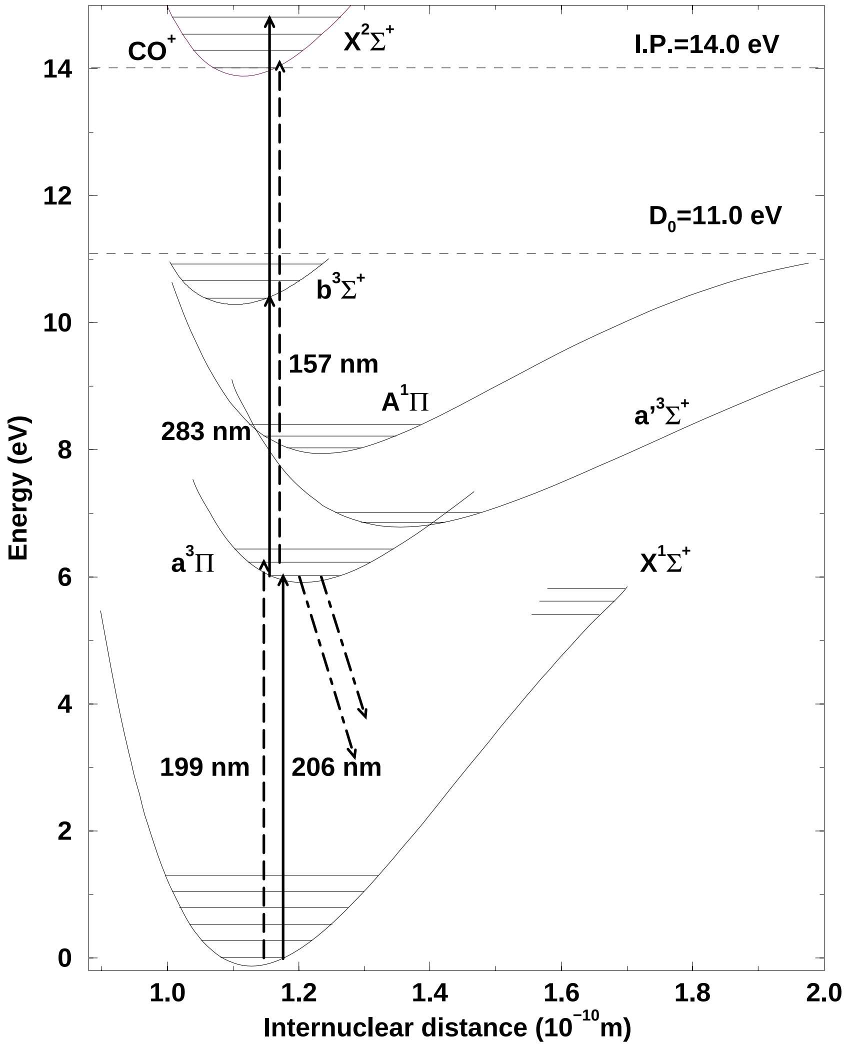

Figure 3.1: *All potential energy curves of CO and CO$^+$ that are relevant for the here presented detection schemes are shown. Metastable CO molecules can be produced from the electronic ground state via the spin-forbidden a←X transition (206/199 nm radiation is needed to prepare molecules in the v=0/v=1 level), which borrows intensity from the A←X transition. Apart from a detection scheme using Auger deexcitation, spontaneous fluorescence can be used for detection of the metastable CO molecules (indicated with dashed-dotted arrows). One and two photon ionization schemes from the metastable state are indicated by the dashed and solid arrows, respectively.*

In the excitation region a fraction of the ground state CO molecules is laser excited to the metastable a$^3\Pi(v=0)$ state via pumping on the Cameron band around 206 nm [12]. The R$_2$(0) line is employed to populate the – parity Λ-doublet component of the a$^3\Pi_1(v=0, J=1)$ level. The laser radiation needed to prepare the metastable CO molecules is obtained by frequency tripling the output of a pulsed dye-laser system (Spectra Physics GCR-11/PDL-2 combination), running on a mixture of Sulforhodamine 640 and DCM, in

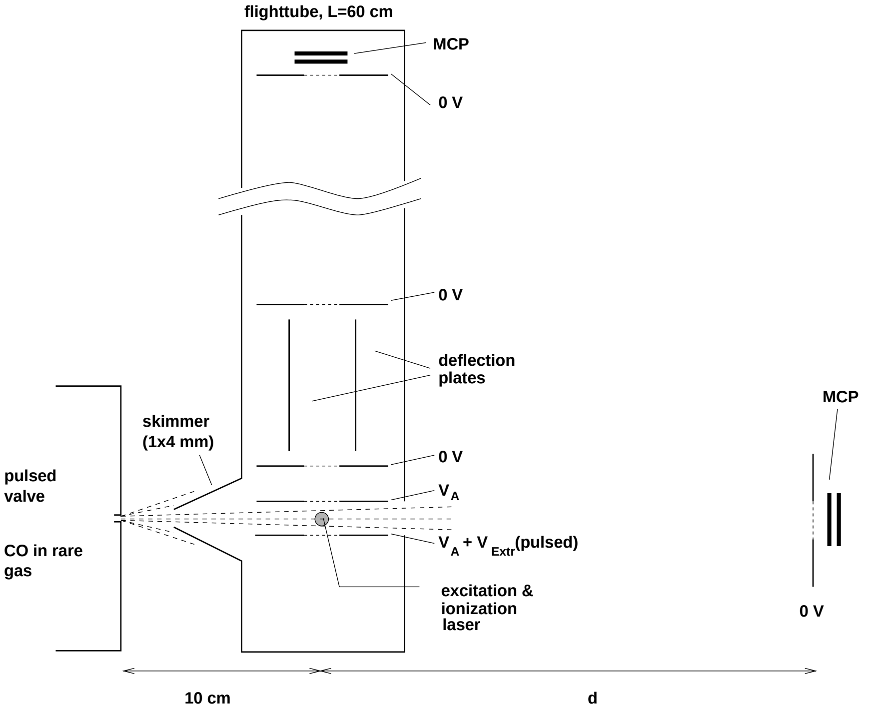

Figure 3.2: *Schematic view of the molecular beam machine. The pulsed molecular beam enters the mass spectrometer after passage through the skimmer. The ground state CO molecules are excited to the metastable* $a^3\Pi$ *state between the lower two grids of the mass spectrometer. They can either be ionized by a second laser and detected mass selectively in the Wiley-McLaren type mass spectrometer or they can leave the excitation region and be detected on the MCP detector which is mounted at a distance* d *from the excitation region.*

the combination of a KDP and a BBO crystal. The 206 nm laser radiation thus obtained (1 mJ/pulse, 0.5 cm^{-1} bandwidth) is focused in the excitation region with a 25 cm lens. The weak a←X transition is still not saturated under these conditions. The production of the metastable CO molecules is monitored with a 25 mm diameter MCP detector (R.M. Jordan Co.), placed at a distance d=40 cm downstream from the excitation region.

The CO($a^3\Pi$, v=0) molecules can be efficiently ionized in an ionization scheme (discussed in detail below) via the $b^3\Sigma^+(v{=}0)$ state, see Fig. 3.1. The 283 nm laser radiation needed for this (1+1)-Resonance Enhanced Multi-Photon Ionization (REMPI) scheme, is obtained by frequency doubling the output of a pulsed dye laser system (Spectra Physics GCR-150/PDL-3 combination) running on Fluorescein 548 in a KDP crystal. The 283 nm laser radiation passes anti-parallel to the 206 nm laser beam through the excitation region. The ionization laser is focused by a 40 cm lens and overlaps the focus of the 206 nm laser completely. The wavelength of the ionization laser is tuned to efficiently ionize the metastable CO molecules.

About 100 ns after the ionization laser is fired, the extraction field accelerates the ions into the field free flight tube of the mass spectrometer. The pulsed extraction voltage is applied using a fast (10 ns rise- and fall-time) high voltage switch, allowing preparation and excitation of the metastable CO molecules in a field free region. The ions are detected mass selectively with a MCP detector mounted at the end of the field free flight tube, identical to the one used for direct detection of the metastable molecules.

The signals of the MCP detectors are fed into a fast digital oscilloscope (Lecroy 9430) with a 10 bit vertical resolution and a 100 MHz sampling rate. The oscilloscope is read out by a PC (486) via a GPIB interface. Time-gates are placed around the signal to be detected and the averaged signal in the gate is recorded e.g. as a function of the laser frequency, which is controlled by the same PC. Pulsed valve, laser(s), and detection system are triggered by a delay generator (Stanford Research Systems DG535).

3.2.2 Results and discussion

With the 283 nm laser switched off, the MCP detector on the molecular beam axis registers 35±8 metastable CO molecules per laser pulse. The ionization laser, when switched on, is able to ionize 50% of the metastable CO molecules. The resulting ion signal, detected at the end of the mass spectrometer, corresponded to approximately $(11.0\pm2.5)\cdot10^3$ ions per laser pulse. Taking the transmission of each of the extraction grids into account (the total transmission through the grids of the mass spectrometer is 41%), and assuming a detection efficiency of unity once the ions reach the detector of the mass spectrometer, the efficiency of the MCP detector for detection of metastable CO($a^3\Pi$, v=0, J=1) molecules via the Auger deexcitation process is calculated as $(6.5\pm2)\cdot10^{-4}$.

The detection efficiency of the MCP for detection of metastable CO molecules is thus not very high, partly because the workfunction of the material at the surface of the MCP is rather high, and partly because not all the created electrons are detected; the electrons need to be created ín or close to the entrance of one of the channels. Surface contamination of the MCP detector also decreases the detection efficiency.

As the *electronic* energy (6 eV) of the metastable CO molecules is responsible for the creation of electrons at the surface of the MCP detector, the detection efficiency is expected to be essentially independent on rotational or kinetic energy of the metastable CO molecules. But even if part of the rotational or kinetic energy of the metastable CO molecules could be used in producing Auger electrons, the detection efficiency would only show a minor dependence on these quantities as it is only a small contribution to the total internal energy of the CO molecules.

3.3 Detection of the spin-forbidden $a^3\Pi\rightarrow X^1\Sigma^+$ fluorescence

A second, relatively easy, way to detect the metastable CO molecules utilizes their spontaneous fluorescence. Although the a→X electric dipole transition is very weak, as explained before, all molecules will eventually decay back to the electronic ground state via emission of photons (schematically indicated with the dashed-dotted lines in Fig. 3.1) in the absence of other deactivation mechanisms.

This Laser Induced Fluorescence (LIF) signal can be monitored with a photomultiplier

(PMT). The detection efficiency depends on the solid angle and the detection volume that can be monitored, as well as on the time that the metastable CO molecules spend in the detection region, i.e. on their velocity. It is noted that spatial filtering via a lens-pinhole-lens system, commonly used in LIF experiments to suppress background light, is unfavourable for detection of the weakly radiating metastable CO molecules because of the small detection volume registered.

It is possible to obtain a complete separation in time of fluorescence of the long lived metastable CO molecules and straylight caused by the laser; with a large detection volume probed, fluorescence measurements lead to sensitive detection of the electronically excited CO molecules.

3.3.1 Dispersion and absorption measurements

First, the branching ratios of the $a(v{=}0)\rightarrow X(v'')$ emission, previously calculated by James [2], are determined experimentally. Secondly, the absolute peak absorption cross-section of CO in an almost 2 m long, room temperature absorption cell is measured. The combination of absorption and dispersion measurements allows the absolute values of the Einstein coefficients to be determined and can be used to calculate the radiative lifetime of the $a^3\Pi$ state.

Experimental

The molecular beam machine in which the absorption and dispersion measurements are performed, is different from the one described above and has been explained in detail before [10]. A gas mixture of 20% CO seeded in Ar is expanded from a pulsed valve; the metastable CO molecules are produced in the source chamber, before the molecular beam is skimmed.

In these experiments a Pulsed Dye Amplified (PDA) laser system (Lambda Physik LPD3000), pumped by a Nd:YAG laser (Spectra Physics GCR-190 without injection-seeder), is used to excite the ground state CO molecules. The seeding of the PDA-system is performed with a single-mode cw ring dye laser system (Spectra Physics 380), pumped by an Ar-ion laser (Spectra Physics 2017). The output of the PDA-system (around 618 nm) is frequency tripled in the combination of a KDP and a BBO crystal, providing 0.5 mJ/pulse of 206 nm laser radiation in a bandwidth of 150 MHz (FWHM). The superior spectral brightness of this system compared to conventional pulsed dye lasers, makes this laser ideally suited for these experiments.

The spectral profile of this laser can be deduced from the spectrum shown in the upper trace of Fig. 3.3, which is recorded by monitoring the LIF signal with a PMT (detection area 1 in Fig. 3.4, see below) while scanning the preparation laser over the $Q_2(1)$ line of the $a\leftarrow X$ transition of CO. The 220 MHz wide peak (the convolution of the 150 MHz wide laser peak and the residual Doppler profile in the molecular beam) is superimposed on a broad background signal with an integrated intensity that is even larger than the integrated intensity of the narrow-band laser peak. This broad background signal is produced by the time-profile of the pulse delivered by the non-seeded Nd:YAG laser that is used to pump

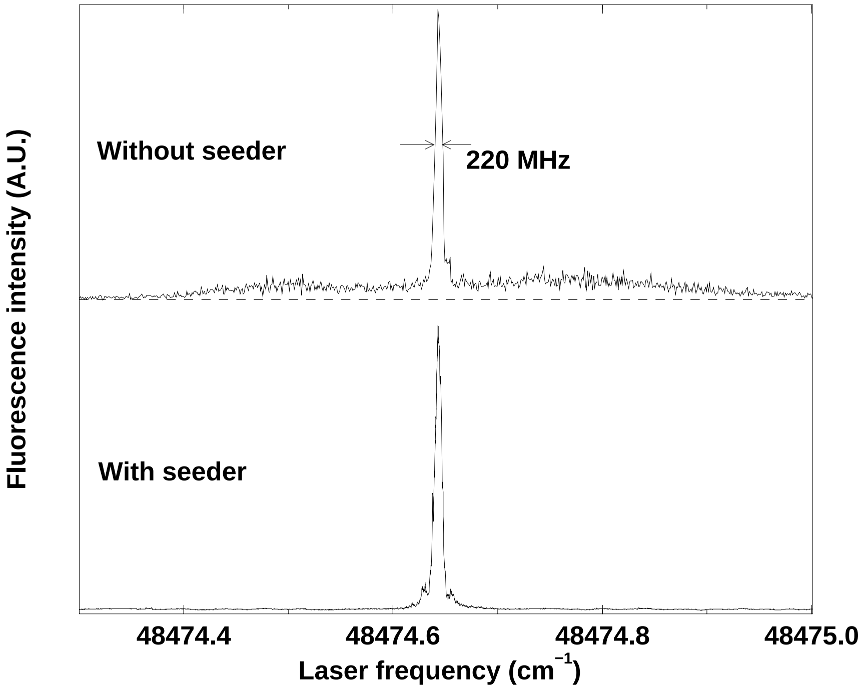

Figure 3.3: *LIF spectrum of metastable CO molecules as recorded in the molecular beam machine. The profile is the convolution of the laser profile with the residual Doppler profile in the molecular beam. Upper trace: LIF spectrum as obtained when the PDA system is pumped with a non-seeded Nd:YAG laser. Lower trace: LIF spectrum obtained when an injection-seeded Nd:Yag laser pumps the PDA system under otherwise identical circumstances.*

the PDA system. The time-profile of a laser pulse from an injection-seeded Nd:YAG laser is close to a Gaussian, while for a non-seeded Nd:YAG laser a number of spikes is obtained. Thus, the broad background signal is absent when an injection-seeded pump laser pumps the PDA system, as shown in the lower trace of Fig. 3.3. For this reason the use of an injection seeded Nd:YAG laser results in a more efficient production of metastable CO molecules (the injection-seeded Nd:YAG laser (Spectra Physics GCR-3) became available only in a later stage).

The broad background signal gives no problems while doing the dispersion measurements because the laser is kept fixed on top of an absorption line and only the resonant light is used. It gives difficulties, however, in direct absorption measurements when the laser is scanned over an absorption line: the background signal depends on the tuning of the BBO crystal and is therefore not constant during the scan and no correct baseline for zero absorption is obtained. These problems are circumvented in the experimental approach that we followed for the absorption measurements.

For the dispersed fluorescence measurements, the PDA system is used to excite the CO molecules 2 cm downstream from the nozzle before they pass through a 0.8 mm diameter skimmer. After the skimmer, in a second differentially pumped vacuum chamber, the spin-

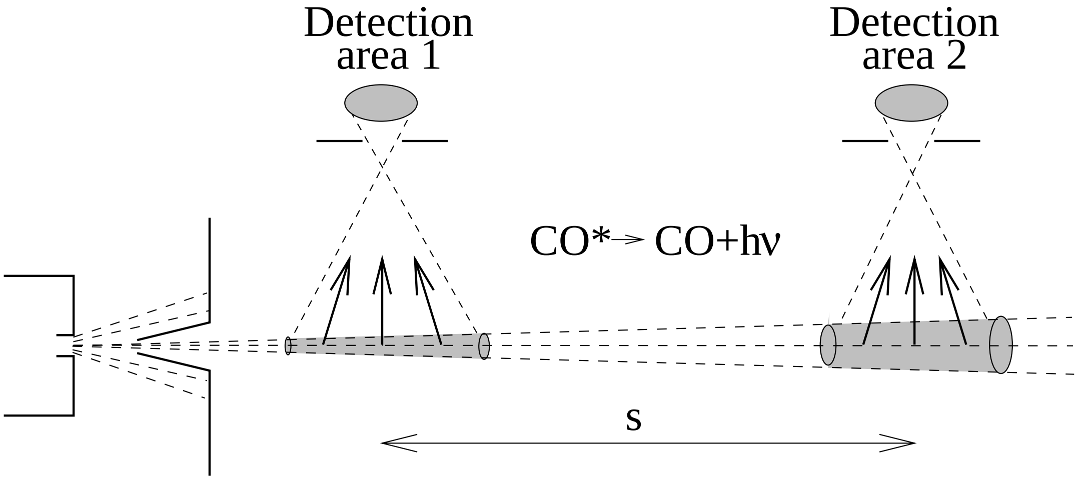

Figure 3.4: *Schematic representation of the two detection areas in the molecular beam that allow detection of the a(v=0)→X(v″) fluorescence signal of the metastable CO molecules. For the dispersion and absorption measurements, photons are detected in detection area 1, both in horizontal and vertical direction. For the two-point measurement of the radiative lifetime both detection areas indicated in the figure, separated by s=1 m, are used for fluorescence detection.*

forbidden fluorescence of the metastable CO molecules back to the electronic ground state is detected perpendicularly to the molecular beam axis, both in horizontal and vertical direction, at a distance of 7.5 cm downstream from the excitation region. The molecular beam machine is schematically depicted in Fig. 3.4. Here, only the fluorescence detection area directly after the skimmer is used.

The non-dispersed fluorescence that is emitted in horizontal direction is used as a calibration signal to correct for fluctuations. The fluorescence in vertical direction is collected by a lens, imaged on the entrance slit of the monochromator (Oriel 77250; resolution set to approximately 3 nm in the 200-300 nm region), and detected with a second PMT. Because the signal intensity is very low (averaged peak signal around 0.15 photon per laser pulse), a photon counting technique is used to measure the dispersed fluorescence spectrum. The oscilloscope sums typically over 100 laser shots; the PC then reads this signal out and counts the number of photons present in the time interval during which the molecules pass through the field of view of the monochromator/PMT combination. At each wavelength position of the monochromator the fluorescence intensity has been summed over 2400 laser shots to obtain the dispersed fluorescence spectrum. The frequency dependent sensitivity of the detection system is calibrated afterward in a cell experiment by the well known dispersed fluorescence spectrum of the $A^2\Sigma^+(v'=2)\rightarrow X^2\Pi(v'')$ transition in NO [13], which covers the same wavelength region as the dispersed fluorescence spectrum of CO ($a(v'=0)\rightarrow X(v'')$). The $A(v'=2)$ level of NO is prepared with laser radiation around 205 nm.

For the absorption measurements the molecular beam machine described above serves as a narrow-band monochromator to circumvent problems related to the spectral profile of the PDA laser pulse. The excitation laser is passed through a 1.76 m long absorption cell, where the actual absorption experiment takes place, prior to entering the molecular beam machine. This cell is filled with a total pressure of 0 to 10 Torr CO at room temperature. The pressure is low enough that only the Doppler width of 0.113 cm^{-1} (FWHM) has to be taken into account i.e. pressure broadening effects can be neglected. Only light that is transmitted through the cell and that is resonant with a transition in CO can become absorbed by CO molecules in the molecular beam on the condition that the ground state level is populated in the molecular beam. The residual Doppler width in the molecular beam is around 100 MHz due to the geometry of the machine. The fluorescence signal, measured with the PMT in detection area 1, is a direct measure for the amount of light at this specific frequency that is transmitted through the absorption cell.

By varying the pressure in the absorption cell while keeping the laser frequency on top of the molecular beam resonance, the absorption cross-section of specific transitions of the Cameron band ($R_2(1)$, $Q_2(1)$ and $Q_2(2)$) is measured (contributions of neighbouring lines are in all cases below 10^{-3} on top of the resonance). The fluorescence signal, corrected for laser intensity and measured as a function of pressure in the absorption cell, yields the cross-section for all the absorption lines. The technique employed for the absorption measurements is limited to absorption lines that are isolated, and start from levels in the electronic ground state that are sufficiently populated both in the absorption cell and in the molecular beam. Direct information is obtained, however, on exactly those levels that are relevant in the molecular beam studies reported in this thesis.

Results and discussion

Figure 3.5 shows the dispersed fluorescence spectrum of the $a(v'=0)\rightarrow X(v'')$ transition of CO obtained after excitation on the $Q_2(1)$ transition, thus preparing the + parity component of the $J=1$ level in the $a^3\Pi_1$ state. It follows from the selection rules that the fluorescence to the different vibrational levels in the electronic ground state can only occur via $Q_2(1)$ emission lines. Preparation of the – parity component of the same rotational level would lead to emission on P_2 and R_2 lines. The peaks in the dispersed fluorescence spectrum are therefore due to emission on single rotational lines. The assignment of the different vibrational levels in the electronic ground state is indicated in Fig. 3.5. The dispersed fluorescence spectrum displayed in the figure is already corrected for the wavelength dependent sensitivity of the detection system (indicated by the dashed line in the figure).

The height of the different peaks directly provides the relative branching ratios for the different vibrational transitions, being proportional to the Einstein $A_{0,v''}$ coefficient. The dispersed fluorescence spectrum directly relates all $a(v'=0)\rightarrow X(v'')$ transitions to the 0-0 transition measured in direct absorption. The resulting Einstein coefficients, with their absolute scale determined by the absorption measurements of the 0-0 transition (*vide infra*), are listed in Table 3.1, together with the Franck-Condon factors. The measured Einstein coefficients agree rather well with the ones calculated by James [2]. The original values of James differ by a factor 2 from the ones listed here because James considered both

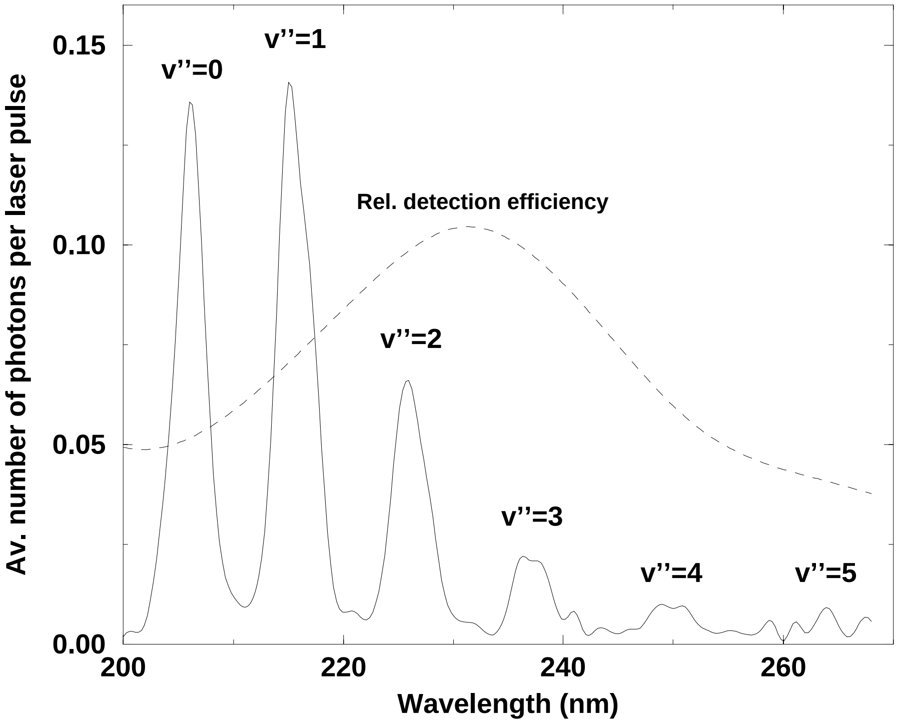

Figure 3.5: *Dispersed fluorescence spectrum of the spin-forbidden a→X transition in CO. The vertical axis shows the averaged number of photons per laser pulse. The relative wavelength dependent detection efficiency of the entire detection system, indicated with the dashed curve in the figure, is calibrated using the known branching ratios of the NO(A→X) transition, which lies in the same wavelength region. The CO dispersed fluorescence spectrum displayed in the figure is already corrected for this curve.*

Λ-doublet components separately. The agreement between calculated and experimentally determined values for the Einstein coefficients once more validates the model as proposed by James.

The Einstein A coefficient for the 0-0 transition ($A_{0,0}$) is obtained from direct absorption measurements. Figure 3.6 shows the results of the absorption measurements on the $Q_2(2)$ transition. The transmitted light through the absorption cell is measured for pressures of 0, 5, and 10 Torr of CO. Each data point shows the transmitted light intensity, i.e. the intensity of the fluorescence signal in the molecular beam, for the indicated pressure, averaged over 60 laser shots. The vertical axis is adjusted to correspond to zero absorption at 0 Torr.

From these data the peak cross-section for absorption at the $Q_2(2)$ transition is obtained. The measured data points are fitted to Beer's law:

$$I = I_0 e^{-\sigma(\nu_p)n(N'')l} \tag{3.1}$$

where I is the intensity of the transmitted light, I_0 the intensity of the incoming light pulse,

Table 3.1: *Einstein coefficients and Franck-Condon factors derived from the dispersed fluorescence spectrum (Fig. 3.5), compared to the Einstein coefficients as obtained from the calculations by James [2].*

$v' \rightarrow v''$	$A_{v',v''}(s^{-1})$	F.C. factor	$A^{calc}_{v',v''}(s^{-1})$
0→0	97.2 ±3.2	0.303±0.010	128
0→1	100.7 ±3.5	0.355±0.012	136
0→2	47.22±4.0	0.194±0.016	61
0→3	15.75±3.0	0.074±0.014	16
0→4	7.03±2.5	0.038±0.014	2.5
0→5	6.55±2.5	0.036±0.014	0.22

$\sigma(\nu_p)$ the absorption cross-section on the top of the excitation line at center frequency ν_p, l is the length of the absorption cell and $n(N'')$ is the number density of molecules in the rotational level in the electronic ground state, labelled by the rotational quantum number N''. The relative population of the various rotational levels in the ground state needed for the calculation of $n(N'')$, is obtained from a Boltzmann distribution for room temperature CO.

The peak absorption cross-section for the $Q_2(2)$ line is determined from the fit. The value for the peak cross-section is indicated in Table 3.2 for all three lines of the absorption experiment. The Einstein A coefficient can be related to the peak absorption cross-section

$$\sigma(\nu_p) = \pi r_0 f_{if} g(\nu_p) \qquad (3.2)$$

where

$$g(\nu_p) = \frac{2\sqrt{ln2}}{\sqrt{\pi}\Delta\nu_D} \quad \text{and} \qquad (3.3)$$

$$f_{if} = \frac{g_f}{g_i}\frac{\lambda^2}{8\pi^2 r_0 c}\frac{A_{v',v''}S_{J,N''}}{2N''+1} \qquad (3.4)$$

r_0 is the classical electron radius, $g(\nu_p)$ the value of the normalized Doppler profile with Doppler width $\Delta\nu_D$ (in cm^{-1}) at the peak position of the transition and f_{if} the oscillator strength of the transition. The oscillator strength contains the degeneracy of the final (g_f) and initial (g_i) state (g_f/g_i=2 because of the Λ-doubling in the excited state), the wavelength of the a←X transition λ, the normalized Hönl-London factor $\frac{S_{J,N''}}{2N''+1}$ and the Einstein A coefficient for the given vibrational transition. The calculated Hönl-London factors [2, 12] as well as the resulting Einstein coefficient for the transitions probed in the experiment are also found in Table 3.2. From these data an averaged Einstein coefficient of $A_{0,0}$=97.2±3.2 s^{-1} is derived for the a$(v'=0)$ ←X$(v''=0)$ transition.

Combining the results of the dispersion and the absorption measurements, the lifetime $\tau(J)$ of a certain rotational level with quantum number J of the $a^3\Pi$ state is calculated

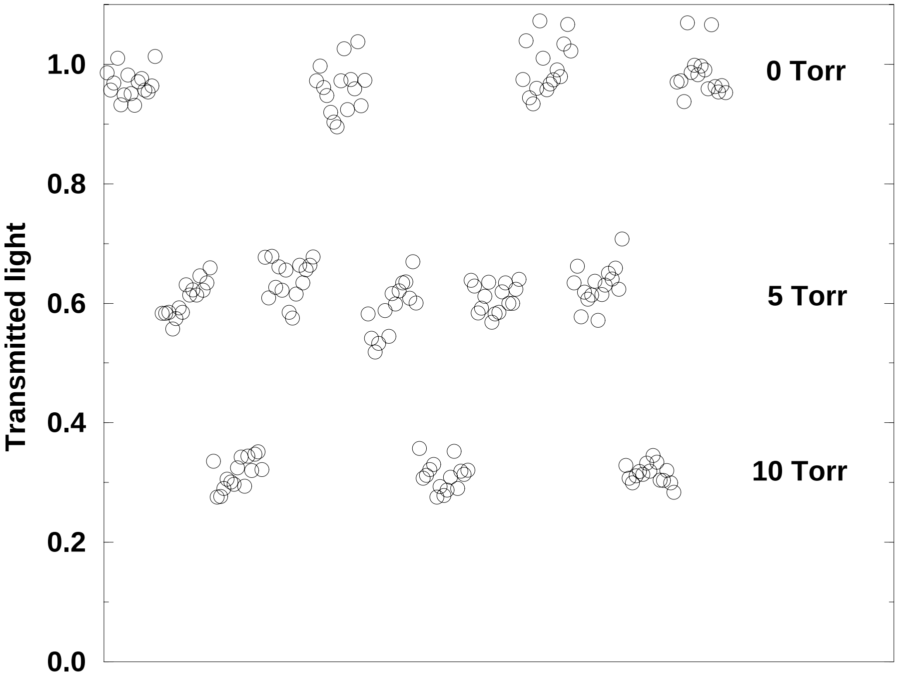

Figure 3.6: *Transmission on the $Q_2(2)$ line for three different pressures of CO in the absorption cell. The first 15 data points are recorded with an evacuated cell. For the next 15 data points the cell is filled with 5 Torr of CO, after that with 10 Torr of CO, etc. The vertical axis is adjusted to a transmittance of unity for an evacuated cell.*

via [2]:

$$\tau(J) = \left[c_{i,1}^2(J)\Sigma_{v''}A_{0,v''}\right]^{-1} \tag{3.5}$$

$c_{i,1}^2(J)$ describes the amount of Ω=1 character for the specific level labelled by J and Ω'=i [14]. Since $c_{i,1}^2(J)$ strongly depends on J and i, the lifetime of the excited state depends strongly on these parameters as well. Using this expression, the lifetime of the J=1 level in the Ω=1 ladder is determined to be $\tau(J{=}1){=}3.6_7{\pm}0.4$ ms. The lifetime τ_{abs} of the upper levels of the different transitions used in the absorption experiment, calculated via this model, is indicated in Table 3.2.

The combination of dispersion and direct absorption measurements provide a general tool to measure lifetimes even of very weak transitions; it is generally applicable to obtain peak cross-sections of molecules with a well separated spectrum even for a broad-band light source.

The value of the Einstein A coefficient of the a$(v' = 0) \rightarrow$X$(v'' = 0)$ transition in CO as obtained from the direct absorption measurements differs from the value that we have obtained previously from cavity ring down (CRD) absorption experiments [15] by a factor of 2.5. The explanation for this might be found in the fact that the CRD measurements are performed for the bandhead of the Q_3-branch, which is much weaker than the transitions to the Ω=1 ladder. A (weak) additional coupling of the a$^3\Pi$ state to states other than

Table 3.2: *For each of the excitation lines used in the experiment the rotational quantum number of the upper state J, the peak absorption cross-section $\sigma(\nu_p)$, the Hönl-London factor, the Einstein coefficient $A_{0,0}$ obtained from the peak absorption cross-section, the lifetime as determined from absorption and dispersion measurements τ_{abs}, and the lifetime determined from the two-point measurements τ_{2p} are given.*

Exc. line	J	$\sigma(\nu_p)(10^{-19}\mathrm{cm}^2)$	2×H.L.	$A_{0,0}(\mathrm{s}^{-1})$	τ_{abs} (ms)	τ_{2p} (ms)
$R_2(0)$	1		1.988		$3.6_7\pm0.4$	1.07 ± 0.15
$R_2(1)$	2	4.16	0.964	92 ± 14	$3.7_8\pm0.4$	1.20 ± 0.20
$Q_2(1)$	1	4.78	0.993	102.6 ± 11	$3.6_7\pm0.4$	1.10 ± 0.20
$Q_2(2)$	2	4.39	0.962	97.1 ± 3.5	$3.7_9\pm0.4$	

the $A^1\Pi$ state will, therefore, have a relatively large influence on the oscillator strength of transitions to levels in the Ω=2 ladder.

The averaged lifetime of the $a^3\Pi$ state that follows from our absorption and dispersion measurements, τ_{av}=11.0±0.4 ms (corresponding to an oscillator strength of $(1.26\pm0.04) \cdot 10^{-7}$), can directly be compared to a number of values reported in literature before [3, 4, 7, 8]. It should be remembered that the value determined in the present experiment is derived for single, low lying, rotational levels in the $a^3\Pi_1(v' = 0)$ state, and is only afterward averaged over many rotational levels.

3.3.2 Two-point lifetime measurements

An alternative way to determine the lifetime for long lived species is to detect the fluorescence signal at two different positions, separated by a distance s, as schematically shown in Fig. 3.4. The ratio of the fluorescence intensity recorded with PMT's at either position can be measured as a function of the time-delay Δt by varying the velocity v of the metastable species in the beam. The ratio of the two integrated PMT-signals $\frac{I_2}{I_1}$ is related to the lifetime τ of the laser prepared rotational level in the $a^3\Pi$ state via:

$$\frac{I_2}{I_1} \propto e^{-\Delta t/\tau} \tag{3.6}$$

By changing Δt, i.e. the carrier gas, the exponentially decaying fluorescence curve can be probed. The method relies on the fact that only the ratio of the two signals is needed to extract the lifetime.

This might not be obvious on first sight. First of all both PMT's see a different solid angle and have a different detection efficiency for photons. This effect is, however, constant for all the measurements and is just a pre-factor which is independent of the carrier gas. Secondly, upon changing the carrier gas, the velocity of the beam is changed and thereby the residence time in the detection areas 1 and 2 (Fig. 3.4) is changed. The longer the molecules spend in the detection area (i.e. the slower they move) the more photons will be emitted in that time period, leading to an increase in fluorescence signal. Under the assumption that the time that the molecules spend in the detection area is much smaller than the radiative lifetime, this effect is proportional to $\frac{1}{v}$ for both PMT's and cancels out if the ratio of both signals is considered.

Care has to be taken of the mass-focusing effect, however, which causes a distribution of the CO molecules perpendicular to the molecular beam axis that depends on the mass of the carrier gas [16]. Based on earlier measurements for different CO mixtures [10] this effect is on the order of 1% for the given experimental setup and is corrected for in the results discussed here.

Finally, alignment and polarization effects could influence the determination of the radiative lifetime. The spatial orientation of the laser polarization vector causes the molecules to radiate with a certain spatial anisotropy. It is assumed that the spatial fluorescence profile does not change when the carrier gas, and thereby the velocity of the metastable CO molecules, is changed. This is explicitly verified for the laser polarization vector both parallel and perpendicular to the molecular beam axis by measuring the ratio of the fluorescence intensity emitted in vertical and horizontal direction as a function of the velocity of the metastable CO molecules.

Experimental

For the two-point lifetime measurements the (non-dispersed) fluorescence of the laser prepared metastable CO molecules is detected at a distance of 22 cm and 122 cm downstream from the excitation region by two different PMT's, as schematically indicated by detection area 1 and 2 in Fig. 3.4. Both PMT's are looking perpendicularly at the molecular beam in horizontal direction (i.e. in the plane of the molecular beam and the excitation laser beam). The photocathode of the first and the second PMT is mounted 35 cm and 18 cm away from the molecular beam axis, respectively. The fluorescence signal of both PMT's is simultaneously measured, summed over typically 3000 to 6000 laser shots to get good photon statistics, and read out by a PC. The integrated intensities of the fluorescence signals are afterward divided to obtain the desired ratio. The two-point measurements have been performed for 5% CO seeded in He, Ne, Ar, Kr, and Xe using excitation on the $R_2(0)$, $R_2(1)$, and $Q_2(1)$ line.

Normally the entire molecular beam-, laser- and detection-system is operated at a 10 Hz repetition rate. To reduce the pressure in the chamber during these experiments as much as possible, the pulsed valve (and for this reason also the detection system) is running on 10/3 Hz. This guarantees that the pressure in the chamber is below 10^{-6} Torr prior to each gas pulse during operation.

Results and discussion

Figure 3.7 shows the data points (circles with error bars) that are obtained for the different carrier gasses. Laser excitation on the $R_2(0)$ transition (populating the – parity level of the J=1 Λ-doublet in the $a^3\Pi_1$ state) is used to obtain these data points. The horizontal axis shows the time delay between the two PMT signals for each of the carrier gasses.

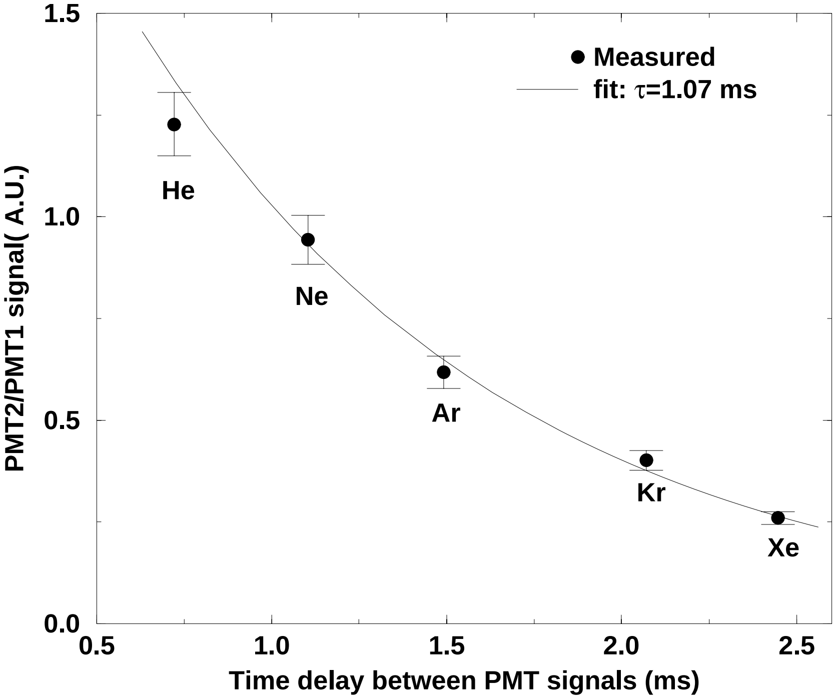

Figure 3.7: *The radiative lifetime of the J=1 – parity level in the* $a^3\Pi_1$ *state (populated via excitation on the* $R_2(0)$ *transition) is recorded with the two-point measurement technique. The horizontal axis shows the time delay between the two PMT-signals (detection area 1 and 2 Fig. 3.4). The vertical axis shows the ratio of the integrated fluorescence signal in area 2 and area 1. The smooth curve shows the best fitting exponential decay, corresponding to a radiative lifetime of 1.07 ms.*

The smooth curve is the exponential fit, and corresponds to a lifetime of 1.07±0.15 ms. The last column of Table 3.2 shows the lifetime τ_{2p} of the upper level as obtained in the two-point lifetime measurements for the different excitation lines. An averaged value of 1.08±0.15 ms is obtained for the J=1 level when the results of excitation on the $R_2(0)$ and $Q_2(1)$ transition are combined.

The lifetime resulting from the two-point measurements differs approximately by a factor 3 from the combined results of the absorption and dispersion measurements. The two-point lifetime measurement is a very direct way to measure the lifetime and is generally applicable for species that have radiative lifetimes between 100 μs and a few ms. A disadvantage is that one can not discriminate against other non-radiative loss channels. An important loss channel in the molecular beam might be collisional redistribution. Normally collisions under these kind of circumstances are negligible, since processes that are monitored are typically on the (sub)nanosecond or microsecond time scale. In the experiment reported here the molecules fly freely during up to 2.5 ms. It might be that collisional redistribution of metastable CO molecules in the molecular beam can no longer be neglected over such a long flight time. The relative velocity between molecules in the beam is very

low, which might lead to large collisional redistribution rates.
Because the lifetime of the lowest rotational levels in the Ω=1 ladder are the shortest, any collisional redistribution to other levels in the $a^3\Pi_1$ state or to the electronic ground state is an extra loss channel for fluorescence and leads to an underestimation of the lifetime. Results of experiments in a cell show that CO in the $a^3\Pi_1(J{=}1)$ level that collides with ground state CO molecules redistributes over other rotational levels, mainly within the Ω=1 manifold. All these levels have approximately the same radiative lifetime. A factor of three difference in lifetime as observed between the different techniques is therefore most probably explained by collisional relaxation of the metastable CO molecules to the electronic ground state.

3.4 Ionization based detection schemes

The above-mentioned detection schemes are rather straight forward, bot not most sensitive. The detection efficiency can be increased by orders of magnitude when a second laser is applied to efficiently ionize the metastable CO molecules (the I.P. is indicated in Fig. 3.1 at 113,027.5 $\text{cm}^{-1}\hat{=}14.0$ eV [17]); subsequently these ions can be detected on a MCP detector.

The easiest way to discriminate metastable CO from ground state CO molecules is by using photons with enough energy to directly ionize the metastable CO molecules, but with insufficient energy to ionize ground state CO. If CO molecules are prepared in the $a^3\Pi(v{=}1)$ state, a photon from an F_2-excimer laser (157 nm) will have just enough energy (only 0.1 eV of excess energy) to reach the I.P. and thus ionize metastable CO. The one-photon ionization of the metastable state is indicated by the dashed arrow in Fig. 3.1 and together with the preparation photon form effectively a (1+1′)-REMPI scheme for detection of ground state CO molecules. This detection scheme is investigated by us and found to be very effective, but no further details will be given here. One-photon laser ionization is much more sensitive than the methods described above and, although it is not quantum-state selective for ro-vibrational levels of the $a^3\Pi$ state, it might even be an advantage if this selectivity is not needed.

The last detection method indicated in Fig. 3.1 combines a high detection sensitivity with quantum state selectivity. A resonant transition to an intermediate electronic state is induced before ionization occurs. An example of (1+1)-REMPI detection of CO molecules that are laser prepared in the $a^3\Pi(v{=}0)$ state (using 206 nm laser radiation) is indicated in Fig. 3.1 by the solid arrows. For the $b(v{=}0)\leftarrow a(v{=}0)$ transition a 283 nm laser photon is needed. Absorption of a photon of the same laser leads to ionization, with an excess energy of almost 0.8 eV. Metastable CO molecules in the $a^3\Pi(v{=}1)$ state can be detected in a similar way by a (1+1)-REMPI process via the $b^3\Sigma^+(v{=}0)$ or $(v{=}1)$ state, using laser radiation around 296 nm or 279 nm, respectively. We will focus here, however, on the first process.

Extensive spectroscopic studies have been performed on the intermediate $b^3\Sigma^+$ state [15,18–23]. All vibrational levels in this electronic state are perturbed by high vibrational levels ($v' \geq 31$) of the $a'^3\Sigma^+$ state. The studies on the $b^3\Sigma^+$ state have yielded calculated and experimentally determined Franck-Condon factors for the b←a transition [15, 19]. The strongest transition from the $a^3\Pi(v{=}0)/(v{=}1)$ state is to the $v{=}1/v{=}0$ level in the $b^3\Sigma^+$ state. The b←a transition is spin-allowed, and therefore this transition is readily saturated with currently available pulsed lasers, even for transitions with unfavourable Franck-Condon factors. Of course detection of the b→a LIF signal can also serve to detect the metastable CO molecules, but is not as sensitive as REMPI detection.

Other electronic triplet states can be chosen for (1+1)-REMPI detection of metastable CO molecules, as long as the one-photon energy is above 4 eV. Examples of states that we have also used are (high vibrational levels of) the $a'^3\Sigma^+$ state [15, 20, 21], the $c^3\Pi$ and the $k^3\Pi$ state [24–27].

3.4.1 Experimental

The REMPI experiments are performed in the setup that has also been used for the calibration of the detection efficiency of a MCP detector for metastable CO molecules. Both preparation and ionization laser are no longer focused. The power of the ionization laser is still large enough, however, to saturate the b←a transition. The extraction of the laser produced ions is accomplished with a high voltage pulser of variable delay relative to the ionization laser pulse. Thus, the ionization can be achieved in zero electric field or in an electric field of controlled field strength.

3.4.2 Results and discussion

Figure 3.8 shows REMPI spectra of the b←a transition for different situations. The 206 nm preparation laser is kept fixed in frequency, while the ionization laser is scanned over the b←a transition. The upper two traces show spectra that are recorded in zero electric field (the extraction field is switched on after ionization). For preparation of the – parity component of the $J{=}1$ level (upper trace: $R_2(0)$ excitation), only transitions to $N{=}0$ and $N{=}2$ level of the $b^3\Sigma^+(v{=}0)$ state are allowed due to the parity-change selection rule. Preparation of the + parity component of the $J{=}1$ level (middle trace: $Q_2(1)$ excitation) only yields the $N{=}1$ and $N{=}3$ peak in the REMPI spectrum. All peaks become rather broad due to saturation of the b←a transition.

The advantage of using a $^3\Sigma^+$ state as intermediate is that the spectrum is less complicated than for a $^3\Pi$ or $^3\Delta$ state, and that the two different Λ-doublet components of rotational levels in the $a^3\Pi_1$ state (for the $\Omega{=}1$, $J{=}1$ level only 394 MHz apart [28]) can easily be distinguished. This is because the parity of the rotational level in the $b^3\Sigma^+$ state is given by $(-1)^N$ and transitions originating from –/+ parity components in the $a^3\Pi$ state must go to even/odd N values in the $b^3\Sigma^+$ state as a result of the parity-change selection rule. The transitions belonging to the different parity components are therefore separated over at least two times the rotational constant in the $^3\Sigma^+$ state, which is readily resolved with normal pulsed dye lasers.

If the $R_2(0)$ transition is excited in an electric field of 400 V/cm (with proper selection of the angle between polarization vector of the laser and the electric field), the parity selection rule is broken due to the mixed character of the wavefunction. This effect is observed in

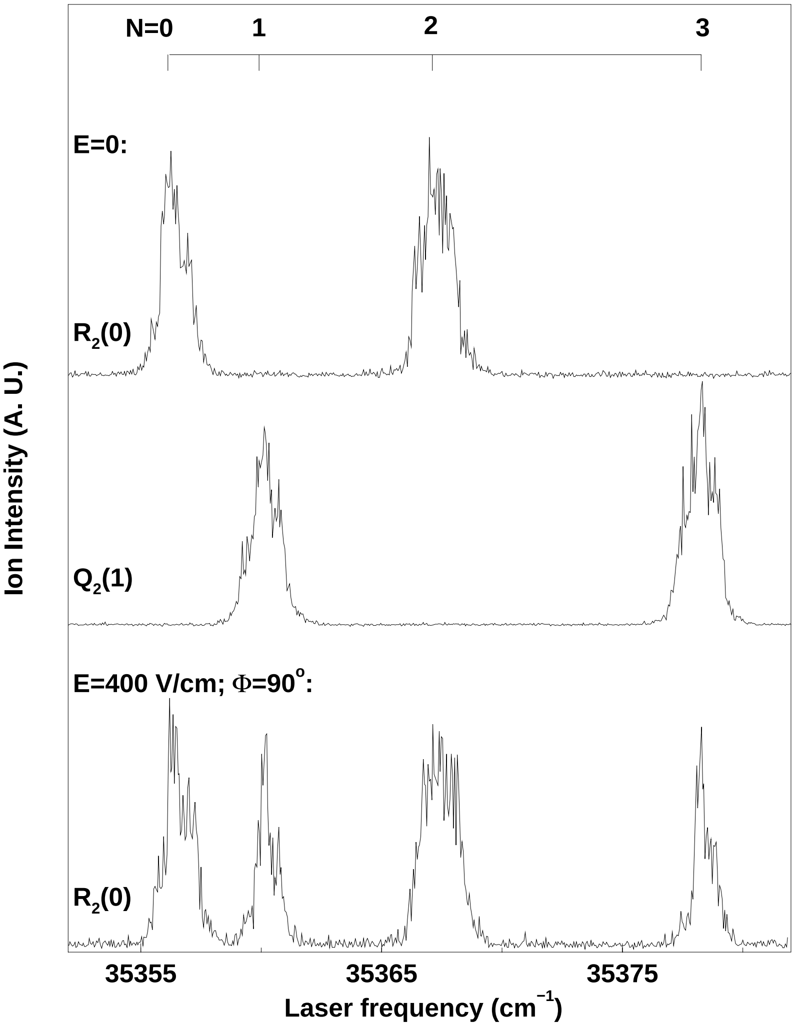

Figure 3.8: *Upper trace: REMPI spectrum of metastable CO molecules that are laser prepared via the $R_2(0)$ transition, followed by ionization via the $b^3\Sigma^+(v=0)$ state. The spectrum is recorded in zero electric field. Labeling of the peaks according to rotational levels in the $b^3\Sigma^+$ state is indicated at the top of the figure. Middle trace: similar spectrum as displayed in the upper trace, but now excitation is performed on the $Q_2(1)$ transition. Lower trace: similar spectrum as displayed in the upper trace, but now the excitation and ionization is performed in an electric field of 400 V/cm that is directed perpendicular to the direction of laser polarization (ϕ=90°).*

the lower trace of Fig. 3.8. The 'parity-forbidden' transitions to N=1 and N=3 levels are clearly visible, almost equally strong as the 'parity-allowed' transitions. Although in these electric fields the mixing of the wavefunction is far from complete (see chapter 4), saturation of the 'parity-forbidden' transitions is easily accomplished and excitation on these transitions yields as much signal as excitation on the 'parity-allowed' transitions on top of the line. However, the saturation broadening for these transitions is observed to be smaller than for the ‘parity-allowed’ transition. The mixing of the $a^3\Pi$ wavefunction in the electric field can therefore be probed very sensitively by using a $^3\Sigma^+$ state as intermediate state for ionization, in a similar way as has been demonstrated for NO [29].

3.5 Conclusions

Several detection schemes applicable to metastable CO molecules are discussed. The described schemes include detection of Auger electrons, fluorescence photons or laser produced ions. Recording the decrease in signal registered by a MCP detector (used for detection of metastable CO molecules via Auger deexcitation) when part of the metastable CO molecules is ionized by a laser enables the detection efficiency of the MCP detector to be determined as $(6.5\pm2)\cdot10^{-4}$.

Detection of the a→X fluorescence allowed the determination of the radiative lifetime for the lowest rotational levels in the Ω=1 component of the $a^3\Pi$ state via two different techniques. From the dispersion and direct absorption experiments a lifetime of $3.6_7\pm0.4$ ms for the J=1 level in the $a^3\Pi_1$ state was determined. The two-point lifetime measurement technique gives a lifetime of 1.08±0.15 ms for this same level. The difference might be explained by collisional redistribution inside the molecular beam.

The (1+1)-REMPI scheme via the $b^3\Sigma^+$ state is shown to be very sensitive and has the advantage of readily distinguishing the different Λ-doublet components in the $a^3\Pi$ state, although they are energetically only a few hundred MHz apart. In addition, the mixing of the wavefunction in electric fields can be probed efficiently.

References

[1] H. Hotop in *Experimental Methods in the Physical Sciences*, Vol. 29 B: Atomic, Molecular and Optical Physics, Chapter 11, 191-215, eds. F.B. Dunning and R.G. Hulet (Academic Press Inc., San Diego, 1996).

[2] T.C. James, J. Chem. Phys. **55**, 4118 (1971).

[3] V. Hasson and R.W. Nicholls, J. Phys. B **4**, 681 (1971).

[4] A.R. Fairbairn, J. Quant. Spectrosc. Radiat. Transfer **10**, 1321 (1970).

[5] T.G. Slanger and G. Black, J. Chem. Phys. **55**, 2164 (1971).

[6] W.L. Borst and E.C. Zipf, Phys. Rev. A **3**, 979 (1971).

[7] G.M. Lawrence, Chem. Phys. Lett. **9**, 575 (1971).

[8] T.C. James, J. Mol. Spectrosc. **40**, 545 (1971).

[9] H.D. Hagstrum, Phys. Rev. **96**, 336 (1954).

[10] Chapter 2 of this thesis and
R.T. Jongma, Th. Rasing, and G. Meijer, J. Chem. Phys. **102**, 1925 (1995).

[11] M.G.H. Boogaarts, Ph.D. thesis, University of Nijmegen (1996).

[12] R.W. Field, S.G. Tilford, R.A. Howard, and J.D. Simmons, J. Mol. Spectrosc. **44**, 347 (1972).

[13] L.G. Piper and M. Cowles, J. Chem. Phys. **85**, 2419 (1986).

[14] The values $c_{\Omega',i}$ (as given in the Appendix) are calculated using the model of Field et al. [12] to determine the energy of rotational levels in the $a^3\Pi$ state. In this model all the Ω-ladders are interacting with each other. From the wavefunction belonging to the specific quantum state labelled by J and Ω', the amount of Ω=i-character is calculated by squaring $c_{\Omega',\mathrm{i}}(J)$.

[15] R.T. Jongma, M.G.H. Boogaarts, and G. Meijer, J. Mol. Spectrosc. **165**, 303 (1994).

[16] *Atomic and Molecular Beam Methods*, Vol. I and II, ed. G. Scoles (Oxford University Press, New York, 1988/1992).

[17] A. Mellinger, C.R. Vidal, and Ch. Jungen, J. Chem. Phys. **104**, 8913 (1996).

[18] G.H. Dieke and J.W. Mauchly, Phys. Rev. **43**, 12 (1933).

[19] C.V.V. Prasad, G.L. Bhale, and S.P. Reddy, J. Mol. Spectrosc. **121**, 261 (1987).

[20] T. Rytel, J. Mol. Spectrosc. **145**, 420 (1991).

[21] T. Rytel, J. Mol. Spectrosc. **173**, 370 (1995).

[22] T. Rytel, J. Mol. Spectrosc. **151**, 271 (1992).

[23] T. Rytel, J. Mol. Spectrosc. **161**, 369 (1993).

[24] I. Dabrowski, M. Vervloet, and D.-C. Wang, Can. J. Phys. **65**, 1171 (1987).

[25] J. Baker and F. Launay, J. Mol. Spectrosc. **165**, 75 (1994).

[26] J. Baker, J. Mol. Spectrosc. **167**, 323 (1994).

[27] G. Berden, D. van der Zande, R.T. Jongma, and G. Meijer, in preparation.

[28] R.C. Stern, R.H. Gammon, M.E. Lesk, R.S. Freund, and W.A. Klemperer, J. Chem. Phys. **52**, 3467 (1970).

[29] J.J. v. Leuken, Ph.D. thesis, Vrije Universiteit Amsterdam (1994).

Appendix

Table 3.3: *Wavefunction of the lower Λ-doublet components: Proportionality constants of Ω=0, 1 and 2 part of the wavefunction of rotational levels in the F_1, F_2 and F_3 component of the lower Λ-doublet components (accessible via P or R transitions from the electronic ground state) of the a$^3\Pi$(v=0) state. The amount of Ω=0, 1 or 2 character in the wavefunction is obtained by squaring the constants given in the table.*

	F_1			F_2			F_3		
J	$c_{0,0}$	$c_{0,1}$	$c_{0,2}$	$c_{1,0}$	$c_{1,1}$	$c_{1,2}$	$c_{2,0}$	$c_{2,1}$	$c_{2,2}$
0	1.0000	0.0000	0.0000						
1	0.9969	-0.0788	0.0000	-0.0788	-0.9969	0.0000			
2	0.9908	-0.1349	0.0082	-0.1347	-0.9817	0.1349	0.0101	0.1348	0.9908
3	0.9821	-0.1875	0.0179	-0.1871	-0.9601	0.2076	0.0217	0.2073	0.9780
4	0.9711	-0.2368	0.0300	-0.2360	-0.9337	0.2693	0.0357	0.2686	0.9626
5	0.9582	-0.2825	0.0440	-0.2813	-0.9036	0.3230	0.0515	0.3219	0.9454
6	0.9440	-0.3245	0.0593	-0.3227	-0.8713	0.3698	0.0683	0.3683	0.9272
7	0.9289	-0.3626	0.0755	-0.3603	-0.8377	0.4104	0.0856	0.4085	0.9088
8	0.9132	-0.3969	0.0921	-0.3942	-0.8038	0.4455	0.1028	0.4432	0.8905
9	0.8974	-0.4276	0.1088	-0.4246	-0.7702	0.4759	0.1197	0.4732	0.8728
10	0.8817	-0.4549	0.1252	-0.4518	-0.7375	0.5020	0.1360	0.4991	0.8558
11	0.8663	-0.4792	0.1411	-0.4759	-0.7060	0.5245	0.1517	0.5215	0.8396
12	0.8514	-0.5007	0.1565	-0.4974	-0.6758	0.5439	0.1666	0.5410	0.8244
13	0.8370	-0.5197	0.1712	-0.5165	-0.6471	0.5608	0.1806	0.5578	0.8101
14	0.8233	-0.5366	0.1852	-0.5335	-0.6200	0.5754	0.1939	0.5725	0.7967
15	0.8102	-0.5515	0.1984	-0.5485	-0.5944	0.5880	0.2064	0.5853	0.7841
16	0.7979	-0.5647	0.2109	-0.5620	-0.5703	0.5991	0.2181	0.5965	0.7724
17	0.7862	-0.5765	0.2226	-0.5739	-0.5476	0.6088	0.2291	0.6064	0.7614
18	0.7752	-0.5870	0.2336	-0.5846	-0.5264	0.6174	0.2394	0.6151	0.7512
19	0.7648	-0.5963	0.2440	-0.5942	-0.5064	0.6249	0.2491	0.6229	0.7416
20	0.7550	-0.6047	0.2537	-0.6028	-0.4876	0.6316	0.2582	0.6297	0.7326
21	0.7458	-0.6122	0.2628	-0.6105	-0.4700	0.6375	0.2667	0.6359	0.7242
22	0.7371	-0.6189	0.2714	-0.6174	-0.4535	0.6428	0.2747	0.6414	0.7164
23	0.7289	-0.6250	0.2795	-0.6237	-0.4379	0.6475	0.2823	0.6463	0.7090
24	0.7212	-0.6305	0.2871	-0.6294	-0.4232	0.6517	0.2894	0.6507	0.7020
25	0.7139	-0.6354	0.2942	-0.6346	-0.4094	0.6555	0.2961	0.6547	0.6955

Table 3.4: *Wavefunction of the upper Λ-doublet components: Proportionality constants of Ω=0, 1 and 2 part of the wavefunction of rotational levels in the F_1, F_2 and F_3 component of the upper Λ-doublet components (accessible via Q transitions from the electronic ground state) of the $a^3\Pi(v=0)$ state. The amount of Ω=0, 1 or 2 character in the wavefunction is obtained by squaring the constants given in the table.*

J	F_1			F_2			F_3		
	$c_{0,0}$	$c_{0,1}$	$c_{0,2}$	$c_{1,0}$	$c_{1,1}$	$c_{1,2}$	$c_{2,0}$	$c_{2,1}$	$c_{2,2}$
0	1.0000	0.0000	0.0000						
1	0.9966	-0.0824	0.0000	-0.0824	-0.9966	0.0000			
2	0.9900	-0.1408	0.0088	-0.1407	-0.9808	0.1349	0.0104	0.1348	0.9908
3	0.9805	-0.1954	0.0191	-0.1951	-0.9585	0.2077	0.0223	0.2074	0.9780
4	0.9687	-0.2463	0.0319	-0.2457	-0.9311	0.2695	0.0367	0.2689	0.9625
5	0.9549	-0.2932	0.0465	-0.2921	-0.9001	0.3233	0.0529	0.3223	0.9451
6	0.9398	-0.3358	0.0625	-0.3343	-0.8667	0.3702	0.0701	0.3688	0.9269
7	0.9239	-0.3743	0.0793	-0.3724	-0.8322	0.4109	0.0878	0.4091	0.9082
8	0.9076	-0.4086	0.0964	-0.4064	-0.7974	0.4461	0.1054	0.4440	0.8898
9	0.8912	-0.4392	0.1134	-0.4367	-0.7631	0.4764	0.1227	0.4741	0.8719
10	0.8751	-0.4662	0.1301	-0.4635	-0.7298	0.5026	0.1394	0.5001	0.8547
11	0.8593	-0.4900	0.1462	-0.4872	-0.6977	0.5251	0.1553	0.5225	0.8384
12	0.8442	-0.5110	0.1617	-0.5082	-0.6672	0.5446	0.1704	0.5419	0.8230
13	0.8297	-0.5295	0.1764	-0.5267	-0.6382	0.5615	0.1847	0.5588	0.8085
14	0.8160	-0.5459	0.1904	-0.5431	-0.6109	0.5761	0.1981	0.5734	0.7949
15	0.8029	-0.5602	0.2035	-0.5576	-0.5852	0.5888	0.2108	0.5862	0.7822
16	0.7906	-0.5730	0.2159	-0.5704	-0.5611	0.5999	0.2226	0.5974	0.7704
17	0.7790	-0.5842	0.2275	-0.5818	-0.5384	0.6096	0.2337	0.6073	0.7593
18	0.7681	-0.5942	0.2384	-0.5919	-0.5172	0.6182	0.2440	0.6160	0.7490
19	0.7579	-0.6031	0.2486	-0.6010	-0.4973	0.6257	0.2538	0.6236	0.7394
20	0.7483	-0.6111	0.2582	-0.6091	-0.4786	0.6324	0.2629	0.6305	0.7303
21	0.7392	-0.6182	0.2672	-0.6163	-0.4611	0.6383	0.2714	0.6365	0.7219
22	0.7307	-0.6246	0.2756	-0.6229	-0.4447	0.6436	0.2795	0.6420	0.7140
23	0.7227	-0.6303	0.2835	-0.6288	-0.4293	0.6484	0.2870	0.6468	0.7066
24	0.7152	-0.6355	0.2909	-0.6341	-0.4147	0.6526	0.2941	0.6512	0.6996
25	0.7081	-0.6402	0.2979	-0.6389	-0.4011	0.6565	0.3008	0.6552	0.6930

Chapter 4

Confining CO Molecules in Stable Orbits [1]

Abstract

A scheme for confinement of neutral molecules in stable orbits on the basis of the linear Stark effect in a properly designed electrostatic trap is presented. Based on Stark shift measurements in electric fields up to 144 kV/cm, an electrode configuration is described that is, under realistic experimental conditions, capable of confining metastable CO($a^3\Pi$) molecules with velocities up to 22 m/s. Metastable CO molecules can be laser-prepared inside the trap and their trajectories can be directly visualized via spatially resolved detection of their fluorescence.

---

[1] Adapted from: R.T. Jongma, G. von Helden, G. Berden, and G. Meijer, Chem. Phys. Lett. (in press).

4.1 Introduction

Trapping atoms using laser cooling, together with techniques like magnetic trapping and evaporative cooling, has led to numerous exciting results over the last decade, with the realization of Bose-Einstein condensation as the most spectacular achievement [1]. Laser-cooling schemes are applicable to atoms since closed multi-level systems can be realized and many consecutive absorption-emission cycles can be induced. This leads to a momentum transfer from the laser photons to the atom, resulting in a significant change of the velocity of the atom. By now, trapping in one, two or three dimensions has been realized for many different atoms [2, 3].

Trapping of neutral molecules has not been demonstrated yet. The above-mentioned laser-cooling schemes fail for molecules, even though multi-level systems that are electronically and rotationally closed can be found as well. The unavoidable off-resonant fluorescence decay of molecules from the excited state to other vibrational levels in the electronic ground state hampers efficient momentum transfer. As a consequence, only deflection of molecules over small angles using sequential absorption of a limited number of photons is demonstrated [4]. Recently, a complex scheme to overcome this problem has been proposed for laser cooling of Cs_2 (effectively a 21-level system) requiring an exceptional laser system [5].

Other schemes for trapping molecules have been investigated. In the past, magnetic deflection has been realized for several molecules [6, 7], and mechanisms for magnetic [8] and electrostatic trapping [9] have been proposed. It has also been suggested that extremely high laser powers might be used to induce a dipole moment in polarizable molecules, leading to trapping of these molecules in the laser beam [10].

Here we outline a scheme by which neutral, metastable CO molecules can be confined in an appropriately shaped DC electric field on the basis of their linear (first order) Stark effect. The scheme is based on the fact that the electric field between two coaxial electrodes scales with the distance r from the axis as $1/r$. This implies that molecules with a linear Stark effect experience a force that is proportional to $1/r^2$, and can therefore be captured in stable 'planetary' orbits. Metastable CO($a^3\Pi$) molecules are ideal test candidates, as these can be laser-prepared inside the trap and as their trajectories can be directly monitored via spatially resolved detection of their fluorescence.

4.2 A trapping scheme for metastable CO

In an inhomogeneous electric field, neutral molecules experience a force proportional to the gradient of the Stark energy. For molecules in electronic states with a large permanent electric dipole moment such inhomogeneous electric fields can therefore be used to efficiently deflect or focus these molecules. As the force acting on a molecule in a given quantum state depends on its rotational quantum numbers, inhomogeneous electric fields are suitable for state-selection. Often hexapole state-selectors are employed, although a variety of other electrode configurations has been proposed and experimented with [11]. In most cases the focusing performance is based on the first order, i.e. low-field or linear, Stark effect. Recently, it has been demonstrated that polar molecules in extremely high inhomogeneous electric fields, molecules in so-called ‘pendular’ states, can be state-selected as well [12]. In that paper it was suggested that the electrode configuration under study, was also a promising candidate for the trapping of polar molecules. Other papers have elaborated somewhat further on this scheme using an electrode configuration similar to the one proposed here [13, 14].

Rather than working with ‘pendular’ states, we propose confinement in stable orbits of molecules that posses a linear (first order) Stark effect. A promising molecule for such a confinement scheme is the CO molecule. CO in its electronic ground state has only a small dipole moment, and, as it is in a $^1\Sigma^+$ state, does not experience a first order Stark effect. CO in its first electronically excited state, the metastable $a^3\Pi$ state, has a relatively large dipole moment (1.37 D [15]) and does experience a linear Stark effect [15, 16]. Metastable CO ($a^3\Pi$) molecules can therefore be efficiently deflected and focused using inhomogeneous electric fields [17]. CO molecules can be prepared in single quantum-levels of this metastable state via laser excitation on the spin-forbidden $a^3\Pi(v{=}0) \leftarrow X^1\Sigma^+(v{=}0)$ transition around 206 nm [16, 17]. If the laser preparation of metastable CO is performed inside a DC inhomogeneous electric field, the force on the molecule is suddenly switched on at the moment of excitation and acts on the molecule as long as it is in the metastable state. The lifetime of CO ($a^3\Pi$) is strongly quantum-level dependent and ranges from 3–200 ms [18, 19] for levels that can be readily laser prepared.

For the design of an electrostatic trap, it is important to know the exact dependence of the Stark shift on the electric field strength, as this will determine the trajectories of the trapped molecules. Although the Stark shift of the individual quantum-levels in the $a^3\Pi$ state of CO can be calculated using known spectroscopic data, it is *a priori* not clear whether the Stark shift will follow theory in the high electric fields that are necessary for confinement. Neighbouring quantum-levels of perturbing electronic states might interfere in these extremely high fields, thereby complicating the exact field dependence.

4.3 Stark effect in high electric fields

4.3.1 Experimental

To verify the behaviour of the Stark shift as a function of electric field, CO $a^3\Pi(v{=}0) \leftarrow X^1\Sigma^+(v{=}0)$ excitation spectra are recorded as a function of the electric field in which the metastable CO molecules are prepared. The pulsed molecular beam machine and detection techniques used for these experiments have been described in detail in chapter 2 and 3. The radiation used to prepare CO in the metastable state is obtained via frequency-tripling the output of a pulsed dye amplified cw-ring dye laser system. This system produces pulses of 5 ns duration with a high spectral brightness (0.5 mJ/pulse in a 150 MHz bandwidth), by which the spin-forbidden transition in CO can be efficiently induced. Excitation is performed on the $R_2(0)$ and $Q_2(1)$ line to prepare both Λ-doublet components of the $a^3\Pi_1(v{=}0,\ J{=}1)$ level in CO. The laser excites the CO molecules in a homogeneous DC electric field that is applied between two parallel, gold coated electrodes placed 2.06±0.01 mm apart. This set-up allows to obtain high electric fields using relatively low ($\leq$30 kV) voltages. The spectral resolution of the preparation laser system is sufficient to resolve the splittings of the various M-components in the $a^3\Pi_1(v{=}0,\ J{=}1)$ state of CO even in electric fields as low as 1 kV/cm. The angle between the polarization vector of the laser and the electric field is close to the magic angle of 54.7°, such that all M-sublevels in the excited state are equally populated after excitation.

Detection of the metastable CO molecules is performed using (1+1)-Resonance Enhanced Multi-Photon Ionization (REMPI) via the $b^3\Sigma^+(v{=}0)\leftarrow a^3\Pi(v{=}0)$ transition around 283 nm in a field-free region, about 65 cm downstream from the excitation region. The laser light that is needed for this is produced with a Nd:YAG laser pumped pulsed dye laser system (DCR-3/PDL-2, Spectra Physics), running on Fluorescein 548. The output of this laser (40 mJ/pulse in a 0.2 cm^{-1} bandwidth) is frequency doubled in a KDP crystal, providing 10 mJ/pulse of tunable laser radiation around 283 nm. The upper (lower) Λ-doublet component, populated via excitation on the $Q_2(1)$ ($R_2(0)$) transition, can in zero electric field be probed via transitions to the $N{=}1$ or the $N{=}3$ ($N{=}0$ or $N{=}2$) level in the $b^3\Sigma^+(v{=}0)$ level. Subsequently the molecules are ionized via absorption of a second photon from the same laser.

4.3.2 Results and discussion

In zero electric field the splitting between the Λ-doublet levels, the lower with – parity and the upper with + parity, is 394 MHz [15]. Figure 4.1 shows a number of excitation spectra as recorded for the – parity level of the $a^3\Pi_1(v{=}0,\ J{=}1)$ state, populated by excitation on the $R_2(0)$ line of the Cameron band, for different strengths of the electric field. In the electric field each of the Λ-doublet levels is split in a component with $|M\Omega|{=}1$ and a component with $M{=}0$. For the – parity level it is observed that both levels shift to lower energy. The dashed line in the figure shows the calculated first order Stark effect for the $M\Omega{=}1$ level. The component with $M\Omega{=}1$ shifts nearly linearly with the electric field up to field strengths of 50 kV/cm. The deviation for higher electric fields as well as the shift of the $M{=}0$ level can be explained by the second and higher order Stark effect, *vide infra.* To complete the picture for the $J{=}1$ level, similar spectra are recorded for the + parity level of the $a^3\Pi_1(v{=}0)$ state as a function of the electric field strength as well.

The behaviour of the different M-components of the CO ($a^3\Pi_1$, $v{=}0$, $J{=}1$) level in the electric field as deduced from the measured excitation spectra is shown in Fig. 4.2. The energy of the various Stark components is plotted versus the applied electric field. The origin of the vertical axis in Fig. 4.2 is taken at the center of the Λ-doublet in zero electric field. The components originating from the –/+ parity level are indicated in the figure with circles/squares. The $M{=}0$ component does not show a first order Stark effect, and in low electric fields this level is therefore not significantly shifted. In high electric fields the $M{=}0$ components shift over a few tenths of a cm^{-1}. This shift is caused by the second order Stark effect, originating from the coupling of the J=1 level with other rotational levels. Although the second order Stark effect is largest for $M{=}0$, it contributes significantly to the shift of the $|M\Omega|{=}1$ components as well (see Fig. 4.2). The absolute value of the Stark shift is largest for the $M\Omega{=}1$ component (originating from the lower Λ-doublet level), due to the combination of the first and second order Stark effect. A total shift of 1.81 cm^{-1} is observed in an electric field of 144 kV/cm for this level. CO molecules in this quantum

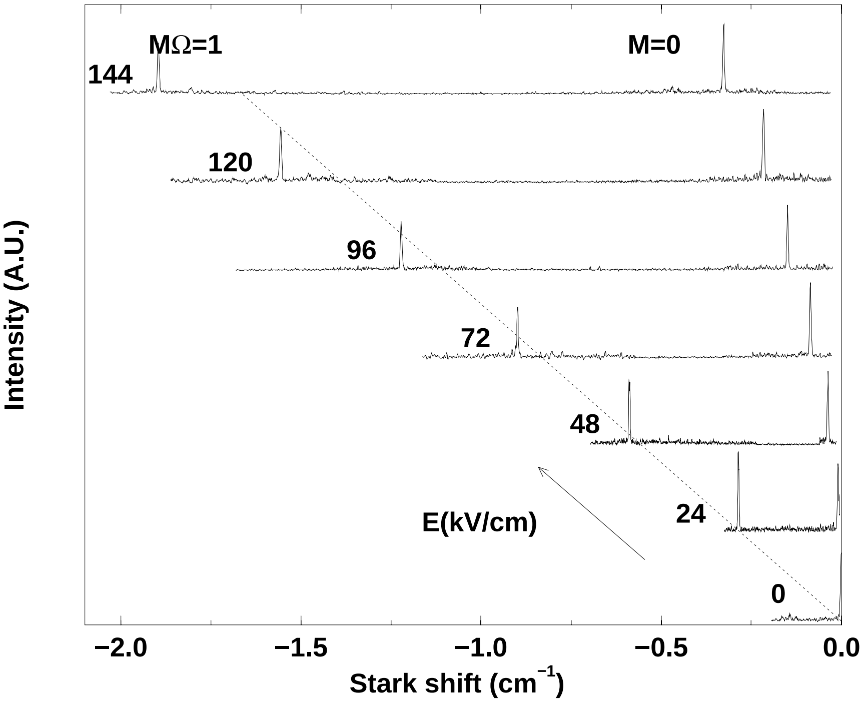

Figure 4.1: *Excitation spectra recorded for the lower Λ-doublet component of the* $a^3\Pi_1(v=0,\ J=1)$ *level for several values of the electric field. The horizontal axis shows the shift of the* $M=0$ *and* $M\Omega=1$ *level relative to the position of these levels in zero electric field. The vertical axis shows the intensity of metastable CO molecules as probed via a (1+1)-REMPI scheme. The dashed line shows the calculated first order Stark effect for the* $M\Omega=1$ *level. The deviation from this line for the* $M\Omega=1$ *component and the shift of the* $M=0$ *level are explained by second and higher order Stark effect.*

level are therefore good candidates for confinement in stable orbits.

4.3.3 Calculation of the Stark energy

The smooth curves indicated in Fig. 4.2 show the calculated Stark shift of the different components, obtained using the known value of the dipole-moment and the rotational energy level structure [20] in the $a^3\Pi$ state. The energy matrix used in the calculations [21, 22] includes coupling to rotational levels up to J=10 for all of the three Ω-ladders. The Hamiltonian for the Stark energy is calculated in a description intermediate between Hund's case (a) and (b). The wavefunction used in this description $|\mathbf{J},\mathbf{M},\mathbf{\Omega},\pm>$ is a superposition of the pure Hund's case (a) wavefunctions,

$$|\mathbf{J},\mathbf{M},\mathbf{\Omega}',\pm> = c_{\Omega',0}|J,M,\Omega=0,\pm> \ + c_{\Omega',1}|J,M,\Omega=1,\pm> \ + \\ c_{\Omega',2}|J,M,\Omega=2,\pm> \qquad (4.1)$$

in which $c_{\Omega',k}$ is the pre-factor for the part of the wavefunction with Ω=k character in the specific Ω′-component [23], as obtained from the energy matrix for a $^3\Pi$ state treated in

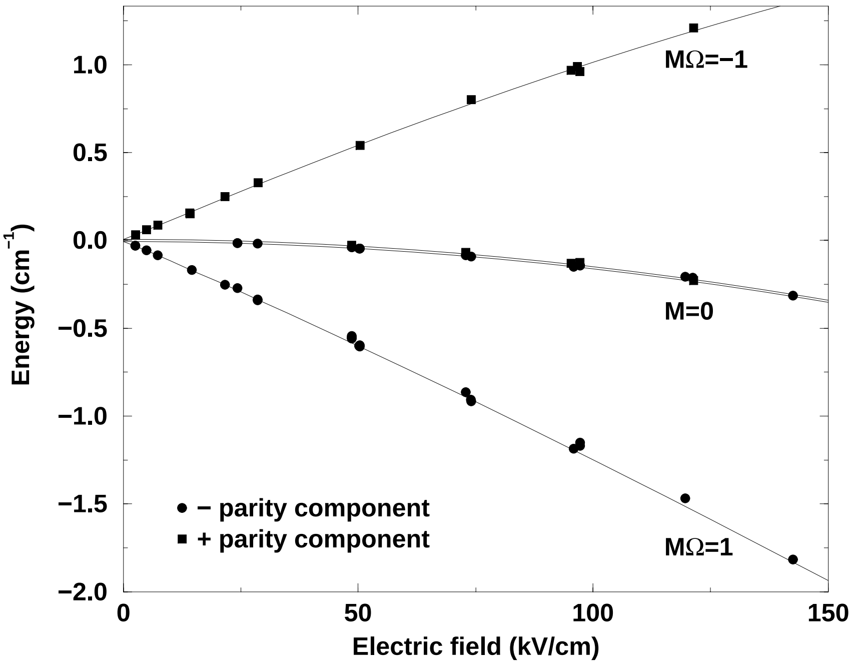

Figure 4.2: *Measured splitting of the different M-components of the CO $a^3\Pi_1(v=0, J=1)$ Λ-doublet as a function of the applied electric field. The vertical axis shows the position of the energy levels relative to the center of the Λ-doublet in zero electric field. The smooth curves indicate the calculated Stark shift.*

a description intermediate between Hund's case (a) and (b) [20]. The (anti-)symmetrical Hund's case (a) wavefunction is given as

$$|J, M, \Omega, \pm >= \sqrt{1/2}\,(|J, M, \Omega > \pm\ |J, M, -\Omega >) \tag{4.2}$$

The only non-zero matrix elements for the Stark energy operator H_{St} are in the pure Hund's case (a) description given by:

$$< J, M, \Omega, \pm|H_{St}|J, M, \Omega, \mp > \;=\; -\frac{|M\Omega|}{J(J+1)}\mu_{el}E \tag{4.3}$$

$$< J, M, \Omega, \pm|H_{St}|J+1, M, \Omega, \pm > \;=\; -\frac{\mu_{el}E}{J+1}\sqrt{\frac{((J+1)^2-\Omega^2)((J+1)^2-M^2)}{(2J+1)(2J+3)}} \tag{4.4}$$

in which μ_{el} is the permanent electric dipole moment and E is the strength of the electric field. Equation (4.3) couples the two Λ-doublet components for a specific J-level in pure Hund's case (a). Because the magnitude of the Λ-doubling is small, this term, which is responsible for the first order Stark effect, has a large influence. Equation (4.4) couples two neigbouring rotational levels, which are much further apart than the two Λ-doublet components, and is responsible for the second and higher order Stark effect. In the description intermediate between Hund's case (a) and (b), all the non-zero matrix elements can be found using the wavefunction as given in Eq. (4.1) and the non-zero matrix elements as given in Eq. (4.3) and (4.4). Diagonalization of the Stark energy matrix provides the eigenvalues (presented for different electric field strengths in Fig. 4.2) and the eigenfunctions as present in an electric field.

The calculation is performed for higher fields than experimentally can be achieved as well. The results of these calculations are indicated for the lowest rotational levels of the F_2 component (mainly $\Omega = 1$ character) in Fig. 4.3. The figure shows the energy of all of the $M\Omega$ components for rotational levels up to J=3. The Λ-doubling is too small to be observed on this scale. It is clear from the figure that levels with equal $|M\Omega|$ but different J are repelling each other. Upon careful inspection, a few discontinuities in the solid lines (indicated with the horizontal arrows) can be seen for several components. These discontinuities are caused by avoided crossings between rotational levels in the Ω=0 component and Ω=1 component. With all energy levels displayed the presence of avoided crossings becomes clear. In this figure the rotational levels of the Ω=0 component, however, are omitted to make the density of states not too high.
So called 'pendular' states, as mentioned above, are achieved for still higher electric fields. To accurately perform the calculations for these high fields, also higher rotational levels should be included in the matrix. The formation of these states is appearing in Fig. 4.3 already; for the lowest rotational states different $M\Omega$ components run almost parallel. Trapping of metastable CO molecules using the 'pendular' states as suggested by Loesch [12], however, is not achievable for metastable CO molecules for realistic values of the electric field.

Equation (4.3) shows that the two Λ-doublet components with equal $|M\Omega|$ (and $|M\Omega| \neq 0$) are strongly coupled. Therefore mixing of the + and – parity character of the wavefunction occurs in electric fields where the magnitude of the Λ-doubling is comparable to the first order Stark energy. This effect is visualized in Fig. 4.4. The fraction of J=1 + (C_+^2) and – parity character (C_-^2) in the wavefunction of the lower Λ-doublet component of the $a^3\Pi_1(v=0,\ J=1,\ |M\Omega|=1)$ level is plotted versus the electric field (in kV/cm). In zero electric field the wavefunction has pure – parity character (C_-^2=1 and C_+^2=0). For low electric fields already (around 1 kV/cm) one can see that the wavefunction consists of a considerable fraction of + parity character as well, while an almost complete mixing of + and – parity character is achieved in electric fields around 5 kV/cm.

The mixed character of the wavefunction has implications for the excitation spectra. In zero electric field the excitation to the metastable state must obey the parity-change selection rule. Therefore the – parity level of the J=1 level can only be populated from a rotational level in the electronic ground state that has + parity character (J''=N''=0, or N''=2). In an electric field, however, the parity character of the $|M\Omega|$=1 levels is mixed and both J=1 components can be populated from the N''=0, 1 and 2 level in the electronic ground state, regardless of the parity. The M=0 level does not show mixing of the wavefunction in low electric fields because the first order Stark effect is zero. This means that in a scan around the $Q_2(1)$ or $R_2(0)$ transition one can populate the $|M\Omega|$=1

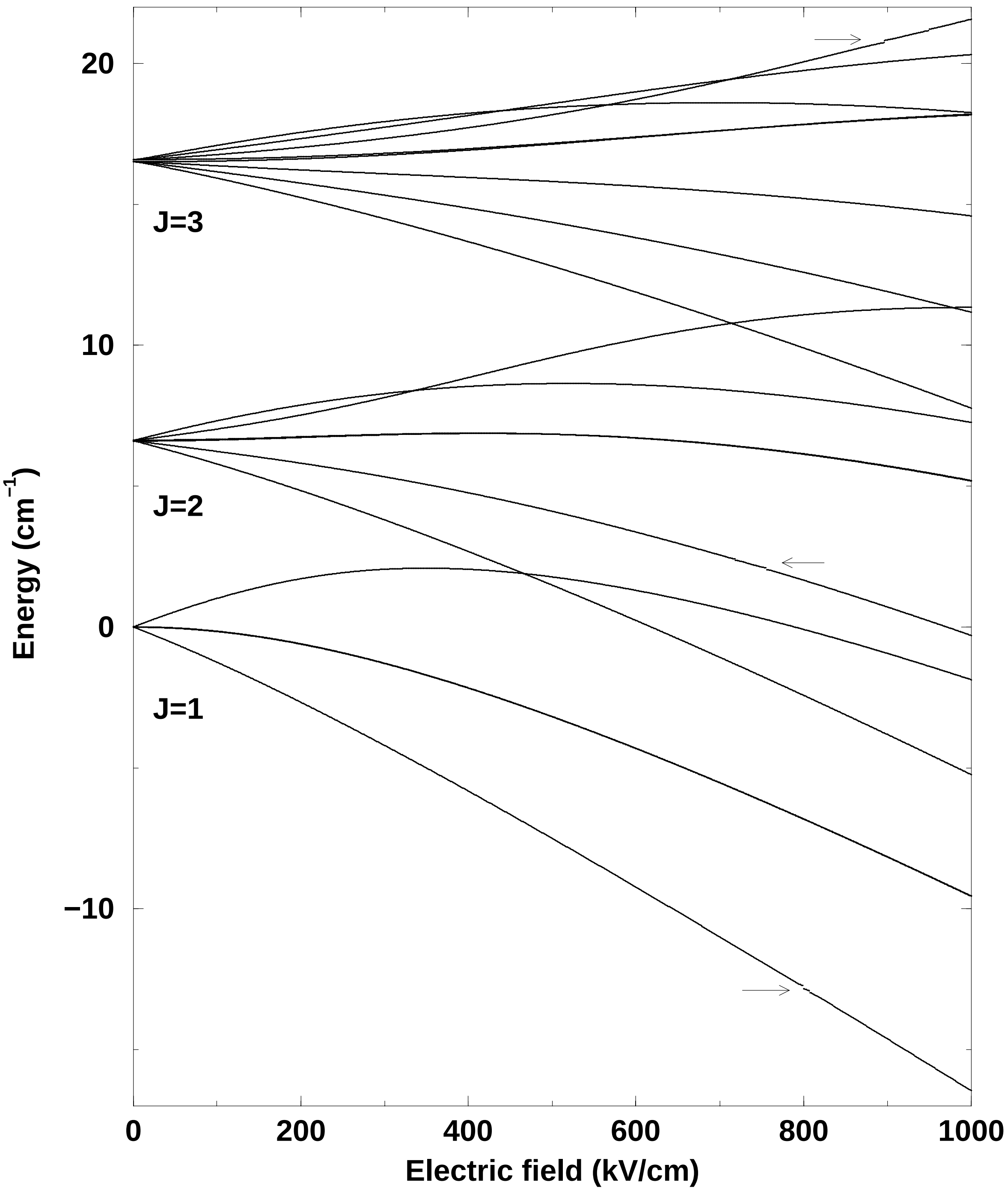

Figure 4.3: *Calculated Stark shift of the M-components for rotational levels up to J=3 of the* $a^3\Pi_1(v{=}0)$ *state in high electric fields. The vertical axis shows the position of the energy levels relative to the origin of the J=1 Λ-doublet of this Ω-ladder in zero electric field. For extremely high electric fields the existence of 'pendular' states is observed. The discontinuities (indicated by the horizontal arrows) are due to avoided crossings with the Ω=0 spin-component.*

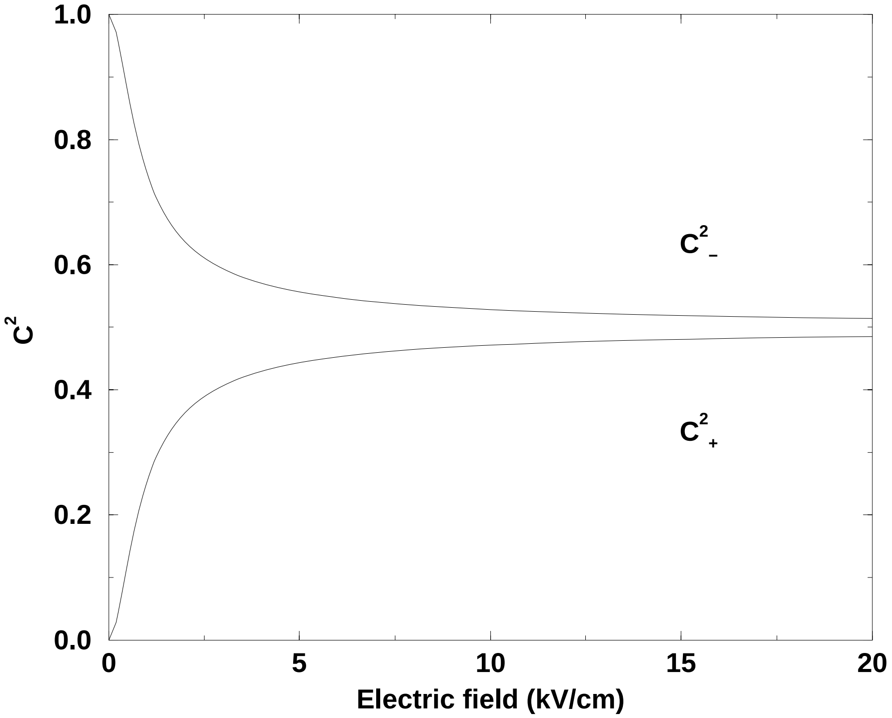

Figure 4.4: *The amount of – parity character (C^2_-) and + parity character (C^2_+) in the wavefunction of the lower Λ-doublet component of the* $a^3\Pi_1$*(v=0, J=1) level is plotted as a function of the electric field (kV/cm). In low electric field the wavefunction has pure – parity character, while for rather low electric fields already, the wavefunction has an almost equal mix of + and – parity character.*

levels originating from both Λ-doublet components and only one of the M=0 components.

The intensity of the metastable CO beam is probed in a (1+1)-REMPI scheme via the $b^3\Sigma^+(v{=}0)$ state. Because the REMPI laser is kept fixed on a transition to N=0 or 1, thereby exclusively probing the – or the + parity component of the J=1 level, and only a minor electric field (below 10 V/cm) is present in the ionization region, the parity selection rules must be obeyed in the resonant b←a transition. Since the metastable CO molecules leave the electric field in the excitation region adiabatically, the different Stark components return to the original + or – parity level of the Λ-doublet and only this component is probed with the REMPI laser, yielding two (instead of three) peaks when the narrow-band excitation laser is scanned. The $|M\Omega|$=1 level of the 'parity forbidden' Λ-doublet component is only probed by changing the frequency of the ionization laser to a resonant transition from this level. This also implies that CO molecules that are state-selected in a hexapole (as described in chapter 2) and in principle posses mixed parity character, will leave the electrostatic hexapole, and will return adiabatically to the Λ-doublet component that was excited by the preparation laser.

4.4 Design of the trap

Knowing the Stark energy as a function of electric field, the force on the molecules can be calculated by taking the gradient of the Stark energy. To aid in the design of a trap, and to be able to calculate and visualize trajectories of neutral molecules in arbitrarily shaped inhomogeneous electric fields, we slightly modified the commercially available programme SIMION [24]. The original programme calculates and visualizes trajectories of charged particles after having determined the force acting on the particles from the gradient of the electrostatic potential, and having solved the equation of motion. The modification to this programme is that, in addition to the calculation of the electrostatic potential, the magnitude of the Stark energy of CO is calculated for each point in which the electrostatic potential is known. Subsequently, the original routine is used, which now calculates the force from the gradient of the Stark energy and shows the resulting trajectories.

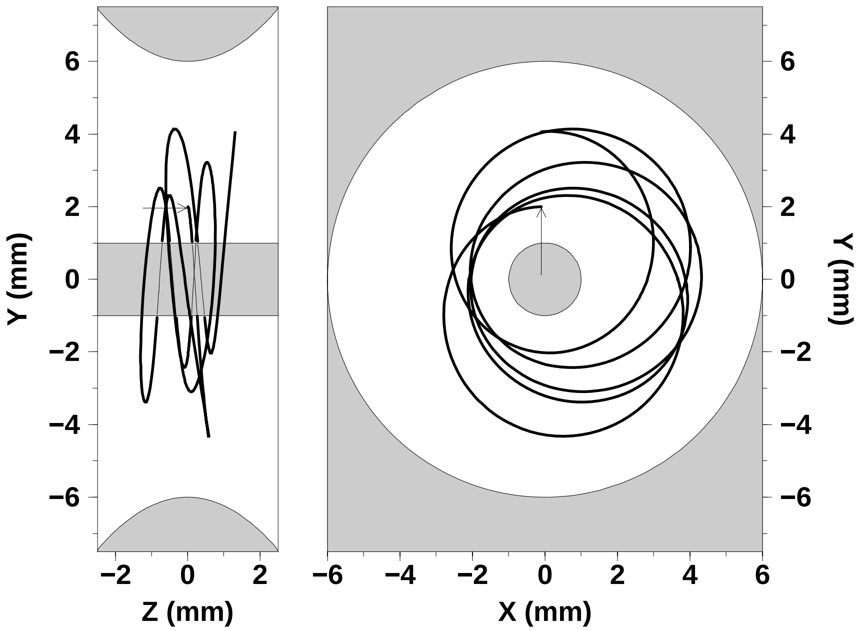

Figure 4.5: *Schematic view of the diabolo-shaped trap, showing a cross-section of the trap in a plane containing the symmetry axis (left) as well as a side view of the trap (right). Calculated trajectories of metastable CO molecules (*$a^3\Pi_1$*, v=0, J=1, MΩ=1) in the trap are indicated by the solid line in both views. The trajectory starts at the laser-excitation region, indicated with an arrow in both figures. The voltage difference applied between inner and outer electrode is 25 kV. The initial velocity of the molecule is 22.1 m/s in the tangential direction and 1.2 m/s in the z-direction.*

A design for a trap based on the Stark effect, is indicated in Fig. 4.5. It is based on the fact that the electric field between two coaxial electrodes scales with the distance r from the axis as $1/r$, implying that molecules with a linear Stark effect, like CO for in moderate electric fields, will experience a force that scales as $1/r^2$. Stable 'planetary' orbits should therefore be possible for molecules with a negative linear Stark effect in such a field geometry. To also obtain confinement in the direction along the symmetry axis, a diabolo-shaped trap is required, as depicted in Fig. 4.5. The figure shows both a cross-section through the symmetry axis (left) and a side view (right) of the trap. The trap indicated in Fig. 4.5 has a diameter for the inner electrode of 2 mm, and an inner diameter of the outer electrode of 12 mm. The shape of the inside of the latter electrode is parabolic in this example. The maximum electric field inside the trap is chosen to be equal to the maximum electric field that could be realized in the above-mentioned experiments ($|E_{max}| \approx$140 kV/cm). This corresponds to an applied voltage difference of 25 kV between inner and outer electrode. When metastable CO molecules are put into this trap at the proper position and with the correct initial velocity, they will be trapped in quasi-periodic orbits. The maximum incoming velocity of the CO molecules that still allows confinement into stable quasi-periodic orbits is determined by the maximum Stark shift that can be obtained, which in turn is limited by the maximum electric field that can be achieved.

A projected trajectory of a CO molecule inside the trap is indicated in both views of the trap. The trajectories are generated assuming that the CO molecules are prepared inside the trap in the $M\Omega$=1 component of the $a^3\Pi_1(v=0,\ J=1)$ level using a laser beam that is running parallel to the symmetry axis and close to the inner electrode (r=2 mm). Here the electric field, and hence the Stark shift, is largest. The tangential velocity of the CO molecules for which the trajectories are calculated is 22.1 m/s. Their velocity in the direction of the symmetry axis (z-axis) is 1.2 m/s. The maximum tangential velocity of the CO molecule that can be trapped is found to be 22.3 m/s for the presented configuration, assuming a maximum electric field of 140 kV/cm. The maximum velocity that can be trapped in the direction of the z-axis is found to be 2.0 m/s. It should be noted that ground state CO molecules hardly experience any force due to the electric fields because the (second order) Stark effect in the $^1\Sigma^+$ state is negligible as compared to the Stark effect in the $a^3\Pi$ state [16].

For the practical realization of the above-mentioned scheme one can start with a slow effusive beam of CO from a liquid N_2 cooled source. In such a beam the most probable velocity is about 200 m/s; a few percent of the molecules will have velocities below 22 m/s. After pre-selection of molecules with low velocity (using, for example, a mechanical velocity selector), this beam of ground state CO molecules can enter the trap perpendicularly to, and slightly above, the symmetry axis of the trap through a small (0.5 mm diameter) hole. The metastable molecules can be prepared by the above-mentioned narrow-band pulsed laser running parallel to the cylinder axis. As the electric field inside the trap scales approximately with $1/r$, there is a strong dependence of the Stark shift on the radial position. Assuming a bandwidth of 150 MHz for the preparation laser, it follows that in the radial direction only molecules over a distance of a few tens of micrometers will be in resonance with the laser. The spatial resolution of the excitation region will therefore be determined by the combination of laser bandwidth and field gradient rather than by the spot size of the laser beam. In principle the narrow-band laser can be used for velocity selection in the z-direction by scanning through the Doppler profile. As the Stark shift is much larger than the Doppler shift, however, spatial selection rather than velocity selection will be performed.

Visualization of the trajectories of the trapped CO molecules can be performed via time- and spatially-resolved imaging of the $a^3\Pi(v{=}0) \rightarrow X^1\Sigma^+(v'')$ fluorescence of the laser-prepared molecules [25]. The lifetime of the laser prepared level is around 3 ms [18, 19], which is well matched to the typical orbiting time for CO in the trap (0.5–1.5 ms). Several round-trips are performed inside the trap during the lifetime of the metastable molecules.

CO molecules in the $a^3\Pi_2(J{=}2,\ M\Omega{=}4)$ level can be used for confinement in this geometry as well. The linear Stark effect for this quantum-level is even larger than for the $a^3\Pi_1(J{=}1,\ M\Omega{=}1)$ level. The radiative lifetime of this level is around 160 ms [18] and excitation to this level is correspondingly more difficult. The much longer lifetime of this state, however, allows to accumulate molecules inside the trap for many laser pulses when a high repetition rate laser system is used.

4.5 Conclusions

The static confinement scheme as proposed here, works for CO because this molecule can be excited inside the trap to a metastable state, where the laser is used to 'switch on' the dipole moment. Otherwise 'planetary' orbits could not be accomplished. The scheme presented here will be applicable to all molecules that have this property. In addition, the scheme could work for ground state neutral molecules with a large dipole moment, provided the electric fields can be switched on sufficiently fast.

Apart from confinement, electric fields can be used to manipulate polar molecules on the basis of the linear Stark effect. If, for instance, CO molecules are prepared in an electric field in a quantum-level with a certain negative (positive) Stark shift, then the molecules will loose (gain) exactly this amount of kinetic energy upon entering a field-free region. The extent to which polar molecules can be slowed down or accelerated via this scheme is again determined by the magnitude of the Stark shift that can be realized.

Acknowledgements

This work has been realized in the framework of the EC-HCM network (ERB-CHR-XCT-94-0603) and is part of the research programme of the 'Stichting voor Fundamenteel Onderzoek der Materie (FOM)', which is financially supported by the 'Nederlandse Organisatie voor Wetenschappelijk Onderzoek (NWO)', and receives direct support by NWO via PIONIER-grant # 030-66-89.

References

[1] M.H. Anderson, J.R. Ensher, M.R. Matthews, C.E. Wieman, and E.A. Cornell, Science **269**, 198 (1995).

[2] J. Opt. Soc. Am. B **6**, (1989), Special Issue on Laser Cooling and Trapping of atoms, eds. S. Chu and C. Wieman.

[3] Laser Phys. **4**, (1994), Special Issue on Laser Cooling and Trapping, eds. V. Bagnato, N. Bigelow, A. Dykhne, J. Weiner, and Y. Yakovlev.

[4] A. Herrmann, S. Leutwyler, L. Wöste, and E. Schumacher, Chem. Phys. Lett. **62**, 444 (1979).

[5] J.T. Bahns, W.C. Stwalley, and P.L. Gould, J. Chem. Phys. **104**, 9689 (1996).

[6] J.P. Bucher, D.C. Douglas, P. Xia, B. Haynes, and L.A. Bloomfield, Z. Phys. D **19**, 251 (1991)

[7] D.R. Herrick, M.B. Robin, and A. Gedanken, J. Mol. Spectrosc. **133**, 61 (1989).

[8] J.M. Doyle, B. Friedrich, J. Kim, and D. Patterson, Phys. Rev. A **52**, R52 (1995).

[9] W.H. Wing, Phys. Rev. Lett.**45**, 631 (1980).

[10] B. Friedrich, and D. Herschbach, Phys. Rev. Lett. **74**, 4623 (1995).

[11] J. Reuss in *Atomic and Molecular Beam Methods*, Vol. I, ed. G. Scoles, (Oxford University Press, New York, 1988).

[12] H.J. Loesch, Chem. Phys. **207**, 427 (1996).

[13] S.K. Sekatskii, JETP Lett. **62**, 916 (1995).

[14] S.K. Sekatskii and J. Schmiedmayer, Europhys. Lett. **36**, 407 (1996).

[15] R.C. Stern, R.H. Gammon, M.E. Lesk, R.S. Freund, and W.A. Klemperer, J. Chem. Phys. **52**, 325 (1970).

[16] M. Drabbels, S. Stolte, and G. Meijer, Chem. Phys. Lett. **200**, 108 (1992).

[17] Chapter 2 of this thesis and
R.T. Jongma, Th. Rasing, and G. Meijer, J. Chem. Phys. **102**, 1925 (1995).

[18] T.C. James, J. Chem. Phys. **55**, 4118 (1971).

[19] Chapter 3 of this thesis.

[20] R.W. Field, S.G. Tilford, R.A. Howard, and J.D. Simmons, J. Mol. Spectrosc. **44**, 347 (1972).

[21] J.M.L.J. Reinartz, W.L. Meerts, and A. Dymanus, Chem. Phys. Lett. **16**, 576 (1972).

[22] W. Gordy and R.L. Cook, *'Microwave Molecular Spectra'*, 3^{rd} Ed., (John Wiley & Sons Inc., New York, 1984).

[23] The values for $c_{\Omega',\mathrm{i}}(J)$ are calculated using the model of Field et al. [20] to determine the energy of rotational levels in the $a^3\Pi$ state. In this model all the Ω-ladders are interacting with each other. The values of $c_{\Omega',\mathrm{i}}(J)$ are listed in the Appendix of chapter 3. From the wavefunction belonging to the specific quantum state labelled by J and Ω', the amount of Ω=i-character is calculated by squaring $c_{\Omega',\mathrm{i}}(J)$.

[24] D.A. Dahl, SIMION 3D Version 6.0, Idaho National Engineering Laboratory, Idaho Falls (U.S.A.), (1995).
[25] Chapter 5 of this thesis and
R.T. Jongma, G. Berden, Th. Rasing, H. Zacharias, and G. Meijer, J. Chem. Phys. (in press).

Chapter 5

State-to-state Scattering of Metastable CO Molecules from a LiF(100) Surface [1], [2]

Abstract

Scattering of electronically excited, state-selected metastable CO($a^3\Pi$) molecules from a cleaved LiF(100) surface is studied experimentally. Internal state distributions, fluorescence profiles, Time-Of-Flight (TOF) profiles and angular distributions of the surviving metastable CO molecules are measured. Relative and absolute survival probabilities are determined for various impact velocities. The dependence of translational and rotational temperature on the velocity of the incoming beam unambiguously indicates a direct inelastic scattering process, even though the angular distributions are broad, both in-plane and out-of-plane. The internal state distribution after scattering shows an overpopulation of the initially prepared Ω=1-component relative to the other spin-components.

---

[1] Adapted from: R.T. Jongma, G. Berden, D. van der Zande, Th. Rasing, H. Zacharias, and G. Meijer, Phys. Rev. Lett. **78**, 1375 (1997).

[2] and: R.T. Jongma, G. Berden, Th. Rasing, H. Zacharias, and G. Meijer, J. Chem. Phys. (in press).

5.1 Introduction

During the last decades many experiments on molecular beam-surface interaction have been performed [1, 2]. These experiments almost exclusively utilize molecules in their electronic and vibrational ground state. Measuring the velocity distribution, angular distribution, and internal state distribution of the scattered molecules for known parameters of the incoming beam and for a known scattering geometry, yields detailed information on the molecule-surface interaction potential [3–7].

A few groups have reported on scattering experiments in which vibrationally excited molecules are used [8–11]. So far, little is known about the interaction of electronically excited molecules with surfaces; the study of electronically excited molecules colliding with surfaces is thus far limited to molecules residing in the different Ω-components of the electronic ground state [12–14].

A variety of scattering experiments with metastable atoms have been performed, mostly focused on the electronically inelastic channels of the scattering process. This has led, amongst others, to the development of metastable atom deexcitation spectroscopy (MDS/MIES) as a surface spectroscopic tool [15, 16].

Recently the first scattering experiments with electronically excited CO molecules have been realized [17]. In this chapter we report in more detail on the state-to-state surface scattering experiment with quantum-state selected metastable CO molecules. By studying the electronically elastic channel only, the elastic scattering properties of the process are probed; each molecule being trapped or chemisorbed will be electronically deexcited and removed from the measured signal. Apart from information obtained from Time-Of-Flight (TOF) and angular distributions of the surviving metastable molecules, additional information concerning the interaction potential can be extracted from the internal state distribution of the scattered molecules.

5.2 Experimental

The experimental set-up consists of a pulsed molecular beam machine connected to an Ultra High Vacuum (UHV) system. A schematic view of this machine is presented in Fig. 5.1. Its operation has been described in detail earlier [18]. To summarize, the two differentially pumped chambers of the molecular beam machine are connected by a 0.8 mm diameter skimmer. The source chamber contains a pulsed valve (R.M. Jordan Co.) with a 0.35 mm orifice. In the experiments a mixture of 20% CO seeded in Neon, Argon, Krypton or Xenon is expanded from the nozzle, providing a supersonic beam of gas pulses with a duration of typically 20–30 μs. Different seeding gasses are used to vary the mean velocity of the CO molecules in the molecular beam. About 2 cm downstream from the nozzle the rotationally cold CO molecules are excited from the electronic ground state to the $a^3\Pi_1(v{=}0, J{=}1)$ level by direct laser excitation. To be able to focus the metastable CO molecules with a hexapole, the upper component of the $J{=}1$ Λ-doublet in the $a^3\Pi_1(v{=}0)$ state is populated via excitation on the $Q_2(1)$ line of the spin-forbidden $a^3\Pi(v{=}0)\leftarrow X^1\Sigma^+(v{=}0)$ transition (around 206 nm [19]) using pulsed laser radiation.

This laser light is produced with an argon-ion laser (Spectra Physics 2017) pumped cw-ring

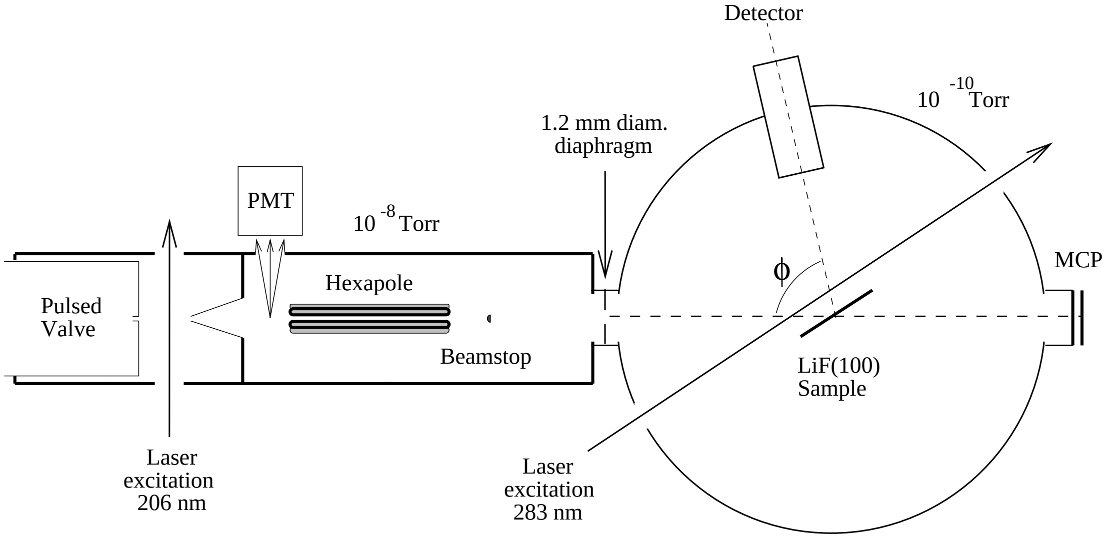

Figure 5.1: *Schematic view of the experimental setup, consisting of a pulsed molecular beam machine connected to an UHV scattering chamber. The 206 nm laser excitation in combination with the hexapole-beamstop-diaphragm setup allows preparation of a pure beam of metastable CO molecules in the UHV chamber. The production of metastable CO molecules is monitored in the hexapole chamber with the PMT. The TOF profile of the incoming beam is measured with the MCP in the UHV chamber. Direct detection of metastable CO molecules, detection of fluorescence photons, or ions prepared by the 283 nm laser is realized with several detection schemes as displayed in more detail in Fig. 5.2.*

dye laser system (Spectra Physics 380), running on a mixture of DCM and Rhodamine 6G, that produces 100 mW of 618 nm laser light in a 1 MHz bandwidth. The output of the cw-laser is amplified in a Nd:YAG laser (Spectra Physics GCR 190) pumped pulsed dye amplified system (Lambda Physik LPD3000) running on Sulforhodamine 640. The pulsed laser radiation around 618 nm is frequency-tripled in the combination of a KDP and a BBO crystal. The 206 nm laser light that is obtained (0.5 mJ in a 150 MHz bandwidth), is separated from the fundamental and second harmonic using a number of 45° mirrors for 206 nm laser light (R>98%, Laseroptik GmbH). The favourable spectral brightness of this laser system, as compared to normal pulsed dye lasers, allows efficient pumping on the $a^3\Pi \leftarrow X^1\Sigma^+$ transition.

After the molecular beam is skimmed, it enters the hexapole chamber. In this chamber a photomultiplier (PMT) is monitoring the a→X fluorescence of metastable CO molecules that pass through its field of view. This PMT is mounted perpendicular to the molecular beam axis, 7.5 cm downstream from the excitation region. The fluorescence signal is used to optimize spatial overlap and frequency of the excitation laser, and can be used as a reference for the number of metastable molecules present in the molecular beam.

The hexapole chamber contains a 15 cm long electrostatic hexapole state-selector as well as a 1.2 mm diameter beamstop blocking the central part of the beam. A 1.2 mm diameter diaphragm, connecting the hexapole chamber to the UHV system, is mounted in the 'shadow' of the beamstop. The beamstop thereby prohibits the unfocused molecular beam to enter the UHV system.

Metastable CO molecules in the upper Λ-doublet component with $M\Omega$=–1 (prepared by laser excitation on the $Q_2(1)$ transition) can be focused by the electrostatic hexapole state-selector based on the first order Stark effect [2, 20]. The voltage on the hexapole is optimized to bend molecules with a certain velocity in this specific quantum state around the beamstop and focus them precisely at the location of the opening of the diaphragm, as experimentally demonstrated earlier for this system [18]. The combination of hexapole, beamstop and diaphragm thus transmits an almost pure beam of metastable CO molecules in a single quantum state to the UHV system, in principle free of ground state CO and carrier gas atoms. Less than 1% of the ground state CO molecules and of the carrier gas atoms will enter the UHV system.

In the center of the UHV system, 72.5 cm downstream from the excitation region, a LiF sample is mounted on a X,Y,Z-manipulator. The manipulator also allows rotation of the sample around a vertical axis, thereby varying the angle of incidence. The LiF surface is chosen for these experiments as it is a likely candidate for which the internal energy of the metastable CO molecules (6.0 eV) will not be lost during the interaction.
The LiF sample is obtained from a 10x10 mm^2 rod of single crystalline LiF. The LiF samples are cleaved along the (100) direction, which is the only stable direction for cleaving, to provide an atomically flat surface. Cleaving is done under atmospheric conditions since there appear to be no differences between air-cleaved and vacuum-cleaved samples used in similar experiments [11, 21]. Within ten minutes after cleavage the sample is mounted and put in the UHV chamber, which is subsequently pumped down. After bake-out a base pressure of $2{\cdot}10^{-10}$ Torr is obtained. The LiF sample is heat-cleaned in UHV for a period of 2 hours at 600 K, and kept at room-temperature during the experiments. For a few samples the flatness of the surface was checked after the experiments (in open air) with an atomic force microscope. The resulting images show large, atomically flat terraces with a typical width of a few μm. The data presented here are reproduced in experiments with many different LiF samples.

5.2.1 Detection schemes

Direct detection of the metastable CO molecules is performed with Micro-Channel Plate (MCP) detectors which allow both time- and spatially-resolved detection [18]. The detection efficiency for $a^3\Pi(v{=}0)$ CO is approximately 6×10^{-4} [22]. This method is not quantum-state specific and is based on detection of electrons produced by Auger deexcitation. In the emission process the electronic energy of the metastable CO molecule (6.0 eV) is used to create electrons at the surface of the MCP detector, and these electrons are subsequently detected. The detection efficiency is therefore not expected to depend strongly on the internal and kinetic energy of the detected molecules. Similar detection schemes have been shown to be essentially independent of kinetic energy [23–26]. Furthermore, the MCP detector has been used earlier to measure excitation spectra in a molecular beam [18]. Rotational levels up to J=8 could be measured for CO molecules in the $a^3\Pi$ state, and the spectra could be fitted using a single rotational temperature, indicating that at least up to J=8 the effect of rotational energy on the detection efficiency can be neglected. If, however, part of the internal or kinetic energy can be used as well for the production of Auger electrons, the detection efficiency still would show only a minor dependence on these quantities as it is only a small contribution ($\leq$0.1 eV) to the 6.0 eV of electronic energy of the metastable CO molecules.

TOF profiles of the incoming metastable CO beam are monitored with a double staged, 25 mm diameter MCP detector (Fig. 5.1) when the LiF surface is moved out of the beam. This detector is mounted 98 cm downstream from the excitation region, and allows determination of the parallel velocity distribution of the incoming beam of metastable CO molecules.

The internal state distribution of the incoming and the scattered metastable CO beam is probed via one-color (1+1)-Resonance Enhanced Multi-Photon Ionization (REMPI) and mass-selective ion detection. The ions are produced by a laser that is resonant with the $b^3\Sigma^+(v{=}0)\leftarrow a^3\Pi(v{=}0)$ transition around 283 nm [27, 28]. This laser is a Nd:YAG pumped pulsed dye laser system (Spectra Physics GCR-3/PDL-2 combination) running on Fluorescein 548. The output of this laser is frequency-doubled in a KDP crystal, producing 10 mJ of 283 nm radiation with a bandwidth of 0.4 cm^{-1}. The laser intensity is more than sufficient to saturate the b$\leftarrow$a transition. For this reason the recorded spectra directly reflect the population in the $a^3\Pi$ state, and Hönl-London factors can be omitted in the analysis. The laser beam is running parallel to the LiF surface through the UHV machine, at a distance of 5 mm from the surface (see Fig. 5.1).

The laser-produced ions are accelerated in the direction of a fast 25 mm diameter MCP/phosphor screen (with a 80 ns decay time to 10% of peak signal) combination using the optional ion-extraction assembly (Fig. 5.2a). The extraction assembly consists of two concentric tubes. The inner tube has two parallel grids mounted at both ends, thereby creating a field-free TOF region of 19 cm for the laser produced ions. The outer tube is open at the side of the detector and has a grid mounted 3.2 cm away from the center of the LiF surface at the other side. The distance between the extraction grids of outer and inner tube at the side of the LiF sample is 3 mm.

At the end of the ion-extraction assembly the ions are accelerated toward the MCP/phosphor screen combination which is mounted 5 mm away from the end of the TOF tube. The total distance between LiF surface and MCP is 23 cm. The (spatially-integrated) emission of the phosphor screen is detected time-resolved with a PMT. The front of the MCP is biased at –1400 V. The voltage on the outer tube is V_1=–20 V, the voltage applied to the inner tube is V_2=–600 V. The mount of the LiF sample is grounded during all the experiments.

The voltages on the ion-extraction assembly are chosen to optimize the time separation between ions produced from the incoming and from the scattered beam. For the scattered molecules the velocity component in the direction of the MCP detector is much larger than for the molecules in the incoming beam. A low voltage on the first extraction grid (V_1) makes use of this difference to obtain an almost complete time-separation between the two signals. A high voltage on the second electrode (V_2) gives rise to rather narrow ions peaks.

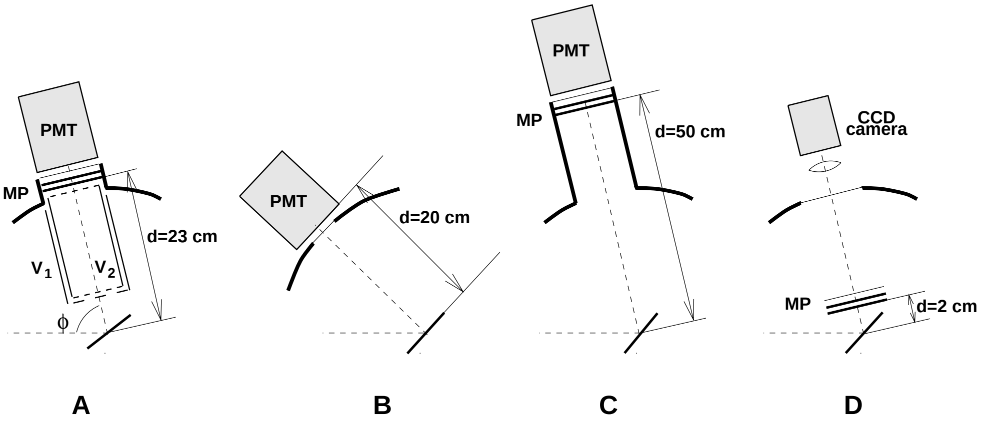

Figure 5.2: *Detailed view of the detection system in the UHV system:*
a) REMPI spectra are obtained using the ion extraction assembly mounted in front of a fast MCP/phosphor screen (MP) detection system. The (spatially integrated, time-resolved) emission of the phosphor screen is detected with a PMT. The extraction unit consists of two concentric tubes with extraction grids mounted at the end. The axis of the incoming metastable CO beam and the axis of detection enclose a fixed angle of $\phi = 72°$*.*
b) Spontaneous emission of incoming and scattered beam is monitored with a PMT directly looking at the fluorescence signal of the metastable CO molecules ($\phi = 36°$*).*
c) TOF profiles of scattered metastable CO molecules are detected with the same PMT-MCP/phosphor screen combination as shown in Fig. 5.2a, allowing direct detection of the metastable CO molecules ($\phi = 72°$*).*
d) Angular distributions of the scattered metastable CO molecules are measured, using a CCD camera system looking (time-integrated, spatially-resolved) at the emission of a MCP/phosphor screen combination similar to the one mentioned above.

In this detection scheme, the ions produced from the scattered beam arrive earlier on the detector than ions produced from the incoming beam, and can be sensitively detected. On resonance the ion signal of the incoming beam is a few orders of magnitude larger than the signal of the scattered beam and would, without this scheme, overwhelm the scattering signal.
The axis of the incoming beam of metastable CO molecules and the axis of detection of the scattered molecules enclose a fixed angle of ϕ=72° ($\phi = \theta_i + \theta_f$, with θ_i (θ_f) the angle enclosed by the surface normal and the incoming (scattered) beam) in this setup. The LiF sample is rotated to make an angle of incidence of θ_i=51° with the incoming metastable CO beam, allowing free passage of the REMPI laser, close to the LiF surface. The diameter of the laser beam is 6 mm, to probe scattered molecules in a rather large volume.

The spontaneous emission of the metastable CO molecules can be monitored with a PMT in the UHV chamber as well (Fig. 5.2b), allowing an estimation of the upper limit of the absolute survival probability by comparing the fluorescence signal of incoming and scattered metastable CO molecules. The PMT is mounted at a distance of 20 cm from the LiF(100) surface. The detection angle $\phi = 36°$. The fluorescence profiles of the metastable

CO molecules are recorded for the specular direction ($\theta_i = \theta_f = 36°$). Fluorescence profiles are measured with the LiF sample placed in the beam of metastable CO molecules and with the molecular beam hitting the stainless steel sample holder under otherwise identical circumstances. Stainless steel efficiently deexcites the metastable CO molecules and the thus recorded fluorescence profile will not contain a contribution of the fluorescence signal of the scattered molecules.

TOF profiles of the scattered metastable CO molecules are recorded by the PMT, registering the time-resolved and spatially integrated emission of the MCP/phosphor screen combination, located 50 cm away from the LiF surface (Fig. 5.2c, ϕ=72°). Molecules scattering in the specular direction are monitored (θ_i=θ_f=36°) to allow direct comparison with the fluorescence profiles.

Angular distributions of the scattered molecules are measured with a CCD-camera system recording the time-integrated emission of another 25 mm diameter MCP/phosphor screen detector, similar to the one mentioned above, but this time mounted 2 cm away from the LiF surface (Fig. 5.2d). The camera system has a gated image-intensifier which is at high voltage during typically a hundred μs, corresponding to the width of the arrival time distribution of the metastable CO beam at the detector.

5.2.2 Data acquisition

The signals recorded by the MCP (Fig. 5.1) or PMT (Fig. 5.2) are fed into a digital oscilloscope with a 10 bit vertical resolution (Lecroy 9430), where they are digitized and then read out by a computer (486PC) via a GPIB interface (National Instruments). The TOF profiles of the incoming beam are measured by summing the detected signal over typically 1500 shots in the 16 bit memory of the oscilloscope and by subsequent transfer to the PC.

The fluorescence profiles and TOF profiles of the scattered molecules are measured using time-resolved event counting. These signals are too low to average directly on the oscilloscope. Therefore the signal is typically summed over 120 shots in the memory of the oscilloscope and read out by the computer. The maximum of a certain signal peak that appears above a preset threshold is counted as a single event (detection of a metastable molecule or a photon) and put into a data array in the computer at a position corresponding to the detection time. The length of the time-interval over which the number of events is summed can be chosen afterward.

The use of the PMT or PMT-MCP/phosphor screen combination guarantees sensitive detection of single events due to the large amplification that can be obtained. The MCP/phosphor screen combination together with the CCD camera system (LaVision Flamestar) allows spatially resolved detection of single metastable CO molecules with a signal to noise ratio better than hundred. The software to control and read out the CCD camera can be used for two-dimensional (2D) event counting. The detected angular distribution is therefore free of noise caused by the dark-current of the CCD-chip.

The REMPI spectra are measured with the same detection system, allowing sensitive detection of ions. The signal is summed over typically 25 laser shots on the oscilloscope and read into the computer. The signal in a preset time-gate (corresponding to the arrival time of the ions) is averaged and recorded after subtraction of the baseline. The energy of the ionization laser and the number of metastable CO molecules in the beam, the latter monitored via the fluorescence signal on the PMT in the hexapole chamber, are recorded simultaneously with the ion signal. The fluorescence signal is averaged on a gated integrator/boxcar averager (Stanford Research Systems (SRS) 250) because of the large time delay between the fluorescence signal and the ion signal (on the order of a ms), and because of the presence of only two channels on the oscilloscope. The averaged output of the boxcar is digitized by a 13 bit digitizer (SRS 245) and read into the computer together with the oscilloscope signals. Thus recorded REMPI spectra can be corrected for intensity fluctuations in the beam of metastable CO molecules and for fluctuations in the energy of the ionization laser.

Synchronization of pulsed valve, laser(s) and oscilloscope or camera system is achieved with a delay generator (SRS DG535).

5.3 Results and discussion

5.3.1 Internal-state distributions

The two upper traces in Fig. 5.3 show experimental one-colour (1+1)-REMPI spectra of incoming and scattered beam. The incoming beam (upper trace) shows two peaks, both originating from the + parity component of the J=1 level in the $a^3\Pi_1$ state. Ionization occurs via the N=1 and N=3 level in the $b^3\Sigma^+(v=0)$ state, respectively. The absence of the N=0 and N=2 peak indicates that the electric fields used in the extraction region (below 10 V/cm), are not high enough to induce mixing of the two Λ-doublet components of the J=1 level.

The high laser power that is used, guarantees complete saturation of the allowed b←a transition. In the analysis of the spectrum of incoming and scattered beam, the Hönl-London factors of the b←a transition can therefore be omitted. The ionization step is not saturated, and the (1+1)-REMPI signal depends therefore linearly on laser power. The spectra are corrected for intensity fluctuations in the metastable CO beam and energy of the ionization laser. The peaks in the upper trace of the figure have equal intensity, as they both originate from the same level in the $a^3\Pi$ state.

The observed (1+1)-REMPI spectrum of the scattered CO molecules, shown in the middle trace of Fig. 5.3, yields the internal state distribution of the scattered metastable CO molecules. This spectrum is recorded for a mixture of 20% CO seeded in Ar at an angle of incidence θ_i=51°. The spectrum is observed to be much more dense than the spectrum of the incoming beam, indicating a strong redistribution within the $a^3\Pi$ state upon collision with the LiF(100) surface. The number of ions that is produced in the scattered beam is, on top of the strongest band-head, approximately a factor of 200 smaller than the number of ions that are produced when the incoming beam is probed.

The lower trace in Fig. 5.3 shows the best fit to the experimental spectrum, using a least-squares intensity fit of the entire spectrum. Frequencies of the transitions are obtained from literature [27, 28] and are kept fixed in the fitting procedure. The intensity $I_{J,\Omega}$ of each line, used for fitting the experimental data, is calculated from the population in a

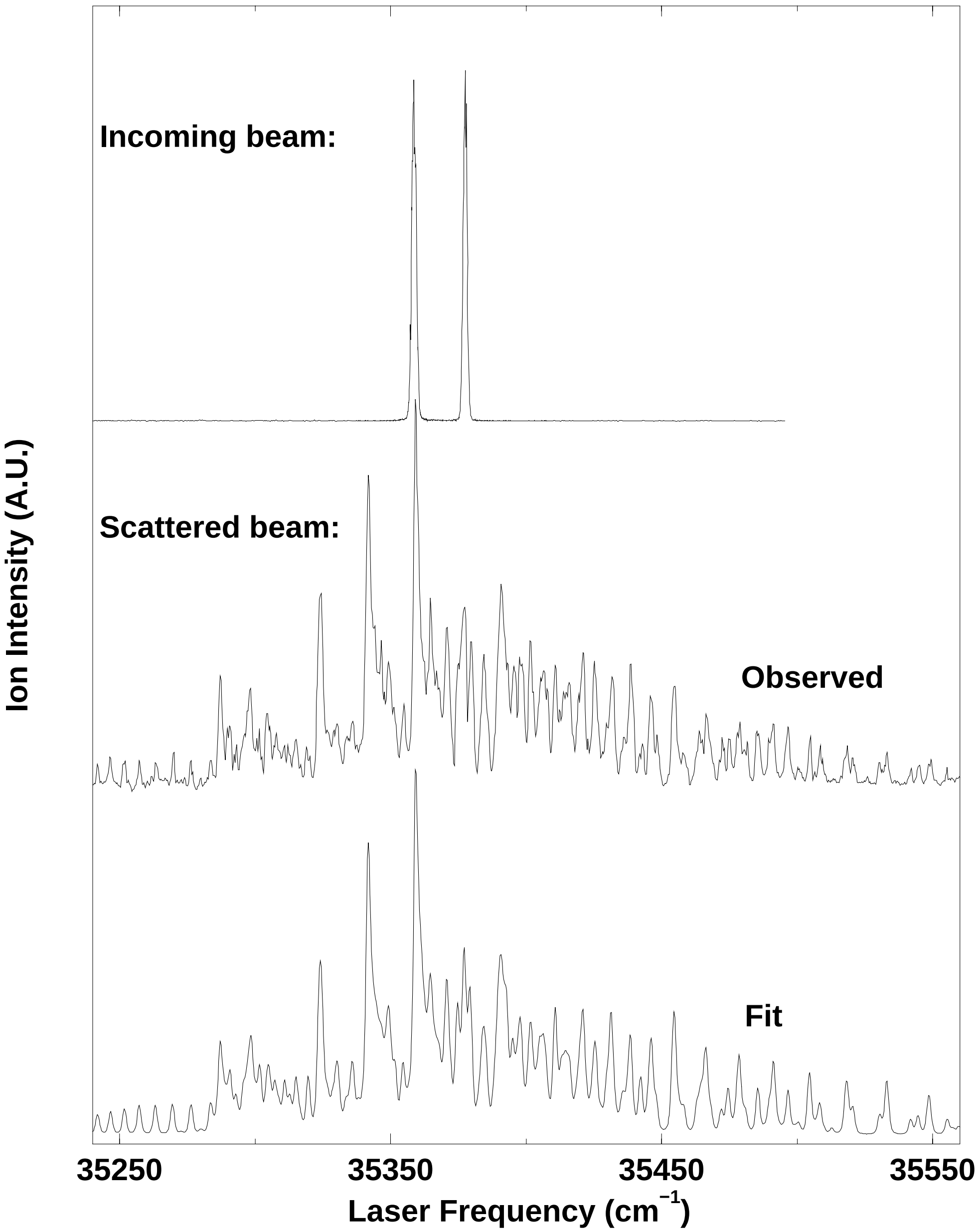

Figure 5.3: *Upper trace: REMPI spectrum reflecting the internal state distribution of the incoming beam. The two peaks both originate from the + parity component of the J=1 level in the* $a^3\Pi_1(v=0)$ *state. The experimental spectra are recorded for a gas mixture of 20% CO in Ar. Middle trace: REMPI spectrum which reflects the internal state distribution of scattered metastable CO molecules. This spectrum is recorded for* θ_i=51°. *Lower trace: Best fitting spectrum using a rotational temperature of 293 K, and an overpopulation of the* Ω=1 *component with a factor 2.5 relative to the other* Ω*-components.*

specific $a^3\Pi'_\Omega(J)$ level to be:

$$I_{J,\Omega'} = \left(\frac{c^2_{\Omega',0}(J)W_0}{N_0} + \frac{c^2_{\Omega',1}(J)}{N_1} + \frac{c^2_{\Omega',2}(J)W_2}{N_2}\right) \times (2J+1)\exp\left(-\frac{E_{J,\Omega'}}{kT_{rot}}\right) \tag{5.1}$$

in which:

$$N_{\mathrm{i}} = \sum_{\text{all levels}} c^2_{\Omega',\mathrm{i}}(J)(2J+1)\exp\left(-\frac{E_{J,\Omega'}}{kT_{rot}}\right) \tag{5.2}$$

for i=0, 1 or 2. Hönl-London factors are omitted in the fit for reasons explained above. The indicated quantum numbers J and Ω' are those of the $a^3\Pi$ state. The value $c^2_{\Omega',\mathrm{i}}(J)$ represents the amount of Ω=i (i=0, 1, or 2) character in the wave-function of the quantum state labelled by J and Ω' [29]. $W_{0,2}$ is the relative weight of the total population in levels with Ω=0 or 2 character with respect to the total population of levels with Ω=1 character. $E_{J,\Omega'}$ is the energy of the specific (J, Ω')-level in the $a^3\Pi$ state. The population in levels with Ω=i character is normalized by N_{i} (i=0, 1 or 2) which is the sum of the Boltzmann population $(2J+1)\exp\left(-\frac{E_{J,\Omega'}}{kT_{rot}}\right)$ over all levels weighted with the amount of Ω=i character. The rotational temperature is given as T_{rot}.

Normally the rotational temperature is defined with respect to a certain Ω-ladder, as for example can be done for NO in its electronic ground state [30–32]. In this electronic state, NO can be well described in the pure Hund's case (a) approximation for rotational levels up to J=20.5. For higher rotational levels, mixing of the different Ω-ladders will occur (determined by $Y=A/B$=72.5), and the energy levels must be calculated in a description intermediate between Hund's case (a) and (b). For CO in the $a^3\Pi$ state (Y=24.6), strong mixing of the different Ω-ladders occurs already above J=5, and Ω is no longer a good quantum number. Defining the population of a specific level as given in Eq. (5.1) attaches the rotational temperature not to a specific Ω-ladder (which is only valid in the pure Hund's case (a) approximation where Ω is a good quantum number), but to the Ω-character. This accounts for the increasingly mixed character of the wavefunction with increasing rotational quantum number.

A small fraction of the spectrum of the incoming beam had to be added to the scattered spectrum as well, probably caused by a few ions from the incoming beam appearing in the time gate centered on signal of the scattered beam.

A least-squares fit of the contour of the observed spectrum to Eq. (5.1) results in a rotational temperature T_{rot}=293±25 K. Fitting the spin-multiplet components with three different rotational temperatures does not improve the fit significantly. Best agreement with experiment is obtained when a non-equilibrium distribution for the three Ω components is assumed; in the final state distribution there appears to be an overpopulation of the (initially prepared) Ω=1 component relative to both the Ω=0 and Ω=2 component, as can be seen from the values for W_i given in Table 5.1. This table contains the rotational temperature and the values for W_i as obtained from the fit for all of the carrier gasses, together

Table 5.1: *For each of the carrier gasses used, the rotational temperature and weight of the population of the* Ω*=0 and 2 character relative to the population of the* Ω*=1* ($W_{0,2}$) *as obtained from the best fit to the experimental spectrum as well as the internal energy* E_{int} *that is gained in the collision with the surface (calculated from the fit-parameters) is given (for* $\theta_i = 51^\circ$ *and a surface temperature of* $T_s = 298K$*).*

Carrier gas	T_{rot} (K)	W_0	W_2	E_{int} (meV)
Ne	360±30	0.56±3	0.49±3	28±4
Ar	293±25	0.39±2	0.40±2	24±3
Kr	330±25	0.27±4	0.47±5	26±4
Xe	243±20	0.56±5	0.57±6	20±3

with the corresponding gain in internal energy E_{int} with respect to the (J=1,Ω=1)-level, as calculated using these parameters. The situation with W_0=W_2=0 would correspond to conservation of Ω=1 character, while the situation with W_0=W_2=1 corresponds to a completely (electronically and rotationally) thermalized Boltzmann-like distribution.

The rotational temperature tends to decrease with decreasing velocity of the incoming beam. The overpopulation of the initially prepared Ω=1 character is obvious for all of the carrier gasses. Striking is the equal population of levels with Ω=0 and 2 character for almost all of the carrier gasses.

5.3.2 Fluorescence profiles

Fluorescence profiles are measured for two different situations: the first is with the LiF(100) surface positioned in the molecular beam, the second with the molecular beam hitting the stainless steel sample holder under otherwise identical circumstances. Since stainless steel very efficiently deexcites the metastable CO molecules via an Auger process, in which the internal energy of the CO molecules is used to emit an electron from the surface [33], the fluorescence profile measured with this target in the molecular beam only shows fluorescence caused by metastable CO molecules in the incoming beam. The difference signal between profiles measured with LiF(100) and stainless steel target provides the fluorescence signal of the scattered metastable CO molecules. The profiles are measured for a mixture of 20% CO seeded in Neon, because the survival probability for faster molecules is larger (*vide infra*).

The upper trace of Fig. 5.4 shows the fluorescence signal as obtained for the first situation. The horizontal axis shows the time after laser excitation. The vertical axis shows the number of counted photons. The lower trace represents the (noisy) difference signal between the situation with LiF target and stainless steel target. The vertical dashed line shows the mean arrival time of the incoming beam at the position of the LiF surface. At this time a small, 150 μs wide peak is observed. The height of this peak is a direct measure for the upper limit of the survival probability.

Because the internal state distribution of the scattered molecules is probed as well (see

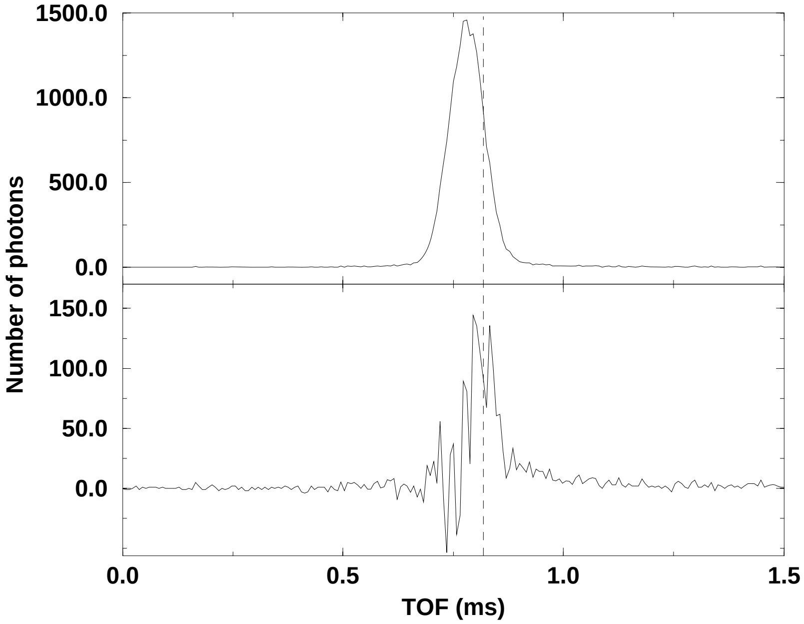

Figure 5.4: *Upper trace: Fluorescence profile of metastable CO obtained with the LiF sample placed in the molecular beam. The profile is recorded for a 20% CO in Ne mixture. Lower trace: Fluorescence profile obtained by taking the difference between the upper profile and a similar profile measured by replacing the LiF sample by the stainless steel sample holder under otherwise identical circumstances. Vertical dashed line: mean arrival time of incoming metastable CO beam at LiF surface.*

previous section), the time-evolution of the fluorescence profile of the scattered metastable CO molecules can be calculated by summing the exponentially decaying curves for each of the populated levels. This is done because the lifetime in the $a^3\Pi$ state is strongly dependent on rotational- and Ω-quantum number [34]. The (integrated) intensity of each exponential is weighted with the population of the specific quantum state. From the calculated fluorescence profile it is deduced that, for a typical distribution of population as deduced from the REMPI experiments (the parameters to obtain this distribution are listed in Table 5.1), the fluorescence yield of scattered metastable CO molecules is a factor 2.5 smaller than the fluorescence yield of metastable CO molecules in the incoming beam. Taking the effect of the change in fluorescence yield into account, the upper limit for the survival probability is calculated to be (18±8)%.

Because the signal peak in the lower trace coincides with the arrival time of the incoming beam and has a width comparable to the TOF distribution of the incoming beam (see next session), it is tempting to state that this peak can (at least partly) be explained by enhanced fluorescence, caused by the interaction of the CO molecule with the LiF surface. Assuming the entire peak to be explained by this mechanism, the efficiency of deexcitation via this mechanism is still only on the order of 10^{-4} of the total number of incoming molecules. The broad background signal that is observed at larger flight times, however, must be explained by fluorescence signal of scattered molecules anyway.

5.3.3 Time-of-flight profiles

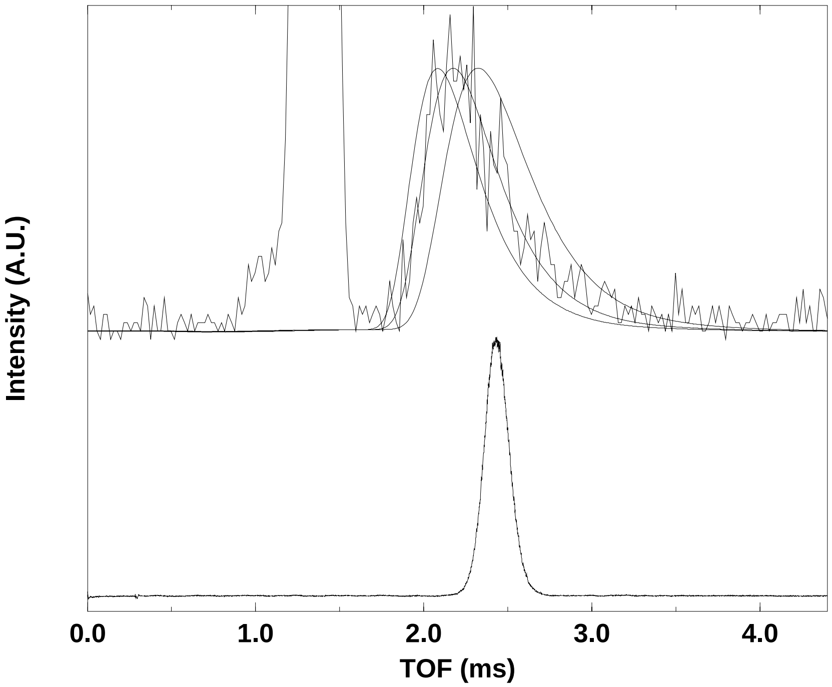

Figure 5.5: *Measured TOF profiles of both incoming (lower trace) and scattered (upper trace) metastable CO molecules for a mixture of 20% CO in Kr. On the horizontal axis the time relative to the laser-preparation is indicated. The lower trace shows the measured TOF distribution of the incoming beam (the horizontal axis is rescaled to allow direct comparison with the scattered TOF distribution). The upper trace includes the scattered TOF distribution (second peak) and the best fit (T_{trans}=285 K) as well as calculated TOF profiles for T_{trans}=185 K (right) and 385 K (left). The first peak (off-scale) corresponds to spontaneous fluorescence of the laser-prepared metastable molecules.*

Figure 5.5 shows the TOF profiles of both incoming and scattered metastable CO molecules as measured for a 20% CO in Kr mixture. In the lower trace the TOF profile of the metastable CO molecules impinging on the LiF surface, as detected with the MCP (Fig. 5.1), is shown. The corresponding velocity distribution has a width (FWHM) of less than 10% of the mean velocity. The time axis of the lower trace is rescaled to correspond to a flight path (72.5 cm + 50 cm) which is identical to the flight path that the scattered metastable CO molecules must travel to reach the MCP/phosphor screen combination (Fig. 5.2a). This allows direct comparison of the TOF distributions of incoming and scattered metastable CO molecules as shown in Fig. 5.5.

The first peak (off scale) in the upper trace in Fig. 5.5 is due to the fluorescence of metastable CO molecules decaying to the electronic ground state; the detected fluorescence is emitted in the direction of the MCP detector by molecules that are passing through the field of view of this detector from the moment that they enter the UHV chamber until they hit the LiF surface. The origin of this peak is confirmed by installing a Suprasil 1 window in front of the MCP detector. In this setup the fluorescence peak was still present, while even at the maximum of the scattered metastable signal no significant amount of fluorescence signal was visible. The time-integrated fluorescence signal is a direct measure for the number of incoming molecules.

The second peak in the upper trace corresponds to the TOF distribution of the scattered molecules. This peak is clearly broader than the distribution of the incoming beam (lower trace) and has a tail to larger flight times. The profile of scattered CO molecules is fitted to the convolution of the measured velocity distribution of the incoming beam at the position of the LiF surface (as can be calculated by rescaling the time axis to correspond to the flight path needed to reach the LiF surface, which is 72.5 cm) and a Maxwellian velocity distribution. In thermal equilibrium, the number of molecules with absolute velocity between v and $v + dv$ is given by

$$f(v)dv = Cv^2 \exp\left(-\frac{mv^2}{2kT_{trans}}\right) \exp\left(-\frac{A}{v}\right) dv \tag{5.3}$$

The first two terms describe a Maxwellian velocity distribution with a Boltzmann temperature T_{trans} whereas the last term is included to take the velocity dependent survival probability (*vide infra*) into account. The factor C is a normalization constant. From this velocity distribution it is calculated that the number of molecules that will reach the surface of the MCP detector in a time interval between t and $t + dt$ is given by [35, 36]:

$$F(t)dt = C't^{-4} \exp\left(-\frac{m(l/t)^2}{2kT_{trans}}\right) \exp\left(-\frac{At}{l}\right) dt \tag{5.4}$$

where l is the distance between surface and detector and C' is a normalization constant. The convolution is performed in the time domain. The best fitting curve, with $T_{trans} = 285$ K, is superimposed on the experimental trace of Fig. 5.5. For comparison, also traces with translational temperatures of 185 K (right peak) and 385 K (left peak) are indicated in the figure. It should be noted that the effect of the finite lifetime of the scattered metastable CO molecules on the TOF distributions of the scattered CO molecules, as described above for the fluorescence profiles, should in principle be accounted for in the analysis as well [the lifetime of the J=1 level in the Ω=1 ladder is around 3 ms, lifetimes of other levels are all (much) larger than this value [22, 34]]. Neglecting the finite lifetime, however, barely influences the determination of the Boltzmann temperature.

In many cases a shifted Maxwell velocity distribution with a drift velocity is fitted to the experimental TOF profiles. Since the fit is already almost perfect, adding an extra fit-parameter would not significantly improve the fit and would give unreliable results because of the strong coupling between the drift velocity and the translational temperature.

All TOF measurements have been performed for four different carrier gasses, i.e. for four different incoming velocities. The results are displayed in Fig. 5.6. The best fits to these profiles are superimposed on the experimental traces. For each of these fitted profiles the average velocity v_{in} and kinetic energy E_{in} of the incoming beam, the best fitting Boltzmann temperature T_{trans}, and the corresponding averaged velocity (v_{det}) and kinetic

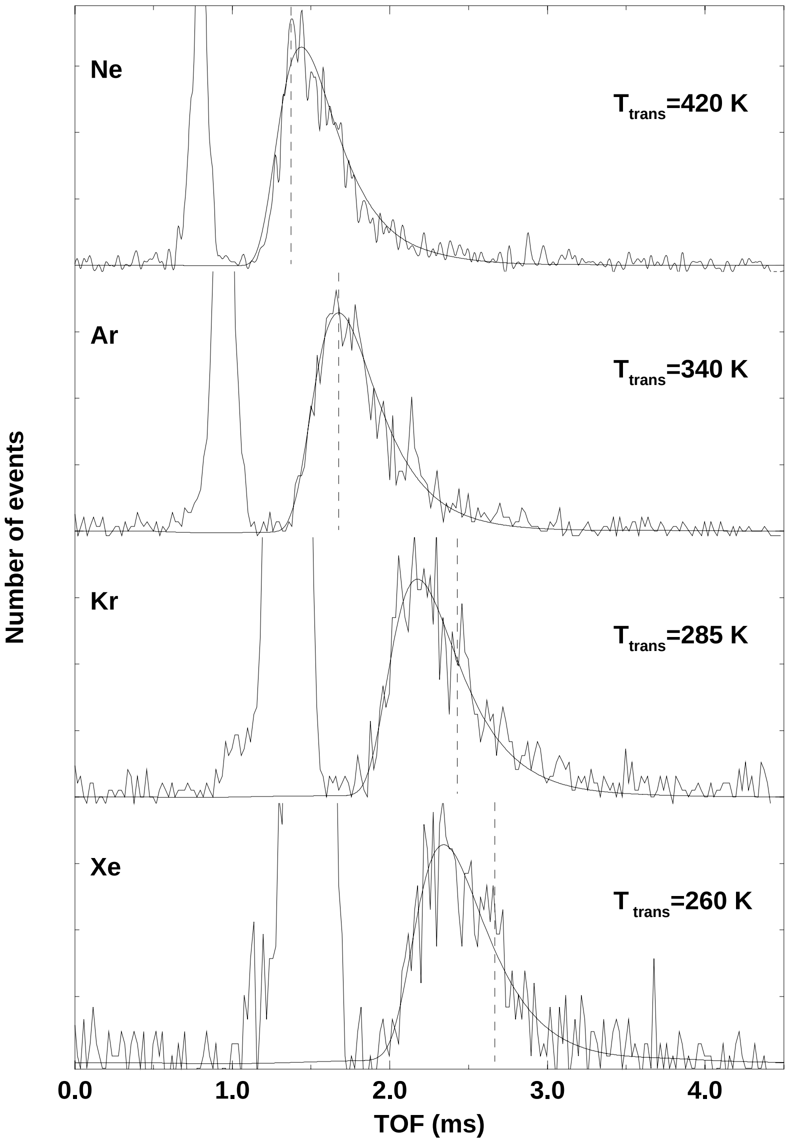

Figure 5.6: *Measured TOF profiles of scattered metastable CO molecules for mixtures of 20% CO in Ne, Ar, Kr and Xe. The best fit is superimposed upon the experimental traces. The dashed line, indicated for each of the TOF profiles, shows the averaged arrival time for a completely elastic scattering process, as obtained from the TOF distribution of the incoming beam.*

energy (E_{det}) of the outgoing beam as present on the detector, are listed in Table 5.2. The dashed lines in Fig. 5.6 indicate the averaged arrival time, obtained from the TOF distribution of the incoming beam assuming a completely elastic scattering process. From comparing the TOF profiles of the scattered metastable CO molecules to the averaged arrival time for completely elastic scattering it is concluded that for CO seeded in Ne the scattered beam is slower than the incoming beam. This is the expected behaviour for a superthermal molecular beam scattering from a room temperature surface. For CO seeded in Ar the incoming beam and the scattered beam are (almost) equally fast. For CO seeded in Kr and Xe, the scattered molecules are significantly faster than molecules in the incoming beam. This apparent acceleration is caused by the velocity dependent survival probability (see below), that is taken into account by the last exponential in Eqs. 5.3 and 5.4. This effect is also clear from the data listed in Table 5.2: it is seen that E_{det} is superthermal (>37.5 meV) for all of the carrier gasses used and that for CO seeded in Kr and Xe the averaged velocity of the scattered molecules is larger than the averaged kinetic energy of the incoming beam. Because faster molecules have a larger probability to survive the collision with the surface as a metastable molecule than slower molecules (see below), this leads to a velocity distribution of the detected scattered molecules that is skewed to larger velocities.

The translational temperature as obtained from the fit is seen to decrease gradually in going from Ne to Xe and this shows that the velocity distribution of the scattered molecules is not completely accommodated to the surface. The translational temperature is (within error) independent of the azimuthal angle (for non-specular scattering). It is noted that the angle of incidence for the determination of the rotational temperature is different from the angle used for measuring the translational temperature. Because the averaged impact energy is different, direct comparison of these temperatures is impossible, although they show a similar trend.

Table 5.2: *For each of the carrier gasses used, the averaged velocity v_{in} and averaged kinetic energy E_{in} of the incoming beam, the best fitting Boltzmann temperature T_{trans} and the corresponding averaged velocity v_{det} and kinetic energy E_{det} of the outgoing beam at the detector are given in the table (all for $\theta_i = 36°$ and a surface temperature of $T_s = 298K$).*

Carrier gas	v_{in} (m/s)	E_{in} (meV)	T_{trans} (K)	v_{det} (meV)	E_{det} (meV)
Ne	884±9	113.8±12	420±30	722±22	83±5
Ar	732±7	77.8±8	340±35	660±30	69±6
Kr	504±5	36.9±4	285±50	613±45	59±9
Xe	461±4	31.0±3	260±55	593±50	55±10

The ratio of the integrated scattered metastable CO signal to the product of the integrated fluorescence signal with v_{in} is presented in Fig. 5.7 (circles with error bars) for each of the carrier gasses used. This number is a measure for the survival probability (SP). It is seen from the data that the relative SP is decreasing with a decrease of the velocity of the incoming CO molecules.

The measured velocity dependence of the SP can, in a simple model, be used to quantitatively determine the SP. In this model the SP at the surface is assumed to be exponentially decaying with the interaction time with the surface, where the latter is taken to be proportional to ($1/v_{in}$+$1/v_{out}$). The quantity v_{out} is obtained using Eq. (5.3), the best fitting

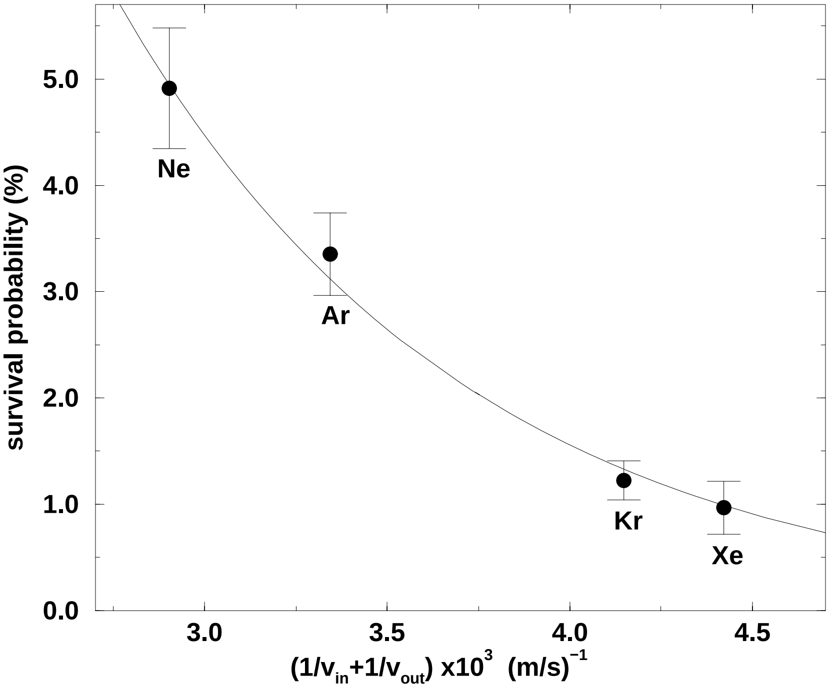

Figure 5.7: *The circular points (with error bar) represent the relative survival probability for the carrier gasses used. The value plotted on the horizontal axis (*$1/v_{in}+1/v_{out}$*) is, in approximation, proportional to the residence time on the surface for scattering at specular angles. The smooth curve shows the best fit to the experimental data points, allowing the determination of absolute survival probability. The vertical axis is rescaled to correspond to the absolute survival probability as obtained from this fit.*

translational temperature, and omitting the velocity dependent survival probability from this expression. In Fig. 5.7 $1/v_{in} + 1/v_{out}$ is plotted on the horizontal axis. Fitting the experimentally determined relative survival probabilities to this model determines the value of A in Eq. (5.3) and yields the absolute survival probabilities for the various carrier gasses (assuming the boundary conditions that a zero interaction time gives a SP of 1, and an infinite interaction time gives a SP of 0). The vertical axis of Fig. 5.7 is rescaled to correspond to the absolute survival probability as obtained from the fit (indicated by the solid line in the figure). Because the translational temperature (and thus the velocity in the outgoing channel v_{out}) and A are coupled to each other, a few iteration cycles have been performed to determine the stable values of A and T_{trans}.

5.3.4 Angular distributions

The angular distributions are measured with the MCP/phosphor screen combination as indicated in Fig. 5.2d. A typical grey scale image measured with this detector is given in Fig. 5.8 for a mixture of 20% CO in Ar and an angle of incidence of θ_i=60°. The angular distribution is obtained by using 2D event counting and summing over typically $1.5{\cdot}10^5$

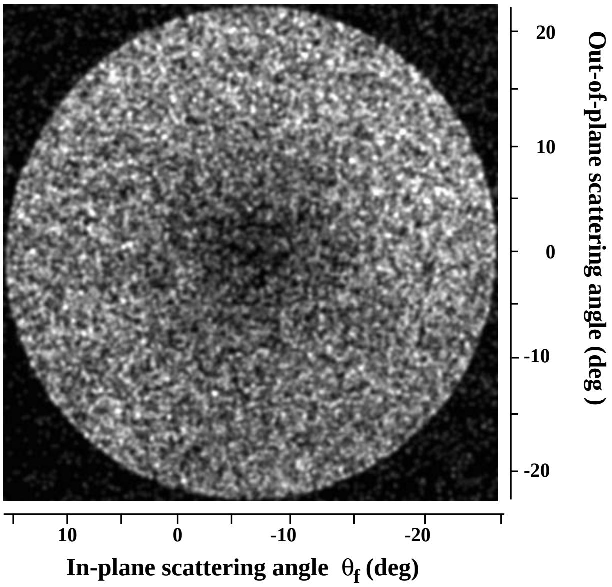

Figure 5.8: *Two dimensional grey scale image of the angular distribution (θ_i = 60°) of the metastable CO molecules taken with MCP 3. The 'hole' in the distribution in the middle of the MCP is a result of the bias angle of the channels leading to an angle-dependent reduction in sensitivity of the MCP detection system.*

laser shots. Both in-plane and out-of-plane scattering angles are indicated in the figure. The distribution of scattered metastable CO molecules is observed to be very broad, both in-plane and out-of-plane. The 'hole' that is visible in the middle of this image is caused by the bias angle of the channels in the MCP which causes an angular dependent detection efficiency; metastable molecules coming in under the bias angle penetrate the channels and are detected less efficiently. By moving the sample relative to the 2D-imaging detector, this 'hole' in the distribution can be moved out of the images; the angular distribution of the scattered molecules is accurately determined if the sample is moved over a distance of 1 cm in the direction of the excitation region.

Figure 5.9 shows the in-plane angular distribution that is obtained by taking a horizontal profile of such a 2-D image (circular dots), corrected for all effects concerning solid angle of detection and pixel size. The horizontal axis is rescaled to correspond to the scattering angle θ_f. The smooth curve indicated in the figure shows a cosine distribution, the best fit to the experimental data points. Squared and cubed cosine distributions do not fit the experimental data as well. The deviation of the experimental data points from the cosine curve for lower scattering angles can again be explained by the angular dependent sensitivity of the MCP detector. Similar experiments have also been performed for all the other carrier gasses and show an equally broad, cosine-like angular distribution.

For a direct scattering process, generally the parallel momentum is conserved and the angular distribution of the scattered molecules is close to specular [1]. The broad angular distribution on itself might indicate a trapping-desorption mechanism, but as trapping

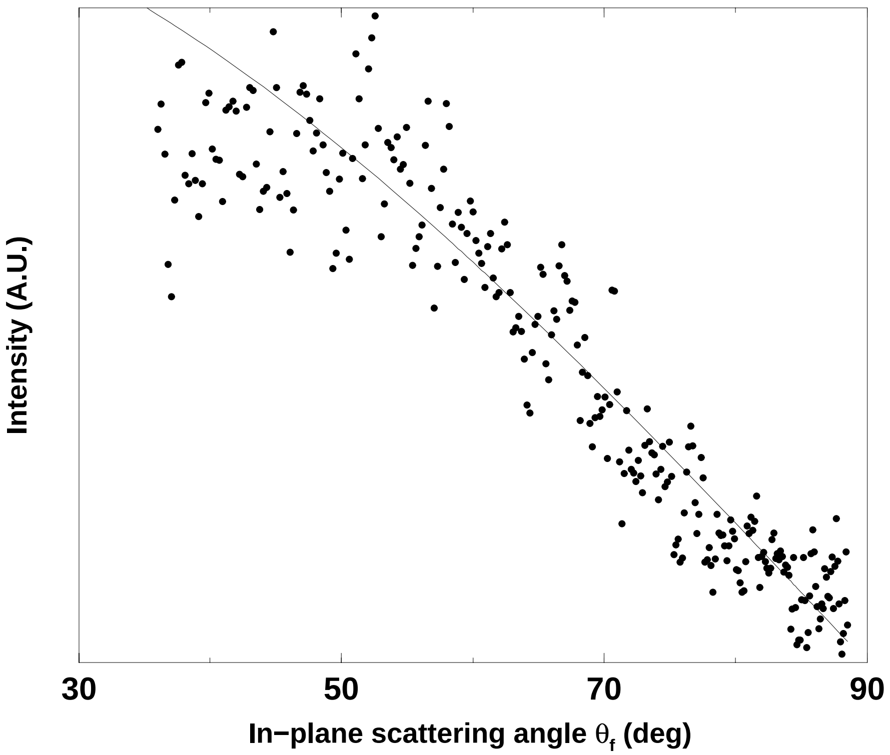

Figure 5.9: *In-plane angular distribution of scattered metastable CO molecules, as obtained from a 2-D image as shown in Fig. 5.8. The circular points show the experimental data as obtained for a mixture of 20% CO in Ar, and an angle of incidence* θ_i*=33°. The smooth curve shows a cosine distribution.*

of the metastable molecules is most probably followed by electronic deexcitation this is not very likely to happen. In the scattering of metastable rare gas atoms from LiF(100) surfaces it has also been found that the angular distributions are much wider than those of the respective ground state atoms [37], which is attributed to the marked change in interaction potential. Also in our case the broad angular distributions might be caused by the detailed character of the molecule-surface interaction potential; LiF is an ionic crystal, and the large dipole moment of the metastable CO molecules (1.37 Debye [38]) will interact with the various Li(+)-F(−) dipoles at the surface. Since LiF is a cubic crystal, these surface dipoles are both in the horizontal and the vertical direction, inducing not only a broad in-plane distribution but also a very broad out-of-plane distribution.

5.4 Conclusions

In this chapter we have presented state-to-state scattering experiments with laser-prepared metastable molecules. The survival of electronically excited, state-selected CO molecules, colliding with a cleaved LiF(100) surface, is analyzed using time- and spatially-resolved detection techniques. The absolute survival probability for metastable CO scattering from

LiF(100) is observed to be between 1 and 5% for the conditions used in the experiments, consistent with the upper limit of 18% obtained from the fluorescence profiles. A clear increase of the survival probability with an increasing velocity is observed.
The translational temperature, obtained from the TOF profiles of the surviving metastable CO molecules, shows that the metastable CO molecules are scattered from the surface with incompletely thermalized velocities. The rotational temperature shows a similar trend and it is concluded therefore that the metastable CO molecules undergo direct inelastic scattering. The population in the initially prepared Ω=1-character is larger than the population in the other spin-components.
The angular distributions are observed to be broad which might be attributed to the strong corrugation of the electrostatic interaction potential in the CO*/LiF(100) system.

Acknowledgements

We thank Carsten Menzel for fruitful discussion and preparation of the LiF crystals, J. Gerritsen for characterizing the LiF surfaces and C.A. Sikkens, J.G.H. Hermsen and C.A. Timmer for technical support. This work has been realized in the framework of the EC-HCM network (ERB-CHR-XCT-94-0603).

References

[1] J.A. Barker and D.J. Auerbach, Surf. Sci. Reports **4**, 1 (1984).

[2] *Atomic and Molecular Beam Methods*, Vol. I and II, ed. G. Scoles, (Oxford University Press, New York, 1988/1992).

[3] C.W. Mulhausen, J.A. Serri, J.C. Tully, G.E. Becker, and M.J. Cardillo, Isr. J. Chem. **22**, 315 (1982).

[4] A.W. Kleyn, A.C. Luntz, and D.J. Auerbach, Phys. Rev. Lett. **47**, 1169 (1981).

[5] E.W. Kuipers, M.G. Tenner, A.W. Kleyn, and S. Stolte, Nature **334**, 420 (1988).

[6] D.A. Mantell, S.B. Ryali, G.L. Haller, and J.B. Fenn, J. Chem. Phys. **78**, 4250 (1983).

[7] M. Asscher, W.L. Guthrie, T.-H. Lin, and G.A. Somorjai, Phys. Rev. Lett. **49**, 76 (1982).

[8] J. Misewich, C.N. Plum, G. Blyholder, P.L. Houston, and R.P. Merill, J. Chem. Phys. **78**, 4245 (1983).

[9] H. Zacharias, M.M.T. Loy, and P.A. Roland, Phys. Rev. Lett. **49**, 1790 (1982).

[10] M. Gostein, H. Parhikhteh, and G.O. Sitz, Phys. Rev. Lett. **75**, 342 (1995).

[11] J. Misewich, H. Zacharias, and M.M.T. Loy, Phys. Rev. Lett. **55**, 1919 (1985).

[12] A.C. Luntz, A.W. Kleyn, and D.J. Auerbach, Phys. Rev. B **25**, 4273 (1982).

[13] G.D. Kubiak, J.E. Hurst, H.G. Rennagel, G.M. McClelland, and R.N. Zare, J. Chem. Phys. **79**, 5163 (1983).

[14] D.A. Mantell, Y.-F. Maa, S.B. Ryali, G.L. Haller, and J.B. Fenn, J. Chem. Phys. **78**, 6338 (1983).

[15] W. Sesselmann, H. Conrad, G. Ertl, J. Küppers, B. Woratschek, and H. Haberland, Phys. Rev. Lett. **50**, 446 (1983).

[16] W. Maus-Friedrichs, S. Dieckhoff, and V. Kempter, Surf. Sci. **249**, 149 (1991).

[17] R.T. Jongma, G. Berden, D. v.d. Zande, Th. Rasing, H. Zacharias, and G. Meijer, Phys. Rev. Lett. **78**, 1375 (1997).

[18] Chapter 2 of this thesis and
R.T. Jongma, Th. Rasing, and G. Meijer, J. Chem. Phys. **102**, 1925 (1995).

[19] R.W. Field, S.G. Tilford, R.A. Howard, and J.D. Simmons, J. Mol. Spectrosc. **44**, 347 (1972).

[20] K.H. Kramer, and R.B. Bernstein, J. Chem. Phys. **42**, 767 (1965).

[21] J. Estel, H. Hoinkes, H. Kaarmans, H. Nahr, and H. Wilsch, Surf. Sci. **54**, 393 (1976).

[22] Chapter 3 of this thesis.

[23] R. Hemmen and H. Conrad, Phys. Rev. Lett. **67**, 1314 (1991).

[24] M.R. Woodard, R.C. Sharp, M. Seely, and E.E. Muschlitz, J. Chem. Phys. **69**, 2978 (1978).

[25] B. Brutschy and H. Haberland, Phys. Rev. A **19**, 2232 (1979).

[26] W.L. Borst, G. Nowak, and J. Fricke, Phys. Rev. A **17**, 838 (1978).

[27] G.H. Dieke and J.W. Mauchly, Phys. Rev. **43**, 12 (1933).

[28] T. Rytel, J. Mol. Spectrosc. **145**, 420 (1991).

[29] The values for $c^2_{\Omega',\mathrm{i}}(J)$ are calculated using the model of Field et al. [19] to determine the energy of rotational levels in the $\mathrm{a}^3\Pi$ state. In this model all the Ω-ladders are interacting with each other. From the wavefunction belonging to the specific quantum

state labelled by J and Ω', the amount of Ω=i-character is calculated. The values of $c_{\Omega',\mathrm{i}}(J)$ are listed in the Appendix of chapter 3.

[30] A.E. Wiskerke, C.A. Taatjes, A.W. Kleyn, R.J.W.E. Lahaye, S. Stolte, D.K. Bronnikov, and B.E. Hayden, Chem. Phys. Lett. **216**, 93 (1993).

[31] K. Fukutani, Y. Murata, R. Schwarzwald, and T.J. Chuang, Surf. Sci. **311**, 247 (1994).

[32] A.E. Wiskerke, C.A. Taatjes, A.W. Kleyn, R.J.W.E. Lahaye, S. Stolte, D.K. Bronnikov, and B.E. Hayden, J. Chem. Phys. Lett. **102**, 3835 (1995).

[33] H.D. Hagstrum, Phys. Rev. **96**, 336 (1954).

[34] T.C. James, J. Chem. Phys. **55**, 4118 (1971).

[35] P.M. Ferm, F. Budde, A.V. Hamza, S. Jakubith, G. Ertl, D. Weide, P. Andresen, and H.-J. Freund, Surf. Sci. **218**, 467 (1989).

[36] F. Budde, T. Gritsch, A. Mödl, T.J. Chuang, and G. Ertl, Surf. Sci. **178**, 798 (1986).

[37] H. Conrad, G. Ertl, J. Küppers, W. Sesselmann, B. Woratschek, and H. Haberland, Surf. Sci. **117**, 98 (1982).

[38] R.C. Stern, R.H. Gammon, M.E. Lesk, R.S. Freund, and W.A. Klemperer, J. Chem. Phys. **52**, 325 (1970).

Chapter 6

Scattering of Vibrationally and Electronically Excited CO Molecules from a LiF(100) Surface [1]

Abstract

Experiments are performed in which vibrationally and electronically excited CO($a^3\Pi$, v=1) molecules are scattered from a LiF(100) surface. As there is originally no population in the vibrationless level of the metastable state, this experiment gives the unique possibility to probe the vibrationally inelastic channel in the scattering of vibrationally excited molecules. The vibrational deactivation probability can thus be accurately determined and is found to be below 10^{-3} for the system under study.

---

[1] Adapted from: R.T. Jongma, G. Berden, Th. Rasing, H. Zacharias, and G. Meijer, Chem. Phys. Lett. (submitted).

6.1 Introduction

The use of molecular beams in surface scattering enables a detailed investigation of the interaction potential between molecules and surfaces. The importance of the vibrational degree of freedom of the molecules for the determination of the interaction potential has been reviewed by Houston and Merrill [1] in 1988, and more recently by Rettner et al. [2]. For the first time unambiguous vibrational excitation has been observed for ground state NO molecules scattered from a Ag(111) surface in essentially a single gas-surface encounter [3]. Molecular beam studies in which vibrationally excited molecules are scattered from surfaces are thus far rather limited in number [4–15]. An important parameter to be determined is the vibrational survival probability, or, alternatively, the vibrational deactivation probability. This is, however, a difficult observable as one has to average over scattering angle, velocity distribution, and final state-distribution to determine the total fraction of molecules in the vibrationally elastic channel. A rather large experimental error is intrinsic to this procedure.

The survival probabilities for vibrationally excited molecules scattering from clean, well-defined, and atomically flat surfaces range from 0.6 up to almost unity, depending on the experimental conditions. For vibrationally excited NO ($X^2\Pi_{1/2}$, v=1) (seeded in He) scattered from a cleaved (room temperature) LiF(100) surface it is observed that the survival probability for molecules in the vibrationally excited state is 0.9±0.1, i.e. as close to unity as could experimentally be determined [5].

The accuracy of the determination of the survival probability can be improved if also the vibrationally inelastic channel is probed. Normally this is impossible because only a small fraction of the molecules is prepared in the vibrationally excited state, and the remaining ground state molecules will dominate in such an experiment. If, however, both vibrationally and electronically excited molecules, or, alternatively, high(er) vibrationally excited molecules ($v\geq2$) are scattered, the vibrationally inelastic channel can be probed and vibrational deactivation probabilities can be determined very precisely.

In this chapter we report on state-to-state scattering experiments with vibrationally and electronically excited CO($a^3\Pi$, v=1) molecules from a LiF(100) surface. From recent scattering studies with metastable CO molecules in their vibrational ground state it is known that a few percent of these molecules survive the collision with a LiF(100) surface as a metastable molecule [16, 17]. In the experiments reported here both the vibrationally elastic channel (Δv=0) and for the first time also the vibrationally inelastic channel ($\Delta v = -1$) have been probed for the scattering process.

6.2 Experimental

The experimental set-up for the scattering experiments consists of a pulsed molecular beam machine that is connected to an Ultra High Vacuum (UHV) system as schematically indicated in Fig. 6.1. The operation principles of this machine have been discussed in detail elsewhere [17, 18]. To briefly summarize, a mixture of 20% CO in a rare gas is expanded into vacuum to produce a pulsed supersonic beam. Metastable CO molecules are prepared by direct laser excitation. The + parity component of the $a^3\Pi_1(v{=}1,J{=}1)$ level is populated

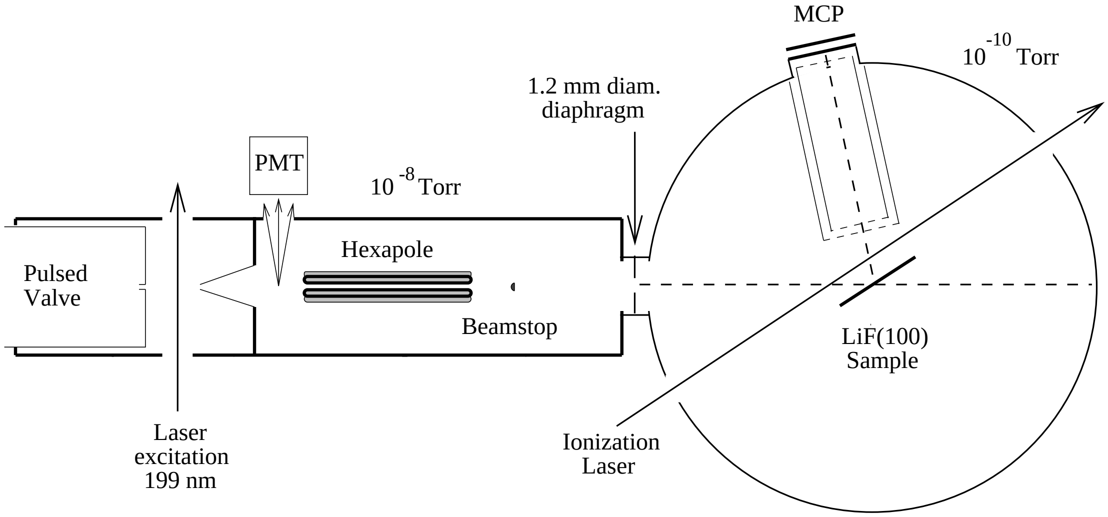

Figure 6.1: *Schematic view of the experimental setup. The 199 nm laser excitation in combination with the hexapole-beamstop-diaphragm setup allows preparation of a pure beam of vibrationally excited metastable CO molecules in the UHV chamber. The production of metastable CO molecules is monitored with the photomultiplier (PMT). Internal state distributions are probed via a (1+1)-REMPI scheme from the* a$^3\Pi$ *state using an ionization laser around 280 nm. Mass selective ion detection is performed using the ion extraction assembly mounted in front of the MCP detector.*

via excitation on the $Q_2(1)$ line of the spin-forbidden a$^3\Pi$ $\leftarrow$X$^1\Sigma^+$ transition using pulsed 199 nm radiation (~0.5 mJ in a 150 MHz bandwidth). Subsequently, the molecular beam enters the hexapole chamber via a 0.8 mm diameter skimmer. Only the laser-prepared metastable CO molecules are bent around the beamstop with the electrostatic hexapole and are focused onto the 1.2 mm diameter diaphragm; a almost pure beam of metastable CO molecules, essentially free of carrier gas atoms and ground state CO molecules, enters the UHV scattering chamber. The averaged kinetic energy of the metastable CO molecules is 78 meV.

A cleaved LiF(100) crystal is mounted on a manipulator in the UHV system, 72.5 cm downstream from the excitation region. The LiF surface is chosen for these experiments as it is known that part of the metastable CO(a$^3\Pi$, v=0) molecules retains their electronic energy (6.0 eV) after scattering from this surface [16, 17]. The vibrational energy of CO (0.22 eV) might be conserved as well in the interaction with the surface, as high survival probabilities have been reported for scattering of vibrationally excited NO molecules from this same surface [5].

After scattering, both the vibrationally elastic and inelastic channels are probed in a (1+1)-Resonance Enhanced Multi-Photon Ionization (REMPI) scheme. The extraction assembly used for mass-selective ion detection is depicted in Fig. 6.1. The b$^3\Sigma^+$(v=1)$\leftarrow$a$^3\Pi$ (v=1) transition around 279 nm is used as the resonant step in the REMPI process and probes the vibrationally and electronically elastic channel, while the corresponding 0$\leftarrow$0 band around 283 nm [19, 20] probes the vibrationally inelastic channel. Both the 279 nm and the 283 nm radiation are produced by frequency doubling the output of a pulsed dye laser system. Ions are produced in a volume close to the LiF surface and are extracted to impinge on a Micro-Channel Plate (MCP) detector. The angle of incidence is chosen to be θ_i=51°, to allow free passage of the ionization laser close to the LiF surface.

6.3 Results and discussion

Figure 6.2 shows experimental (1+1)-REMPI spectra of the incoming beam (upper trace) and the scattered beam (middle trace) of metastable CO molecules. The upper trace shows two features, both originating from the laser prepared $a^3\Pi_1(v{=}1,J{=}1)$ level. The middle trace shows the REMPI spectrum of the scattered metastable CO molecules that remain in the v=1 state. The rotational redistribution within the $a^3\Pi(v{=}1)$ state is evident. The experimental spectrum is fitted in a similar way as was accomplished previously for the spectra obtained for scattering CO molecules in the $a^3\Pi(v{=}0)$ state [17]. The frequencies for the $b^3\Sigma^+(v{=}1)\leftarrow a^3\Pi(v{=}1)$ transition are taken from literature [21, 22]. From a least-squares fit of the contour of the experimental spectrum, the rotational temperature, as well as the relative population within the three different Ω-components of the $a^3\Pi$ state is obtained. The best fitting spectrum is shown in the lower trace of Fig. 6.2. Optimum agreement with the experimental spectrum is obtained for a rotational temperature of T_{rot}=290±25 K. The weight of the total population in levels with Ω=0 and 2 character relative to the total population in levels with Ω=1 character [17] is found to be 0.7±0.2. Both the rotational temperature and the observed overpopulation of levels in the initially prepared Ω=1 component is consistent with the results obtained for scattering of CO($a^3\Pi$, v=0) [17]. The part of the b←a spectrum to the red of the dashed vertical line is omitted from the fit as it overlaps the $a'^3\Sigma^+(v{=}35)\leftarrow a^3\Pi(v{=}1)$ spectrum.

The vibrationally inelastic channel is investigated via probing of the scattered metastable molecules that end up in the v=0 state. For a correct interpretation of the results, it is essential to know which fraction of CO molecules in the $a^3\Pi$ state in the incoming beam has decayed to the v=0 state by emission of infrared (IR) photons. These vibrationally deexcited CO molecules are scattered from the LiF(100) surface as well and at least partly contribute to the observed signal in the CO($a^3\Pi$, v=0) channel.

The left part of Fig. 6.3 shows the (1+1)-REMPI spectrum of metastable CO molecules in the incoming beam that reside in the lowest vibrational level (v=0) of the $a^3\Pi$ state. A mixture of 20% CO in Ar is used. The spectrum is measured with the hexapole state selector on and the beamstop in place, thus selecting a pure beam of metastable CO molecules (the absolute intensity of this spectrum is more than two orders of magnitude lower than the intensity of the spectrum in the upper trace of Fig. 6.2). In zero electric field, only radiative (IR) transitions from the laser prepared J=1 + parity level of the $a^3\Pi_1(v{=}1)$ state to the – parity component of the J=0, 1, and 2 levels of the different spin-components of the $a^3\Pi(v{=}0)$ state are allowed. From the Hönl-London factors for the IR $v{=}1\rightarrow v{=}0$ transition [23] it is calculated that mainly the J=1 and J=2 levels of the Ω=1 component become populated. The peaks indicated by $*$ (+) are, at least partially, originating from the + parity Ω=1 spin-component of the J=1 (J=2) level. Transitions

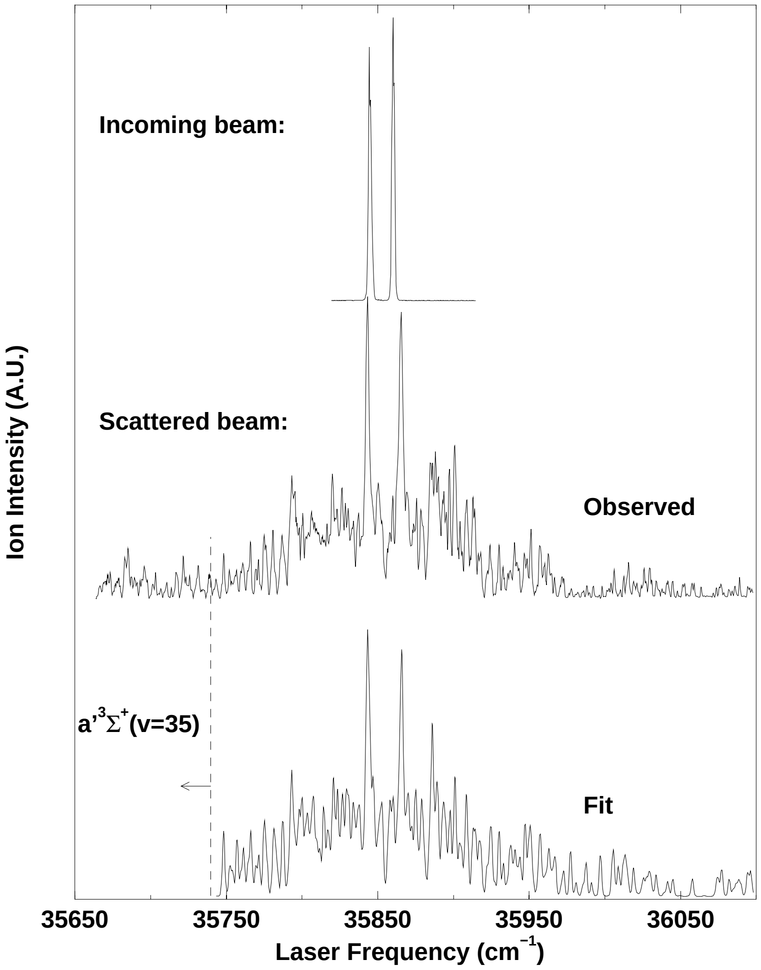

Figure 6.2: *Upper trace: REMPI spectrum showing the internal state distribution of the incoming beam of metastable CO molecules. The two features that are observed, originate from the laser prepared* J*=1 level in the* $a^3\Pi(v=1)$ *state that is focused by the hexapole. Middle trace: REMPI spectrum reflecting the population of rotational levels in the* $a^3\Pi(v=1)$ *state of the scattered CO molecules. The CO molecules that are probed have retained their electronic and vibrational energy. The spectrum is recorded for a gas mixture of 20% CO in Ar and* θ_i*=51°. Lower trace: Best fitting spectrum using* T_{rot}*=290 K, and an overpopulation of the* Ω*=1 component with a factor 1.4 relative to the other* Ω*-components.*

to the + parity components are possible in the electric field present inside the hexapole state-selector as the wavefunctions of + and – parity component become mixed. Part of the molecules decay to the + parity component of the $a^3\Pi_1(v=0, J=1)$ level (with positive Stark effect) and can thus be focused, while other molecules, decaying to levels with a small or negative Stark effect, are deflected much less efficiently or are even defocused by

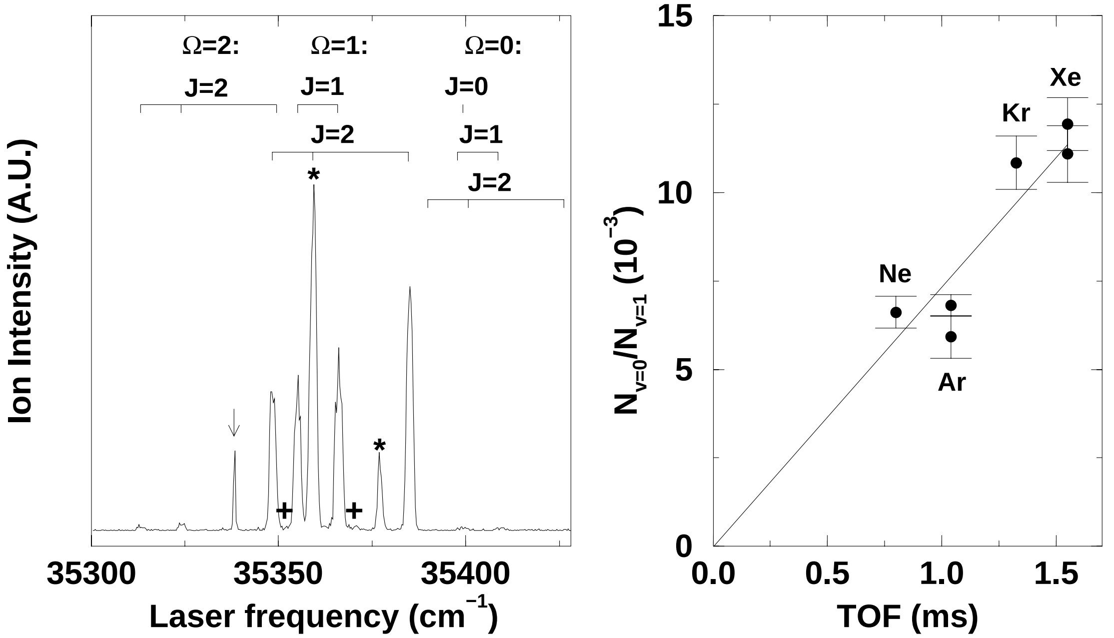

Figure 6.3: *Left: REMPI spectrum showing the relative population of the rotational levels in the* a$^3\Pi$*(*v*=0) state present in the incoming pure beam of metastable CO molecules (hexapole on, Ar seed gas). The (*J*,*Ω*) quantum numbers of the* $-$ *parity levels of the* a$^3\Pi$ *state probed in the b←a transition are indicated on top of the spectrum. The peaks indicated with* $*$ *and* $+$ *are originating from* $+$ *parity levels of* J*=1 and* J*=2 in the* Ω*=1 component. The narrow peak indicated with an arrow is probably due to the much weaker (non-saturated)* a$'^3\Sigma^+$*(*v*=34)←*a$^3\Pi$*(*v*=1) transition. Right: The experimentally determined ratio of the total population in the* v*=0 state (*$N_{v=0}$*) to the total population in the* v*=1 state (*$N_{v=1}$*) of CO (*a$^3\Pi$*) in the incoming beam versus the time after laser preparation in the* v*=1 state. The hexapole is switched of and the beamstop is removed.*

the hexapole. For this reason the peaks originating from the + parity component of the a$^3\Pi_1$(v=0, J=1) level are rather strong and the spectrum deviates from the one obtained for a field free situation.

From the REMPI spectrum in Fig. 6.3 the relative population in the different rotational levels of the a$^3\Pi$(v=0) state can be deduced. The ratio of the total population in the v=0 state ($N_{v=0}$) to the total population in the v=1 state ($N_{v=1}$) is obtained by comparing the corresponding REMPI spectra. The resonant step in the REMPI process is saturated and it is assumed that the ionization probability for the a$^3\Pi$(v=0) level (via the b$^3\Sigma^+$(v=0) level) is the same as that of the a$^3\Pi$(v=1) level (via the b$^3\Sigma^+$(v=1) level). After correction for the energy of the ionization laser and for the intensity of the metastable CO beam, the ratio $N_{v=0}/N_{v=1}$ is calculated to be $N_{v=0}/N_{v=1}=(4.2\pm1.0)\cdot10^{-3}$.

From the time evolution of this ratio, now measured for the unfocused molecular beam (hexapole switched off and beamstop removed), the radiative (IR) vibrational relaxation rate for CO in the a$^3\Pi$ state can be determined for the field free situation. The time evolution can be probed by using different carrier gasses, i.e. different velocities of the molecular beam. The right part of Fig. 6.3 shows the experimentally determined ratio (circles with error bars) as a function of time delay between preparation of the metastable CO molecules and ionization in the UHV chamber, 72 cm downstream from the excitation region.

From the rate equations for this system the ratio $N_{v=0}/N_{v=1}$ is calculated to be

$$N_{v=0}(t)/N_{v=1}(t) = \frac{\gamma_{10}}{\gamma_0 - \gamma_1 - \gamma_{10}} \left(1 - e^{-(\gamma_0 - \gamma_1 - \gamma_{10})t}\right) \tag{6.1}$$

in which γ_i is the radiative relaxation rate of metastable CO molecules in the vibrational level v=i to the electronic ground state, and γ_{10} is the radiative (IR) vibrational relaxation rate of metastable CO molecules in the v=1 state to the v=0 state. The electronic radiative relaxation rate of the a$^3\Pi$ state is expected to be large compared to the vibrational relaxation rate, and is calculated to be almost the same for the v=1 and the v=0 level ($\gamma_0 \approx \gamma_1 \approx 300$ s^{-1} [24]). For this reason the term in the exponent is small and $N_{v=0}(t)/N_{v=1}(t)$ can be approximated by $\gamma_{10}t$. The straight line in the right part of Fig. 6.3 is the best fit of this model through the experimental data points. The slope of this line corresponds to an IR vibrational relaxation rate of γ_{10}=7.4±1.1 s^{-1}.

The vibrationally inelastic channel of the scattered metastable CO molecules is probed by performing a scan for the scattered beam. It is observed that only a very small fraction of the scattered metastable molecules end up in the v=0 state. The spectrum is sampled by summing the ion signal over $6{\cdot}10^3$ laser pulses on top of and in between several band-heads. The ion intensity of scattered metastable CO molecules in the v=0 level is approximately 200 times weaker than the ion signal of scattered metastable CO molecules in the v=1 state. This signal can, assuming the same (electronical) survival probability for molecules in the v=1 and v=0 state, completely be attributed to the fraction of metastable CO molecules in the v=0 level in the incoming beam that is scattered from the LiF surface.

Thus we conclude that the vibrational relaxation channel upon collision with the LiF surface is at least two orders of magnitude slower than the electronic relaxation channel. From the strength of the ion signal of metastable CO molecules in the v=1 state it is concluded that the absolute (electronic) survival probability for metastable CO molecules in the v=1 level is in the same range (on the order of a few percent) as the survival probability for scattered metastable CO molecules in the v=0 level. This implies that the vibrational deactivation probability of CO(a$^3\Pi$, v=1) upon collision with the LiF surface is below 10^{-3}.

6.4 Conclusions

We have presented experiments in which vibrationally and electronically excited molecules are scattered from a LiF(100) surface. Both the vibrationally elastic and the vibrationally inelastic channel are probed for the scattered metastable CO molecules. The vibrational deactivation probability for this system is shown to be below 10^{-3}, indicating that the electronic relaxation channel is at least two orders of magnitude faster than the vibrational relaxation channel. The radiative (IR) vibrational relaxation rate γ_{10} for relaxation of

CO molecules prepared in the $a^3\Pi(v{=}1,\ J{=}1)$ level to the $v{=}0$ state is determined to be $7.4\pm1.1\ s^{-1}$.

In scattering experiments with CO ($a^3\Pi$) in its vibrational ground state it has been observed previously that translational and rotational temperature of the scattered beam depend on the kinetic energy of the incoming beam, thereby indicating a direct scattering mechanism, although the observed broad angular distribution [16, 17] points to a trapping-desorption process. The experiments reported here are in support of a direct scattering process; the small vibrational deactivation probability makes a significant contribution of a trapping-desorption channel highly unlikely.

Acknowledgements

This work has been realized in the framework of the EC-HCM network (ERB-CHR-XCT-94-0603).

References

[1] P.L. Houston and R.P. Merrill, Chem. Rev. **88**, 657 (1988).

[2] C.T. Rettner, D.J. Auerbach, J.C. Tully, and A.W. Kleyn, J. Phys. Chem. **100**, 13021 (1996).

[3] C.T. Rettner, F. Fabre, J. Kimman, and D.J. Auerbach, Phys. Rev. Lett. **55**, 1904 (1985).

[4] H. Zacharias, M.M.T. Loy, and P.A. Roland, Phys. Rev. Lett. **49**, 1790 (1982).

[5] J. Misewich, H. Zacharias, and M.M.T. Loy, Phys. Rev. Lett. **55**, 1919 (1985).

[6] J. Misewich, H. Zacharias, and M.M.T. Loy, J. Vac. Sci. Technol. B **3**, 1474 (1985).

[7] J. Misewich, P.A. Roland, and M.M.T. Loy, Surf. Sci. **171**, 483 (1986).

[8] J. Misewich and M.M.T. Loy, J. Chem. Phys. **84**, 1939 (1986).

[9] H. Vach, J. Häger, and H. Walther, Chem. Phys. Lett. **133**, 279 (1987).

[10] H. Vach, J. Häger, and H. Walther, J. Chem. Phys. **90**, 6701 (1989).

[11] A. Hodgson, J. Moryl, and H. Zhao, Chem. Phys. Lett. **182**, 152 (1991).

[12] C.T. Rettner, J.Chem. Phys. **99**, 5481 (1993).

[13] M. Gostein, H. Parhikhteh, and G.O. Sitz, Phys. Rev. Lett. **75**, 342 (1995).

[14] T.W. Francisco, N. Camillone, and R.E. Miller, Phys. Rev. Lett. **77**, 1402 (1996).

[15] M. Gostein and G.O. Sitz, J. Vac. Sci. Technol. A **14**, 1562 (1996).

[16] R.T. Jongma, G. Berden, D. v.d. Zande, Th. Rasing, H. Zacharias, and G. Meijer, Phys. Rev. Lett. **78**, 1375 (1997).

[17] Chapter 5 of this thesis and
R.T. Jongma, G. Berden, Th. Rasing, H. Zacharias, and G. Meijer, J. Chem. Phys. (in press).

[18] Chapter 2 of this thesis and
R.T. Jongma, Th. Rasing, and G. Meijer, J. Chem. Phys. **102**, 1925 (1995).

[19] G.H. Dieke and J.W. Mauchly, Phys. Rev. **43**, 12 (1933).

[20] T. Rytel, J. Mol. Spectrosc. **145**, 420 (1991).

[21] T. Rytel, J. Mol. Spectrosc. **173**, 370 (1995).

[22] R.W. Field, S.G. Tilford, R.A. Howard, and J.D. Simmons, J. Mol. Spectrosc. **44**, 347 (1972).

[23] I. Kovács, *'Rotational Structure in the Spectra of Diatomic Molecules'*, (Adam Hilger Ltd., London, 1969).

[24] T.C. James, J. Chem. Phys. **55**, 4118 (1971).

Samenvatting

Moleculaire bundel experimenten en verstrooiingsonderzoek met toestandsgeselecteerd metastabiel CO

In dit proefschrift staan experimenten beschreven waarin voor het eerst elektronisch aangeslagen moleculen aan een oppervlak zijn verstrooid. Om deze experimenten uit te kunnen voeren is er een moleculaire bundel-opstelling gebouwd waarmee een pure, toestandsgeselecteerde bundel van metastabiele CO-moleculen kan worden geprepareerd. Deze bundelopstelling is gekoppeld aan een ultra-hoog vacuum opstelling waarin de eigenlijke verstrooiingsexperimenten plaatsvinden. De werking van de gehele opstelling en de uitkomst van de verschillende experimenten die ermee zijn uitgevoerd staan in dit proefschrift beschreven.

De (interne) energie van een molecuul kan van invloed zijn op het proces dat een molecuul ondergaat wanneer het met een oppervlak botst. Het effect van translationele, rotationele en vibrationele energie op oppervlakte-verstrooiingsprocessen van moleculen is voor een aantal systemen al in meer of mindere mate onderzocht. Het effect van elektronische energie is tot nog toe echter niet bekeken, ondanks het feit dat deze energie meestal ordes van grootte meer is dan de kinetische en ro-vibrationele energie van het molecuul. De hier beschreven metingen zijn een eerste stap in de bestudering van oppervlakte-verstrooiing van elektronisch aangeslagen moleculen.

Voor relatief zware moleculen zijn er, voor niet reactieve systemen, slechts twee processen die kunnen optreden, namelijk directe (in)elastische verstrooiing en adsorptie, uiteindelijk gevolgd door desorptie. Door in detail de toestandsverdeling, hoekverdeling en snelheidsverdeling van de verstrooide moleculen te bestuderen, is het mogelijk onderscheid te maken tussen deze twee processen. Voor een direct verstrooiingsproces hangt normaal gesproken zowel toestands-, hoek- als snelheidsverdeling van de verstrooide moleculen af van de kinetische energie en hoek van inval van de inkomende bundel. Voor een adsorptie-desorptie proces is dit, bijna per definitie, niet het geval, waardoor in de meeste gevallen door meting van de genoemde verdelingen uitsluitsel kan worden verkregen over het proces dat het molecuul ondergaat.

Voor dit type verstrooiingsexperimenten wordt meestal gebruik gemaakt van supersone moleculaire bundels, met als voordeel dat na de expansie de kinetische en interne energie van de moleculen in de bundel goed is gedefinieerd. De karakterisatie van de bundelopstelling die is gebruikt voor het merendeel van de hier gerapporteerde experimenten staat beschreven in hoofdstuk 2. Met behulp van verfijnde tijd- en plaatsopgeloste detectiemethoden, die gebruik maken van de grote interne energie van de metastabiele moleculen, is het mogelijk om de moleculaire bundel in detail te karakteriseren. De interne energieverdeling, de snelheidsverdeling en de ruimtelijke verdeling van CO-moleculen in de bundel zijn bepaald. De 2D-detectietechniek laat verder bestudering toe van de banen die de metastabiele CO-moleculen in een hexapool doorlopen. De hexapool werkt voor moleculen zoals een lens voor licht werkt, en wordt gebruikt om de metastabiele CO-moleculen te focusseren. Daardoor ontstaat de mogelijkheid om een zuivere bundel van metastabiele CO-moleculen te maken met behulp van de combinatie van de hexapool, een bundelstop en een diafragma. Dit principe wordt uitgelegd en is experimenteel geverifiëerd.

In hoofdstuk 3 zijn de verschillende technieken beschreven die kunnen worden gebruikt om CO in de metastabiele $a^3\Pi$ toestand te detecteren. Detectie van Auger elektronen, geproduceerd door gebruik te maken van de 6.0 eV interne energie van het molecuul, detectie van de spin-verboden a→X fluorescentie en detectiemethoden gebaseerd op laser-ionisatie zijn beschreven. De efficiëntie van een MCP-detector voor detectie van metastabiel CO is bepaald. Tevens is de stralingslevensduur van CO-moleculen in de $a^3\Pi$ toestand bepaald via twee onafhankelijke methoden. Tenslotte blijkt ionisatie via de $b^3\Sigma^+$ toestand een gevoelige, toestandsopgeloste methode om metastabiele CO-moleculen te detecteren.

In hoofdstuk 4 is (als een afgeleid resultaat) een nieuwe methode beschreven om metastabiel CO met behulp van het lineaire Stark effect op te sluiten in een speciaal ontworpen elektrode-configuratie. De methode is gebaseerd op het plotseling aanschakelen van een kracht op het CO-molecuul door deze moleculen in een elektrisch veld van de grondtoestand naar de $a^3\Pi$ toestand te exciteren. Baanberekeningen voor een realistische elektrode-configuratie laten zien dat metastabiele CO moleculen gedurende hun gehele levensduur in deze 'val' kunnen worden opgeslagen in quasi-stabiele, planeetachtige banen. De spin-verboden fluorescentie van deze moleculen kan worden gebruikt om deze banen direct zichtbaar te maken.

Hoofdstuk 5 en 6 beschrijven de eerste oppervlakte-verstrooiingsexperimenten waarbij elektronisch aangeslagen moleculen zijn gebruikt. In hoofdstuk 5 zijn metingen beschreven waarin toestandsgeselecteerde CO-moleculen in de $a^3\Pi_1(v{=}0,J{=}1)$ toestand worden verstrooid van een LiF(100) oppervlak. Er is selectief gekeken naar de overlevende metastabiele CO-moleculen, dat wil zeggen naar het elektronisch-elastische kanaal. Met behulp van de bovengenoemde detectiemethoden zijn de overlevingskans en toestands-, snelheids- en hoekverdelingen van de verstrooide moleculen gemeten. Hoewel de hoekverdeling van de verstrooide moleculen breed is (hetgeen zou kunnen wijzen op een adsorptie-desorptie mechanisme), laten de metingen zien dat snelheids- en toestandsverdelingen van de verstrooide moleculen afhankelijk zijn van de kinetische energie van de inkomende moleculen. Dit betekent dat de overlevende metastabiele CO-moleculen een direct inelastisch verstrooiingsproces hebben ondergaan. In hoofdstuk 6 zijn verstrooiingsexperimenten met vibrationeel en elektronisch aangeslagen CO-moleculen van een LiF(100) oppervlak beschreven. De CO-moleculen zijn geprepareerd in de $a^3\Pi_1(v{=}1,J{=}1)$ toestand en zijn, na verstrooiing aan het oppervlak, toestandsopgelost gemeten. Het gebruik van deze moleculen maakt het mogelijk om, naast het vibrationeel- en elektronisch-elastische kanaal ($\Delta v{=}0$), ook het vibrationeel-inelastische kanaal ($\Delta v{=}{-}1$) van de verstrooide metastabiele CO-moleculen te bekijken. Uit de kleine fractie van vibrationeel gedeactiveerde moleculen in de verstrooide bundel kan worden geconcludeerd dat de elektronische deëxcitatiesnelheid minimaal twee ordes van grootte hoger is dan de vibrationele deactiveringssnelheid. De hoeveelheid verstrooide moleculen die zich in de a$^3\Pi(v{=}0)$ toestand bevindt, kan geheel worden verklaard door de hoeveelheid moleculen in de inkomende bundel die door emissie van een IR-foton is gerelaxeerd naar de vibrationele grondtoestand vóór de botsing met het oppervlak heeft plaatsgevonden. De relaxatiesnelheid van deze IR-overgang is nauwkeurig bepaald.

Curriculum Vitae

Op 8 juni 1970 ben ik geboren in Deventer. Na de lagere school in Nijmegen, heb ik een goede voorbereiding voor mijn universitaire studie genoten aan het Stedelijk Gymnasium in Nijmegen. Direct na mijn eindexamen, in 1988, ben ik begonnen aan de studie Natuurkunde aan de Katholieke Universiteit Nijmegen, waar ik na een jaar mijn propedeuse behaalde. Tijdens het derde en vierde jaar van mijn studie ben ik studentassistent geweest bij het practicum voor eerste- en tweede-jaars Natuurkunde studenten. In februari 1992 ben ik, onder begeleiding van Gerard Meijer, begonnen aan mijn afstudeerwerk op de afdeling Molecuul- en Laserfysica. In februari 1993 ben ik cum laude afgestudeerd. Uit mijn afdelingswerk vloeide uiteindelijk een promotieonderzoek voort, gebaseerd op een samenwerking binnen de RIM-onderzoeksschool tussen de afdeling Vaste Stof Fysica II en de afdeling Molecuul- en Laserfysica. Tijdens mijn promotietijd ben ik werkcollege-docent/coördinator geweest bij respectievelijk het college Structuur der Materie en het college Mechanica. Het wetenschappelijke resultaat van mijn promotie-onderzoek is in dit proefschrift weergegeven. Bijna aansluitend aan mijn promotie-onderzoek zal ik mijn wetenschappelijke werk voortzetten als post-doc aan de universiteit van Californië in Santa Barbara.

Publications

- *Coherent Cavity Ring Down Spectroscopy*
  G. Meijer, M.G.H. Boogaarts, R.T. Jongma, D.H. Parker, and A.M. Wodtke,
  Chem. Phys. Lett. **217**, 112-116 (1994).

- *Double Resonance Spectroscopy on Triplet States of CO*
  R.T. Jongma, M.G.H. Boogaarts, and G. Meijer,
  J. Mol. Spectrosc. **165**, 303-314 (1994).

- *Branch Intensities and Oscillator Strengths for the Herzberg Absorption Systems in Oxygen*
  D.L. Huestis, R.A. Copeland, K. Knutsen, T.G. Slanger, R.T. Jongma,
  M.G.H. Boogaarts, and G. Meijer,
  Can. J. Phys., **72**, 1109-1121 (1994).

- *Two-dimensional Imaging of Metastable CO Molecules*
  R.T. Jongma, Th. Rasing, and G. Meijer,
  J. Chem. Phys. **102**, 1925-1933 (1995).

- *Trace Gas Detection with Cavity Ring Down Spectroscopy*
  R.T. Jongma, M.G.H. Boogaarts, I. Holleman, and G. Meijer,
  Rev. Sci. Instr. **66**, 2821-2828 (1995).

- *High Rydberg States of DABCO: Spectroscopy, Ionization Potential, and Comparison with Mass Analyzed Threshold Ionization*
  M.G.H. Boogaarts, I. Holleman, R.T. Jongma, D.H. Parker, G. Meijer, and U. Even,
  J. Chem. Phys. **104**, 4357-4364 (1996).

- *State-to-state Scattering of Metastable CO Molecules from a LiF(100) Surface*
  R.T. Jongma, G. Berden, D. van der Zande, Th. Rasing, H. Zacharias, and G. Meijer,
  Phys. Rev. Lett. **78**, 1375-1378 (1997).

- *Confining CO molecules in Stable Orbits*
  R.T. Jongma, G. von Helden, G. Berden, and G. Meijer,
  Chem. Phys. Lett. (in press).

- *Scattering of Vibrationally and Electronically Excited CO Molecules from a LiF(100) Surface*
  R.T. Jongma, G. Berden, Th. Rasing, H. Zacharias, and G. Meijer,
  Chem. Phys. Lett. (in press).

- *State-to-state Scattering of Metastable CO Molecules from a LiF(100) Surface*
  R.T. Jongma, G. Berden, Th. Rasing, H. Zacharias, G. Meijer,
  J. Chem. Phys. (in press).

- *A Re-analysis of the* $k^3\Pi$ *State of CO*
  G. Berden, D. van der Zande, R.T. Jongma, and G. Meijer,
  in preparation.

- *State-specific Lifetime Determination of the* $a^3\Pi$ *State in CO*
  R.T. Jongma, G. Berden, and G. Meijer,
  in preparation.